MANCHESTER 1824
The University of Manchester

First Combined Measurement of the Electron-Neutrino and Electron-Antineutrino Individual Cross Sections on Argon using the MicroBooNE Detector

A thesis submitted to the University of Manchester
for the degree of Doctor of Philosophy
in the Faculty of Science and Engineering

2023

Marina Reggiani-Guzzo
School of Natural Sciences
Department of Physics and Astronomy

Contents

List of Figures **5**

List of Tables **16**

Abbreviations **19**

Abstract **21**

Declaration of Originality **22**

Copyright Statement **23**

Acknowledgements **24**

1 Introduction **26**

2 The Physics of Neutrinos **29**

2.1 History and Basic Neutrino Properties 31

2.1.1 The Discovery of the Neutrino 32

2.1.2 Neutrino Flavours 33

2.1.3 The Solar Neutrino Problem 36

2.2 Neutrino Oscillation 38

2.2.1 Neutrino Oscillation Parameters 40

2.3 Neutrino Sources 41

2.4 Accelerator Neutrino Experiments 42

2.5 Open Questions in Neutrino Physics 45

3 Neutrino Interactions **54**

3.1 Nuclear Effects 57

3.1.1 Final State Interactions 60

3.1.2 Topological classification 61

3.2 Helicity suppression . . . 61
3.3 Existing Electron Neutrino Cross-Section Measurements . . . 64
3.3.1 Summary . . . 70

4 The MicroBooNE LArTPC Detector 72
4.1 Liquid Argon Time Projection Chambers . . . 72
4.1.1 Liquid argon . . . 74
4.1.2 Scintillation Light . . . 74
4.1.3 Ionisation Charge . . . 76
4.1.4 Particle Signatures in MicroBooNE . . . 80
4.2 The MicroBooNE Detector . . . 81
4.3 Cosmic Ray Tagger . . . 84
4.4 Detector Performance Over the Run Period . . . 86
4.4.1 Light Response . . . 87
4.4.2 Unresponsive Wires . . . 89

5 The NuMI Beam at MicroBooNE 90
5.1 Neutrino Beam Production . . . 90
5.2 Neutrino and Antineutrino Modes . . . 92
5.3 Advantages of Using the NuMI Beam . . . 92
5.4 Readout and Trigger Systems . . . 96

6 Simulation and Reconstruction in MicroBooNE 99
6.1 Simulation Overview . . . 99
6.1.1 The NuMI Beam Simulation . . . 100
6.1.2 Neutrino Generation . . . 103
6.1.3 Cosmic Ray Modelling . . . 106
6.1.4 Propagation and Detector Simulation . . . 106
6.2 Signal Reconstruction . . . 107
6.2.1 TPC Charge Reconstruction . . . 107
6.2.2 PMT Light Reconstruction . . . 111
6.2.3 Reconstructed-Truth Matching . . . 112
6.3 Data and MC Samples . . . 113

7 Electron Neutrino and Antineutrino Selection 116
7.1 Boosted Decision Tree . . . 116
7.1.1 Boosting . . . 117

7.1.2 Evaluating the performance of BDT model . . . 123
7.2 Event Classifications . . . 124
7.3 Signal Selection . . . 125
7.3.1 Cosmic Ray Rejection . . . 125
7.3.2 Vertex Containment . . . 130
7.3.3 Shower Identification . . . 133
7.3.4 Electron Neutrino and Antineutrino Selection . . . 137
7.4 Selection Efficiency and Purity . . . 140

8 Electron Antineutrino BDT **143**
8.1 BDT Variables . . . 143
8.2 BDT Result . . . 145
8.3 Post Selection . . . 149

9 Measurement of the Electron-Antineutrino and Electron-Neutrino Cross Section **151**
9.1 Cross Section Calculation . . . 152
9.2 Cross Section Calculation using the Template Fit . . . 155
9.2.1 Template Fit . . . 156
9.2.2 Statistical uncertainty of the template fit . . . 157
9.2.3 Template Fit Result . . . 159

10 Uncertainty Calculation and Final Cross Section Result **161**
10.1 Systematic Uncertainties . . . 161
10.1.1 Summary . . . 165
10.2 Cross Section Result . . . 169

11 Conclusion **172**
11.1 Future Work . . . 173

A Other Projects **175**

References **176**

Word Count: 28 948

List of Figures

2.1 Standard model of particle physics. Figure from [2]. 30

2.2 Allowed interaction vertices in the SM: charged-current weak interaction with leptons (top left) and quarks (top centre), neutral-current weak interaction with leptons/quarks (top right), strong interaction (bottom left) and electromagnetic interaction (bottom right). 31

2.3 Energy spectrum of a β-decay. The continuous spectrum observed versus the expected fixed energy E_0. Figure from [4]. 33

2.4 Cross section measurements for the $e^+e^- \rightarrow$ hadrons decay. The lines represent the prediction from the SM for scenarios with 2, 3 and 4 active neutrinos. Figure from [11]. 36

2.5 Neutrino oscillation probability for different CP phases and mass ordering as function of the neutrino energy for a fixed distance of 1300 km. Figure from [21]. 43

2.6 Probability of $\bar{\nu}_e \rightarrow \bar{\nu}_e$, also known as "survival probability", versus $L_0/E_{\bar{\nu}_e}$ for the KamLAND data, where $L_0 = 180\,\text{km}$. The best-fit survival probability for a standard neutrino oscillation is shown as the blue curve. Figure from [27]. 44

2.7 Feynman diagram of a neutrinoless double beta decay. 47

2.8 The two possible scenarios for the order of the neutrino masses. The "normal hierarchy" (left) describes the scenario where $m_1^2 < m_2^2 < m_3^2$, and the "inverted hierarchy" (right) where $m_3^2 < m_1^2 < m_2^2$. The absolute neutrino mass is also unknown and it is indicated with the question mark at the bottom of the diagram. 49

2.9 Feynman diagrams of the neutrino interactions with matter. Ordinary matter has a much bigger concentration of electrons when compared to muons and taus. For this reason, the charged-current interaction between electron neutrino and electrons (right) is the largest contribution to the matter effect. The neutral-current interaction between neutrinos and electrons (left) happens at same rate regardless of the neutrino flavour and does not contribute to the matter effect. 50

2.10 Observed ν_e data by MiniBooNE neutrino mode as a function of the reconstructed neutrino energy under charged-current quasielastic (CCQE) scattering, E_ν^{QE}. The dashed histogram shows the best fit to the neutrino-mode data assuming the standard oscillation. . . . 52

2.11 Cherenkov signature for photons (left) and electrons (right). The top diagrams show the interactions from a side-view, and the bottom diagrams show the signature in a Cherenkov detector. Both cases create fuzzy rings and the photon-induced signal can be misidentified as an electron-induced signal if there is not enough and/or clear separation between the generated rings. Figure adapted from 53

3.1 Example of a Feynman diagram for $\nu_\ell + n \to \ell^- + p$. 55

3.2 Example of a Feynman diagram for $\nu_\ell + p \to \ell^- + p + \pi^+$, where the circle represents the resonance of the nucleon. 56

3.3 Total neutrino (top) and antineutrino (bottom) charged-current cross section per nucleon, divided by the neutrino energy as a function of energy [40]. The prediction for each interaction process is shown as dashed line for quasielastic scattering, dot-dashed line for resonance production and dotted line for deep inelastic scattering. The solid line represents the total prediction. 57

3.4 Scheme showing how a neutrino scattering on a free nucleon (left) is modified in the impulse approximation (right). This approximation considers the neutrino cross section as being the incoherent sum of elementary processes involving one nucleon. Figure adapted from . . 58

3.5 MiniBooNE ν_μCC cross section on ^{12}C in comparison to predictions with MEC (green solid), without MEC (red dashed) and Martini *et al.* prediction (dot-dash blue). Figure from [43]. 59

3.6 Sketch of possible interactions within the nucleus after an initial neutrino-nucleus interaction, and its final state particles. Figure from [44]. . . 60

3.7 Feynman diagram for the neutrino-electron (left) and antineutrino-electron (right) scatterings for a charged-current weak interaction. . . 61

3.8 Momentum (black arrow) and spin (white arrow) directions represented in the centre of mass of the scattering. In the relativistic approximation, all particles are LH helicity states, and all antiparticles are RH helicity states. 62

3.9 Plot of the function $f(\theta^*) = (1/2)^2 (1 + cos\theta^*)^2$ as a function of the angle θ^*. 63

3.10 Scheme of the antineutrino-electron backward scattering. 63

3.11 Flux integrated electron neutrino and antineutrino charged-current inclusive total 65

3.12 Flux-integrated differential ν_e CCQE-like cross section on hydrocarbon versus electron energy (left) and electron angle (right). Neutrino interactions are simulated using the GENIE 2.6.2 event generator. . . 66

3.13 Differential $\nu_e + \bar{\nu}_e$ cross section on argon as a function of the outgoing electron angle, measured by the ArgoNeuT experiment. Figure from [51]. 67

3.14 Differential cross section on argon as a function of the electron energy (left) and angle (right), measured by the MicroBooNE experiment. The angle β_e represents the electron's deflection from the neutrino direction. Figure from [53]. 68

3.15 Differential cross section on argon as a function of the electron energy (left) and angle (right) for interactions with one electron, N visible protons and no pions, defined as $1eNp0\pi$, measured by the MicroBooNE experiment. The angle θ_e represents the angle between the neutrino beam and electron direction. Figure from [54]. The "p-value" is the probability value 69

3.16 Differential cross section on argon as a function of the leading proton energy (left) and angle (right) for interactions with one electron, N visible protons and no pions, defined as $1eNp0\pi$, measured by the MicroBooNE experiment. The angle θ_p represents the angle between the neutrino beam and the leading proton direction. 69

3.17 Double differential cross section on carbon as a function of the electron angle and energy, measured by NOνA. Figure from [55]. 70

4.1 LArTPC working principle scheme. Figure adapted from [56]. The displayed coordinate system shows the "origin" of the system. The X and Z coordinates are often referred to as "drift direction" and "beam direction", respectively 73

4.2 Scintillation light processes in liquid argon: self-trapped exciton luminescence (top) and recombination luminescence (bottom). Both processes produce singlet and triplet excimers of Ar_2^* that decays producing the liquid argon scintillation light of 128 nm wavelength (Ref. [58]). 75

4.3 Liquid argon scintillation light recorded during tests done by the WArP collaboration. This waveform displays both, the fast decay component resulting from the singlet state decay, and the slow decay component resulting from the triplet state decay. Figure from [60]. . . 75

4.4 Diagram of an electromagnetic shower induced by an electron (left) and by a photon (right). Figure from [63]. 77

4.5 Effect of the longitudinal diffusion on the recorded waveform as a function of the drift time. A larger effect is observed on waveforms created closer to the cathode, that have longer drift times until their detection at the anode. Figure from [66]. 78

4.6 Entry/exit points of reconstructed cosmic muon tracks coincident with a signal from a muon counter located outside of the cryostat. In the absence of SCE and the associated non-uniform electric field in the detector volume, the points should be located strictly along the TPC boundaries (dashed lines). The anode is located at $x = 0\,\text{cm}$ while the cathode is at $x = 256\,\text{cm}$. Figure from [67]. 79

4.7 Examples of event displays collected by MicroBooNE showing the signal generated by tracks and showers. Figure adapted from [63]. The colour scheme shows the amount of energy deposited, high energy in red and low energy in blue. 80

4.8 The dE/dx for electron neutrino shower candidates split by particle type of the leading shower. The energy deposition is evaluated at the start of the shower. It is possible to see that electron-induced showers peak at $2\,\text{MeV/cm}$, whilst photon-induced showers peak at $\sim 4\,\text{MeV/cm}$. This distribution is limited to forward-going showers, whose angle with respect to the neutrino beam, θ, ranges from $0^o < \theta < 60^o$. Figure from [63] 81

4.9 Schematic diagram of the MicroBooNE LArTPC. The outer surface represents the cryostat, the the rectangular block inside represents the TPC, volume which defines the "active volume" of the detector. Figure from [56]. 82

4.10 Shape of the signals recorded on the U, V and Y planes in MicroBooNE. These signals show the bipolar behaviour of the induction planes, U and V, and the unipolar behaviour of the collection plane, Y. Figure from [68]. 84

4.11 Comparison between data and simulation using a variable number of wires adjacent to the wire closest to the ionisation electrons. Figure from [68] 85

4.12 A picture of the PMT structure used in the MicroBooNE detector. The acrylic plate is coated with TPB that allows the scintillation light to be detected by the PMT [56]. 85

4.13 (left) Scheme of the CRT system installed in the MicroBooNE detector. (right) Simulation of cosmic rays crossing the CRT, where the lines represent possible cosmic ray tracks. Figure from [69]. 86

4.14 Number of events seen by the CRT system. The increase from $\sim 2.5\,\mu$s to $\sim 4.1\,\mu$s is related to BNB-induced events, and the increase from $\sim 5\,\mu$s to $\sim 15\,\mu$s is related to NuMI-induced events, as indicated on the plot. Figure from [69]. 87

4.15 Percentage change in the observed light over time for the APT (black) and CPT (red) events. Figure from [70]. 88

5.1 Diagram illustrating the production of the BNB and NuMI beams production at Fermilab. Figure from [63]. 91

5.2 A diagram of the NuMI neutrino beamline. The change between the FHC and RHC polarities is achieved by inverting the polarity of the magnetic horns. Figure from [63]. 91

5.3 Feynman diagram of the decays in Table 5.1. (a) Feynman diagram for decays $\pi^{\pm} \to \mu^{\pm} + \nu_{\mu}(\bar{\nu}_{\mu})$, $\pi^{\pm} \to e^{\pm} + \nu_{e}(\bar{\nu}_{e})$ and $K^{\pm} \to \mu^{\pm} + \nu_{\mu}(\bar{\nu}_{\mu})$, where $\pi^{+} = u\bar{d}$, $\pi^{-} = \bar{u}d$, $K^{+} = u\bar{s}$ and $K^{-} = \bar{u}s$. (b) Feynman diagram for decays $K^{\pm} \to \pi^{0} + e^{\pm} + \nu_{e}(\bar{\nu}_{e})$, $K^{\pm} \to \pi^{0} + \mu^{\pm} + \nu_{\mu}(\bar{\nu}_{\mu})$, $K^{0}_{L} \to \pi^{\mp} + e^{\pm} + \nu_{e}(\bar{\nu}_{e})$ and $K^{0}_{L} \to \pi^{\mp} + \mu^{\pm} + \nu_{\mu}(\bar{\nu}_{\mu})$, where $K^{0}_{L} = (1/\sqrt{2})(d\bar{s} + s\bar{d})$. (c) Feynman diagram for decay $\mu^{\pm} \to +e^{\pm} + \nu_{e}(\bar{\nu}_{e}) + \nu_{\mu}(\bar{\nu}_{\mu})$. 93

5.4 NuMI neutrino flux as a function of the mother particle. The percentages consider a neutrino energy threshold of 60 MeV to remove the large contribution from the muon decay for low neutrino energies. Figure from [63]. 94

5.5 Cumulative POT delivered by the NuMI beam throughout MicroBooNE's working period, from Run 1 to Run 5. Figure adapted from [73]. 95

5.6 Relative position of the MicroBooNE detector with respect to the NuMI beam. Figure from [63]. 96

5.7 Scheme of the MicroBooNE readout and trigger systems. Figure from Ref. [63]. 97

6.1 The NuMI beam central value prediction for MicroBooNE in both FHC (left) and RHC (right) configurations. The integrated proportions of the flux are shown in the legend. Figure from [63]. 102

6.2 Simulated neutrino interactions predicted by GENIE v3.0.6 without (left) and with (right) the μB tune applied [97]. 105

6.3 The field response for each wire plane (left) and the electronics response for different peaking time configurations (right). Figure from [104]. 107

6.4 Representation of the filtering effects in the collected waveform (purple), after applying a noise filter (green), and deconvolution (orange). Figure from [108]. 108

6.5 Cells constructed with the MicroBooNE detector geometry. Cell boundaries are represented by coloured lines, while the wire centres are represented by gray lines. All cells have equilateral triangular shapes due to the $\pm 60^o$ wire orientation [105]. 109

6.6 Diagram of the hit cells in the MicroBooNE detector and a "blob" constructed by the hit wires. The solid lines represent the wires, and the blue dots represent the hit cells. The "blob" is formed by the contiguous hit cells and marker by solid blue lines. Figure from [109]. 110

6.7 Diagram of the inactive regions on the 2D anode plane for the 3-plane tiling approach (top) and for the 2-plane tiling approach (bottom). Figure from [109]. 111

6.8 (left) Scheme of a 2-plane tiling approach where all u_1, u_2, v_1, v_2, v_3 wires registered signals coming from the true hits, in red. The blue hits represent fake hits given the registered signals. (right) Matrix representation of the diagram on the left. Figures from [105]. 112

7.1 Scheme of a decision tree of depth equals 2. 117

7.2 Example of a tree showing the dataset split based on the variable "height". This tree displays the first residual per entry i, $r_{i,1}$, on each leaf based on the condition "height < 1.57", as well as the output value per leaf j, $O_{j,m}$, where m is the iteration number. Each leaf is labelled as $R_{m,j}$, where m is the iteration number and j is the leaf number. 119

7.3 Body weight prediction for a new entry of height 1.54 m using the simple model trained in this section. 120

7.4 Example of tree using two different thresholds based on "height". The tree on the left has a higher gain in comparison to the one on the right, which indicates that the tree on the left clusters the entries better. . . 122

7.5 Scheme of three possible regimes for the BDT model. The top line shows the distribution for signal (green) and background (red), and the bottom line shows the AUC curve for each regime. These are illustrative plots. The left column represents the "perfect classifier" regime, where the separation power is maximum between signal and background and AUC=1. The mid columns represents the "good classifier" regime, where there is some level of overlap between the signal and background distributions but it still has a good separation power, 0.5 <AUC< 1. And the right column represents the "random classifier", where there is no separation power and AUC=0.5. 124

7.6 Examples of a track caused by a STM (left) and by a TGM (right). Figure from [112]. 127

7.7 Example of a dE/dx distribution for a stopping muon. The rise in dQ/dx at the end of the track characterises the Bragg peak. Figure from [112]. 128

7.8 Neutrino energy distribution after applying the wirecell cosmic ray rejection. Most of the cosmic ray contribution is removed, without prioritising the selection of any neutrino flavour. 129

7.9 Neutrino energy distribution after imposing the vertex containment condition. This step does not affect the distribution significantly but it is crucial to guarantee that the analysis only uses events whose reconstruction we trust. 132

7.10 Examples of EM interactions. (a) low-energy wiggled track, (b) track with two isolated showers (shower-like objects are indicated by red colour and track-like objects are indicated by blue colour) , (c) an EM shower from a high-energy electron. The colours represent the reconstructed charge for each space point, where the blue, cyan, green, yellow, and red colours represent from less to more charge, respectively. Rainbow circles indicate particle starting positions. Figure from [113]. 134

7.11 Neutrino energy distribution after requesting the presence of a shower. This step mostly affects the muon-like events, because muons are responsible for creating a track-like signal in the detector rather than a shower-like one. 135

7.12 Neutrino energy distribution after applying the electron neutrino and antineutrino selection. 138

7.13 Selection efficiency for ν_eCC and $\bar{\nu}_e$CC as a function of the true neutrino energy. The efficiency uncertainty is calculated as $\sigma_\epsilon = \sqrt{(\epsilon/N) \times (1-\epsilon)}$ [115], where ϵ is the efficiency, and N is the number of true events in the fiducial volume. 140

7.14 Selection efficiency as a function of the event selection step. 141

7.15 Purity as a function of the event selection step. 142

8.1 Scheme of the $\cos(\theta)$ used as one of the parameters to develop the BDT model. 144

8.2 Distribution of the reconstructed particle multiplicity for ν_e and $\bar{\nu}_e$ interactions. 146

8.3 Distributions of the reconstructed neutrino energy and reconstructed energy for ν_e and $\bar{\nu}_e$ interactions. 147

8.4 Distribution of the angle between the neutrino beam and the produced shower for ν_e and $\bar{\nu}_e$ interactions. 147

8.5 Diagram of the feature importance (left) and the Receiver Operating Characteristic (ROC) curve (right) of the BDT model trained in this analysis. 148

8.6 BDT score distribution for signal ($\bar{\nu}_e$) and background (split between ν_e and everything else). The area normalised plot (right) shows the different shape of the distributions, whilst the stacked weighted distribution (left) shows the real number of events. 148

8.7 Neutrino energy distribution for the selected ν_e (left) and $\bar{\nu}_e$ (right) selected interactions. The selection efficiency plotted on top represents the efficiency in selecting events below a certain energy threshold. . . 149

8.8 Shower energy distribution for the selected ν_e (left) and $\bar{\nu}_e$ (right) selected interactions. The selection efficiency plotted on top represents the efficiency in selecting events below a certain energy threshold. This plot is zoomed-in to lowest energies. 150

9.1 Study of the statistical uncertainty with scaling the beam-on distribution by a weight from 1 to 6 whilst keeping the CV MC distribution. 157

9.2 Study of the statistical uncertainty with scaling both beam-on and MC distributions by a weight from 1 to 6. 158

9.3 Study of the statistical uncertainty with scaling the MC distribution by a weight from 1 to 6 whilst keeping the nominal beam-on distribution. 158

9.4 Variation of the percentage fitting error as a function of the scaling weight applied to the samples, for tests 1 and 2 (left) and 3 (right). . 159

9.5 Stacked selected MC distribution in comparison to the selected beam-on distribution before (left) and after (right) applying the scaling factors calculated by the template fit. 160

10.1 Distribution of the BDT score of the various "flux" universes compared to the CV for ν_e (left) and $\bar{\nu}_e$ (right). The colour scheme represents the number of universes per bin, and the black line shows the CV distribution. 165

10.2 Distribution of the BDT score of the various "cross section" universes compared to the CV for ν_e (left) and $\bar{\nu}_e$ (right). The colour scheme represents the number of universes per bin, and the black line shows the CV distribution. The reason why there is a disagreement between the central value and the universe distributions is under study 166

10.3 Distribution of the BDT score of the various "reinteractions" universes compared to the CV for ν_e (left) and $\bar{\nu}_e$ (right). The colour scheme represents the number of universes per bin, and the black line shows the CV distribution. 166

10.4 Distribution of the BDT score of the various "detector" universes compared to the CV for ν_e (left) and $\bar{\nu}_e$ (right). The colour scheme represents the number of universes per bin, and the black line shows the CV distribution. 167

10.5 Distribution of the BDT score of the various "beamline" universes compared to the CV for ν_e (left) and $\bar{\nu}_e$ (right). The colour scheme represents the number of universes per bin, and the black line shows the CV distribution. 167

10.6 Percentile systematic uncertainty per variation used in this analysis. This plot is in "scaling term" units. 169

10.7 Systematic uncertainty contribution per variation type. 169

10.8 Comparison between the GENIE v3.0.6 cross section with and without tune, and the corrected cross section calculated in this analysis. . . . 170

10.9 Neutrino energy distribution at the end of the selection chain after normalising the ν_e and $\bar{\nu}_e$ categories by their calculated scaling terms of 1.06 and 0.78 respectively. 171

List of Tables

2.1 Summary of the lepton number, electron number and muon number for the leptons known in the 1960s. 34

2.2 Summary of the neutrino oscillation parameters in a 3ν scenario for the normal ordering and inverted ordering [20]. 41

3.1 Summary of the existing electron neutrino cross-section measurements on argon. 71

4.1 Summary of technical information about the wire planes used in the MicroBooNE detector. 83

5.1 Relevant decay modes and their branching ratios for the production of the NuMI beam neutrinos (antineutrinos) [72]. 94

5.2 NuMI neutrino modes during MicroBooNE working period. 95

6.1 The corresponding number of POT for each sample used in this analysis. The beam-off sample is not recorded during beam time, therefore the equivalent-POT listed here for this sample is calculated as a ratio between the beam-on and beam-off HW triggers, multiplied by the recorded beam-on POT. The last columns display the number of simulated events in the MC sample without (third column) and with (fourth column) the data POT normalisation applied. 114

7.1 Example of dataset to explain the working principle of the Gradient Boosting technique. The first 3 columns show the input values of the dataset: height and body weight of 3 different individuals. Columns $F_m(x_i)$ represent the prediction value per iteration m. Columns $r_{i,m}$ represent the pseudo residual per iteration m, defined in Equation 7.2. Columns $O_{i,m}$ represent the output value per iteration m, defined in Equation 118

7.2 Number of interactions per topology for the full NuMI Run 1 data, before any selection cut is applied. 126

7.3 Number of interactions per topology after applying the cosmic ray rejection. Because the cosmic ray rejection is the first selection applied in this analysis, the "survival percentage since previous stage" is equal to the "absolute survival percentage". 130

7.4 The fiducial volume is defined as a volume 3 cm from the TPC boundaries of the MicroBooNE detector, and in this analysis this volume is limited by the coordinates described above. 131

7.5 Number of interactions per topology after applying the vertex containment condition. 131

7.6 Number of interactions per topology after applying the shower condition. 136

7.7 Number of interactions per topology after applying the electron neutrino and antineutrino selection. 139

9.1 Parameters related to the flux and beam-on POT used in this analysis. 155

10.1 List of categories of constraints composing the thin target assumption used by PPFX when predicting the neutrino flux, from Ref [63]. The first three lines represent the interactions proton-carbon of the protons coming from the accelerator unit at Fermilab. 162

10.2 List of the systematic variations used in this analysis, specifying if the method used was re-simulation (RS) or re-weighting (RW). The (*) variations are not available for antineutrinos. From Ref. [63]. 164

Abbreviations

The following list describes the meaning of the abbreviations used in this thesis. The abbreviations are listed in alphabetical order, and the page in which each one is defined is also given.

APT Anode-Piercing Track . . . 87

AUC Area Under (the ROC) Curve . . . 123

BDT Boosted Decision Tree . . . 27

BNB Booster Neutrino Beam . . . 67

CC Charged-Current . . . 54

CCQE Charged-Current Quasielastic . . . 55

CP Charge-Parity . . . 40

CPT Cathode-Piercing Track . . . 87

CRT Cosmic Ray Tagger . . . 84

COH Coherent . . . 104

CV Central Value . . . 100

DIS Deep Inelastic Scattering . . . 54

DUNE Deep Underground Neutrino Experiment . . . 42

EM Electro-Magnetic . . . 76

FHC Forward Horn Current . . . 90

FSI Final State Interactions . . . 60

GDML Geometry Description Markup Language . . . 175

HW Hardware . . . 97

IA Impulse Approximation . . . 58
ICARUS Imaging Cosmic And Rare Underground Signals . . . 42
IO Inverted Ordering . . . 40
KamLAND Kamioka Liquid Scintillator Antineutrino Detector . . . 42
KS Kolmogorov-Smirnov . . . 128
LAr Liquid Argon . . . 72
LArTPC Liquid Argon Time Projection Chamber . . . 27
LArSoft Liquid Argon Software . . . 106
LFG Local Fermi Gas . . . 105
LH Left-Handed . . . 31
LINAC Linear Accelerator . . . 90
LMM Light-MisMatched . . . 128
LSND Liquid Scintillator Neutrino Detector . . . 50
MC Monte Carlo . . . 100
MEC Meson-Exchange Current . . . 59
MicroBooNE Micro Booster Neutrino Experiment . . . 42
MINERνA Main Injector Neutrino ExpeRiment to study ν-A interactions . . . 100
MINOS Main Injector Neutrino Oscillation Search . . . 42
MSW Mikheyev-Smirnov-Wolfenstein . . . 49
NC Neutral-Current . . . 54
NO Normal Ordering . . . 40
NOνA NuMI Off-axis ν_e Appearance . . . 42
NuMI Neutrinos at the Main Injector . . . 27
PDF Parton Distribution Funtions . . . 104
PE Photo-Electrons . . . 97
PMNS Pontecorvo-Maki-Nakagawa-Sakata . . . 38
PMT Photomultipliers . . . 73
PPFX Package to Predict the FluX . . . 100
POT Protons on Target . . . 91

QE Quasi-Elastic . . . 54
RES Resonant . . . 54
RH Right-Handed . . . 31
RHC Reverse Horn Current . . . 90
ROC Receiver Operating Characteristic . . . 123
RPA Random Phase Approximation . . . 59
SBN Short-Baseline Neutrino . . . 42
SBND Short-Baseline Near Detector . . . 42
SCC Second Class Current . . . 165
SCE Space Charge Effect . . . 79
SM Standard Model . . . 26
SNO Sudbury Neutrino Observatory . . . 37
STM Stopping Muons . . . 127
SW Software . . . 97
TGM Through-Going Muons . . . 127
TPB TetraPhenyl Butadiene . . . 83
TPC Time Projection Chamber . . . 79
T2K Tokai to Kamioka . . . 42
VUV Vacuum Ultra-Violet . . . 75
WLS WaveLength Shifter . . . 83
XGBoost eXtreme Gradient Boosting . . . 116

Abstract

Neutrinos are one of the particles of Standard Model of Particle Physics that we know the least. It is believed that a better understanding of these particles could help answer open questions in particle physics, such as why we live in a matter-dominated universe. Because neutrinos are neutral particles, they are not directly detectable by all existing neutrino experiments. For this reason, any neutrino study relies on detecting the daughter particles from neutrino interactions inside the detectors. Therefore, a good understanding of how neutrinos interact, also known as their cross section, is crucial. The MicroBooNE experiment is a Liquid Argon Time Projection Chamber detector located at Fermilab that aims to study neutrinos and their properties. The work presented in this thesis describes the procedure to extract the first individual ν_e cross section on argon using the NuMI beam, and the first ever $\bar{\nu}_e$ cross section on argon. The analysis uses data collected during the NuMI Run 1, corresponding to 2.01×10^{21} protons on target. Using a template fit a normalised cross section on argon of $\sigma_{\nu_e} = [7.91 \pm 1.31\ (\text{stat}) \pm 1.77\ (\text{sys})] \times 10^{-39}\text{cm}^2/\text{nucleon}$ and $\sigma_{\bar{\nu}_e} = [2.40 \pm 1.39\ (\text{stat}) \pm 1.36\ (\text{sys})] \times 10^{-39}\text{cm}^2/\text{nucleon}$ for an average ν_e energy of 1195 MeV and $\bar{\nu}_e$ energy of 1550 MeV is measured.

Declaration of Originality

I hereby confirm that no portion of the work referred to in the thesis has been submitted in support of an application for another degree or qualification of this or any other university or other institute of learning.

Copyright statement

Acknowledgements

Firstly, I would like to thank Dr. Andrzej Szelc, for helping and supporting me since the beginning of my PhD. Your guidance and constant support deserve special recognition. Thank you Prof. Stefan Söldner-Rembold and Prof. Justin Evans for becoming my supervisor and co-supervisor in the middle of my PhD.

Thank you Krishan for helping me with my first steps in calculating a neutrino cross section, and for your patience in guiding me through your analysis. Thank you Elena and Afroditi for answering all my questions about the NuMI beam and cross sections. Thank you Jay, Wenqiang, Xin, Kaicheng and Giacomo for helping me understanding the Wire-Cell framework. Thank you Steven for your knowledge on systematic uncertainties. Thank you Aditya for always being available for my questions about Python. Thank you Nicola, Miquel and Holly for the weekly meetings and fruitful discussions about my analysis.

My PhD has developed in a troubled world where everyone was forced to learn how to live indoors for a long period of time, in which all kinds of communication had to be adapted. The challenges that this period has caused to my work and mental health are immeasurable. I would like to thank my family (Norma, Marcelo and Tomás) and my close friends Laryssa, Luisa, Vitor, Rafaela and Jully for always being there when I needed the most. The doctoral journey has also gifted me my partner, Giorgos, who has been supportive and kind.

Chapter 1

Introduction

The Standard Model (SM) of Particle Physics is the most accurate description of our universe to date. According to this model, all we know is composed of particles that interact between themselves via forces. Despite its success, there are many open questions in particle physics that the SM cannot answer, such as "why do we live in a matter-dominated universe?". Some of these answers could be found by studying neutrinos, particles that belong in the SM but ones we know surprisingly little about. For this reason, studying neutrinos is an exciting field of physics that has seen rapid development in the last few decades.

Neutrinos are intriguing particles that can change flavour as they travel. This phenomenon is known as neutrino oscillation. A precise understanding of neutrino oscillations is believed to be able to provide the necessary information to better understand some aspects of our universe. For this reason, a huge effort to develop and perfect neutrino oscillation experiments has been taking place in the last few years.

Regardless of the detection technology used, all detectors are blind to neutral particles until they interact. Because neutrinos are neutral, the only way to study them using current detectors is by identifying the daughter particles from neutrino interactions that happen inside the detector. Understanding how neutrinos interact, which is quantified by their cross section, is therefore vital.

This thesis describes the measurement of the electron-neutrino charged-current (ν_eCC) and electron-antineutrino charged-current ($\bar{\nu}_e$CC) individual cross section

on argon using the off-axis Neutrinos at the Main Injector (NuMI) beam at MicroBooNE. MicroBooNE is a Liquid Argon Time Projection Chamber (LArTPC) located at Fermilab dedicated to study neutrinos. This is the first ever measurement of the electron-antineutrino cross section on argon.

The structure of this thesis is as follows:

Chapter 2 starts by describing the history behind discovering the existence of neutrinos as well as the theoretical description of the neutrino oscillation phenomenon, and the current numerical values of the oscillation parameters.

Chapter 3 describes the types of interactions that neutrinos undergo in the detector. The chapter finishes by presenting the neutrino cross-section measurements performed to date.

Chapter 4 describes the MicroBooNE LArTPC detector and its operation. The description includes the types of signals generated by a neutrino interaction, as well as the detector effects and changes in the detector performance that affect them.

Chapter 5 describes the NuMI beam used in this analysis. This chapter explains how the neutrino beam is created at Fermilab, from the neutrino beamline structure to the particle decays that create neutrinos. A section is dedicated to outline the advantages of using the NuMI beam, as well as the readout and trigger systems.

Chapter 6 describes the simulation and reconstruction in MicroBooNE. This chapter explains how the produced signals from neutrino interactions are reconstructed, as well as how we simulate those interactions. The last part of the chapter summarises all the different samples created and used in this analysis.

Chapter 7 describes the method used in this analysis to select ν_e and $\bar{\nu}_e$ interactions. The selection chain is made of four steps, that are explained in this chapter. I have developed a machine learning tool, known as Boosted Decision Tree (BDT), to differentiate between ν_eCC and $\bar{\nu}_e$CC interactions, which is a novelty in this kind of analysis as most of the electron neutrino cross-section measurements go up to the point of calculating $\nu_e + \bar{\nu}_e$ combined cross sections.

Chapter 8 describes the procedure used in this analysis to calculate the electron neutrino and antineutrino cross sections. This chapter explains how the output of the BDT model is used in a template fit to data, and how the fitting parameters are

used to extract the cross section.

Chapter 9 describes the sources for the systematic uncertainties, with a brief description of each, their performance, and the mathematical procedure to calculate them. The final cross section result, with full statistical and systematic uncertainties is reported at the end of this chapter.

Chapter 10 summarises the content of this thesis, along with a list of possible improvements.

Chapter 2

The Physics of Neutrinos

All of the matter in the universe is made of elementary particles. An elementary particle is a particle that has no substructure, and can be thought of as a "building block" of matter. These particles are divided into two families: "quarks" and "leptons". Each family consists of six particles. The six quarks are: up (u), down (d), charm (c), strange (s), top (t), and bottom (b). The six leptons are: electron (e^-), muon (μ^-), tau (τ^-), electron neutrino (ν_e), muon neutrino (ν_μ), and tau neutrino (ν_τ). Every particle is associated with an antiparticle with the same mass and opposite quantum numbers, such as electric charge and magnetic moment. The antiparticles are commonly denoted by a bar over the symbol, for example: up antiquark ($\bar{u}$) or electron antineutrino ($\bar{\nu}_e$). Leptons, quarks and bosons are the so-called "elementary particles", which means that they are not composed of other particles. Leptons exist in 3 "flavours" (electron, muon and tau), whilst quarks exist in 3 "colours" (red, blue and green) and 6 "flavours" (up, charm, down, bottom, top and strange). The elementary particles can be split into two groups according to their spin: in the SM, "fermions" are the particles with spin equal to 1/2 (leptons and quarks), and "bosons" are the particles with an integer spin ($s = 1$ for Z, $W^{\pm}$, gluon and photon, and $s = 0$ for Higgs). "Hadrons" are subatomic particles that are built from quarks, they can be "mesons" (made of 1 quark and 1 antiquark, $q\bar{q}$, for instance pions, $\pi^+ = u\bar{d}$, and kaons, $K^+ = u\bar{s}$) or "barions" (made of 3 quarks, $3q$, or 3 antiquarks, $3\bar{q}$, for instance protons $= uud$, and neutrons $= ddu$).

These particles interact between themselves via the four fundamental forces: the strong, weak, electromagnetic, and gravitational forces. These forces are described

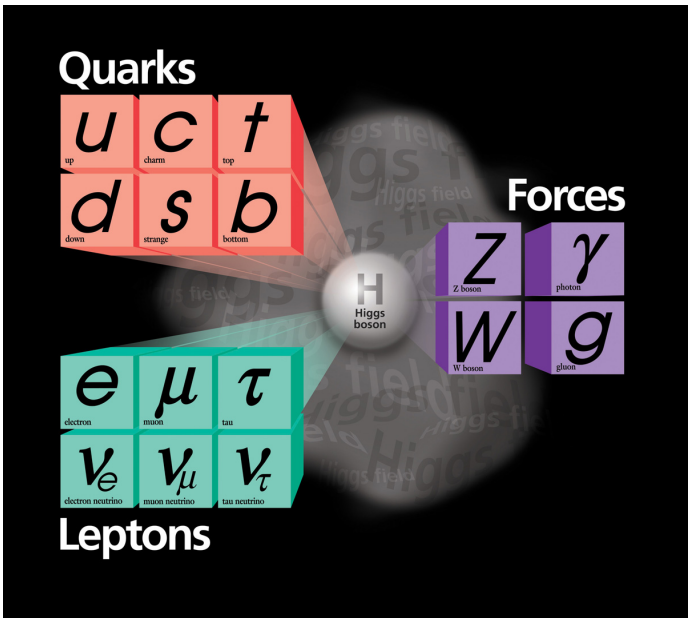

Figure 2.1: Standard model of particle physics. Figure from [2].

as the exchange of force-carrier particles with spin 1, also known as "bosons". We have identified these particles for all the forces apart from gravity. The strong force is carried by the "gluon" and it acts on quarks. The weak force is carried by the W and Z bosons and it acts on fermions, particles whose spin is an odd multiple of 1/2. The electromagnetic force is carried by the "photon" (γ) and only acts on electrically charged particles. The gravitational force acts on massive particles. The SM of Particle Physics [1] is a framework that mathematically describes the existing particles and three of the fundamental forces mentioned above, without including gravity. Figure 2.1 summarises the particles of the SM. The Higgs boson has spin 0 and interacts with massive particles.

The allowed interaction vertices in the SM are shown in Figure 2.2. The **weak interaction** can present itself via a charged-current (carried by the $W^{\pm}$ boson) or via a neutral-current (carried by the Z boson) interaction. A charged-current weak interaction vertex with lepton (Figure 2.2 top left) must conserve charge and lepton flavour. In a charged-current weak interaction vertex with quarks (Figure 2.2 top centre), on the other hand, charge and quark colour are conserved whilst quark flavour can change according to the Cabibbo-Kobayashi-Maskawa matrix [3]. A neutral-current weak interaction vertex (Figure 2.2 top right) conserve flavour, charge and colour, and has the same incoming and outgoing particle. The **strong interaction** (Figure 2.2 bottom left) is carried by a gluon and only couples with

quarks, which means leptons do not undergo strong interactions. Charge and quark flavour are conserved in a strong interaction, and quark colour can change, because gluons carry quark colour. The **electromagnetic interaction** (Figure 2.2 bottom right) is carried by a photon and couples with all charged particles.

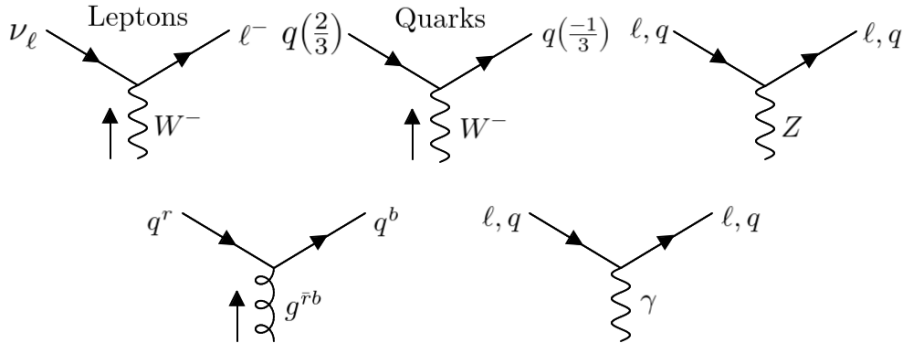

Figure 2.2: Allowed interaction vertices in the SM: charged-current weak interaction with leptons (top left) and quarks (top centre), neutral-current weak interaction with leptons/quarks (top right), strong interaction (bottom left) and electromagnetic interaction (bottom right).

This thesis focuses on a subset of the SM, namely neutrinos and antineutrinos and their interactions. This chapter will introduce the basic physics concepts involving these particles and the importance of studying them.

2.1 History and Basic Neutrino Properties

Neutrinos are one of the particles that make up the SM of particle physics. They are neutrally charged and extremely light particles that interact with matter primarily through the weak force[1]. Technically they also interact via the gravitational force because they have small mass but this is negligible. They can travel long distances without interacting, which makes it challenging to detect and study them. Mainly for this reason, we still do not know everything about these particles, such as their mass and if neutrinos and antineutrinos behave the same way. As they are still one of the most unknown particles in the standard model, resolving neutrinos can help answer

[1]The W bosons only couple with Left-Handed (LH) chiral particle states and Right-Handed (RH) chiral antiparticle states. Because neutrinos primarily interact via the weak force, it means that the only observed neutrinos are LH chiral particles and antineutrinos are RH chiral antiparticles.

some open questions in particle physics. Studying neutrinos and understanding their properties could also answer some mysteries involving our universe. Section 2.5 will explain three of these open questions.

2.1.1 The Discovery of the Neutrino

In the early 20th century the nuclear beta decay was presumed to be a neutron turning into a proton with the emission of an electron

$$ {}^{A}_{Z}X \rightarrow {}^{A}_{Z+1}Y + e^{-}, \tag{2.1} $$

where A is the mass number, Z is the atomic number, and X and Y are the nuclei before and after the beta decay, respectively. By applying the conservation of energy and momentum at the centre of mass of the original nucleus, it is straightforward to uniquely determine the energy of the outgoing electron in such a two-body decay as

$$ E_e = \frac{m_X^2 - m_Y^2 + m_e^2}{2m_X} c^2, \tag{2.2} $$

where m_X, m_Y, m_e and c are the mass of the nucleus X, the mass of the nucleus Y, the mass of the electron and the speed of light, respectively. Contrary to this, beta decay measurements observed that the energy of the outgoing electron was a continuous energy spectrum, as shown in Figure 2.3, instead of a fixed value as expected and described by Equation 2.2. This observation put into question one of the most important pillars of Physics: the conservation of energy. Would the beta decay be the first observation of a violation of this fundamental principle of physics?

In 1930, Wolfgang Pauli proposed that the beta decay was actually a three-body decay, with the emission of an electron and a, not-detected, neutral and very light spin 1/2 particle, which he originally called a neutron. This particle would carry the missing energy of the beta decay [5]. Enrico Fermi incorporated this new proposed particle into his theoretical model of beta decay and renamed it as *neutrino*, after Chadwick discovered the neutron [6], but experimental confirmation was still needed.

The first experimental evidence of the existence of the neutrinos was provided a few decades later, in 1956, by Frederick Reines and Clyde Cowan [7]. The experiment used for this confirmation consisted of placing two tanks with a total of 200 liters of

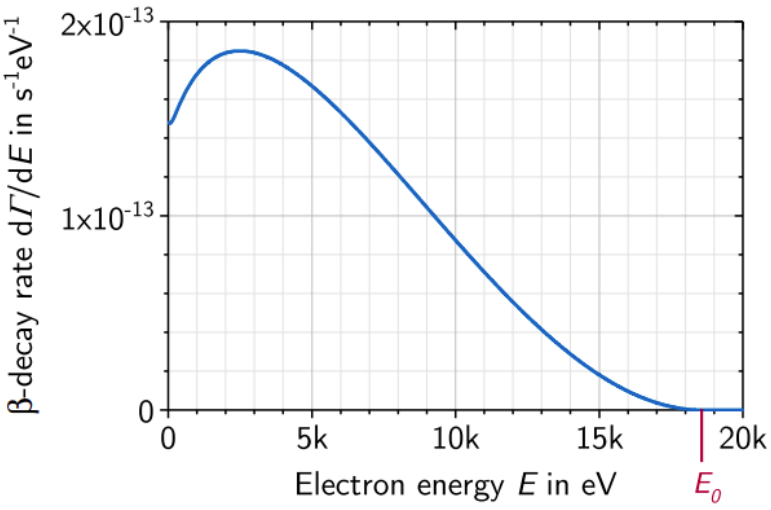

Figure 2.3: Energy spectrum of a β-decay. The continuous spectrum observed versus the expected fixed energy E_0. Figure from [4].

water with cadmium chloride next to the Savannah River nuclear reactor in South Carolina. If neutrinos existed, they would be produced at the reactor and induce an inverse β decay,

$$\bar{\nu} + p \rightarrow e^+ + n, \tag{2.3}$$

inside the detector. This reaction would promptly emit two photons due to the annihilation of the emitted positron (e^+) with electrons from the detector, followed by a few photons due to the neutron capture by the cadmium mixed with the water about $10\,\mu$s later. This signature was observed, confirming the existence of the neutrinos. This discovery earned Frederick Reines the Nobel Prize in 1995[2].

2.1.2 Neutrino Flavours

Confirming the existence of neutrinos was an important milestone. Not only did it confirm the validity of the principle of conservation of energy, but it also started a new field of studies in physics: experimental neutrino physics.

It was not understood at first why the process

$$\bar{\nu} + n \rightarrow p + e^-, \tag{2.4}$$

[2]The Nobel Prize was awarded to Frederick Reines alone because Clyde Cowan passed away earlier.

was not being observed as the reaction should conserve all the required quantities known at the time, including electrical charge. Only in 1953, Konopinski and Mahmoud [8] proposed the existence of a new quantity called the lepton number, L, that should be conserved. This quantity should assume the following values: $L = +1$ for leptons (ℓ^- and ν_ℓ, where $\ell = e, \mu, \tau$), $L = -1$ for antileptons (ℓ^+ and $\bar{\nu}_\ell$, where $\ell = e, \mu, \tau$) and $L = 0$ for non-lepton particles [8]. With this assumption it is straightforward to see that Equation 2.4 does not conserve lepton number since $L_{\text{initial}} = L_{\bar{\nu}} = -1$ differs from $L_{\text{final}} = L_{e^-} = 1$ and so, following this new model, the reaction in Equation 2.4 would be forbidden. The introduction of lepton number conservation however did not solve all the problems. The reactions

$$\mu^- \rightarrow e^- + 2\nu, \tag{2.5}$$

$$\mu^- \rightarrow e^- + \gamma, \tag{2.6}$$

where γ is an emitted photon, both conserve charge and lepton number, but only the reaction in Equation 2.5 was being observed. It was then proposed that there could be two kinds of neutrinos, one associated with electrons (the electron neutrino), and one associated with muons (the muon neutrino), and that there should be a new conserved number also associated to the different lepton flavours: the electron lepton number (L_e), and the muon lepton number (L_μ). A summary of these numbers is displayed in Table 2.1.

	L	L_e	L_μ
e^- and ν_e	1	1	0
μ^- and ν_μ	1	0	1
e^+ and $\bar{\nu}_e$	-1	-1	0
μ^+ and $\bar{\nu}_\mu$	-1	0	-1

Table 2.1: Summary of the lepton number, electron number and muon number for the leptons known in the 1960s.

In this new model, Equation 2.5 should be written as

$$\mu^- \rightarrow e^- + \nu_\mu + \bar{\nu}_e, \tag{2.7}$$

where the produced 2ν from Equation 2.5 are explicitly written as $\nu_\mu + \bar{\nu}_e$. Now it

is also possible to understand why the process described by Equation 2.6 was not being observed, since it does not conserve any of the lepton flavour numbers (L_e, L_μ).

Discovery of the Tau Neutrino

There is a third neutrino called "tau neutrino" that was discovered later. Similarly to the other two neutrinos, the tau neutrino interacts via the weak force producing a tau lepton. However, its detection had two main limitations. Firstly, tau leptons are heavy particles with a rest mass of 1.8 GeV (for a comparison, the mass of the other leptons is 0.510 MeV for electron and 106 MeV for muon). For this reason this interaction was not being observed by previous neutrino experiments since their neutrinos barely had enough energy to produce such a particle. Secondly, tau leptons are extremely hard to detect because they decay quickly, with a lifetime of $\sim 10^{-13}$ s.

This new particle is associated to a tau lepton number (L_τ) that follows the same rules L_e and L_μ, as described in the previous section: τ and ν_τ are associated to $L = L_\tau = 1$, and $\bar{\tau}$ and $\bar{\nu}_\tau$ are associated to $L = L_\tau = -1$.

The DONUT experiment was the first one to detect tau neutrinos. The experiment used a neutrino beam produced at Fermilab, produced by colliding 800 GeV protons on a tungsten target. This collision created, among other particles, the D_S mesons. The primary source of ν_τ was the D_S decays into τ and ν_τ. DONUT published in 2000 the first observation of ν_τ, that accounted for 4 ν_τ interactions [9].

Number of Light Neutrino Species

After the discovery of the Z boson in 1983 by the UA1 experiment on the SPS synchrotron [10], experiments on the next big accelerator, the Large Electron-Positron (LEP) Collider, started to study this new particle via observations of its decay. The LEP experiments such as ALEPH, DELPHI, L3, and OPAL were measuring the hadron production cross-section around the Z resonance given by

$$\sigma_{had} = \frac{12\pi}{m_Z^2} \frac{\Gamma_{ee}\Gamma_{had}}{\Gamma_Z^2}, \tag{2.8}$$

with

$$\Gamma_Z = N_\nu \Gamma_\nu + 3\Gamma_{ee} + \Gamma_{had}, \tag{2.9}$$

where Γ_Z is the total decay width, Γ_ν, Γ_{ee} and Γ_{had} are the partial widths of specific decay modes, and N_ν is the number of active light neutrinos. The result from those experiments led to the conclusion of the existence of 3 light active neutrinos coupling to the Z boson, as shown in Figure 2.4.

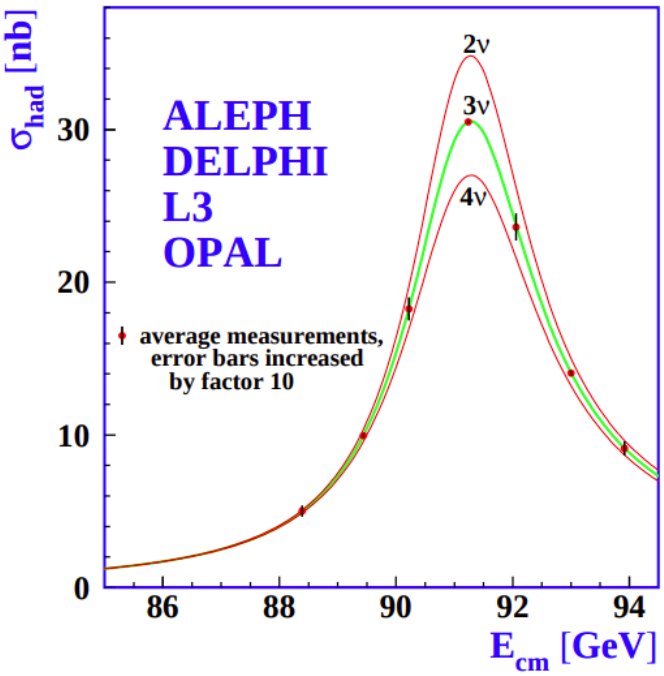

Figure 2.4: Cross section measurements for the $e^+e^- \rightarrow$ hadrons decay. The lines represent the prediction from the SM for scenarios with 2, 3 and 4 active neutrinos. Figure from [11].

2.1.3 The Solar Neutrino Problem

The Reines and Cowan experiment established that nuclear reactions produce (anti)-neutrinos. During the 50s the leading hypothesis assumed that nuclear reactions provided the power heating in the Sun. It did not take long for the neutrino theory to be implemented in the Standard Solar Model [12, 13], which describes the physics that happens inside the Sun, and for John Bahcall to calculate the expected Solar neutrino flux on Earth in 1960 [14]. The Homestake experiment [15] was built in 1968 by Raymond Davis to verify Bahcall's prediction. The experiment consisted of a large tank of a chlorine-rich liquid placed at 1.5 km underground in South Dakota,

and was trying to measure the following neutrino capture reaction

$$\nu_e + {}^{37}\mathrm{Cl} \rightarrow e^- + {}^{37}\mathrm{Ar}. \tag{2.10}$$

This reaction has two products: it creates a ^{37}Ar atom, and it also emits an electron [15]. The experiment could only detect ν_e and is only sensitive to the produced radioactive isotope ^{37}Ar. However, when analysing the full dataset collected during its 30-year operation, it was noted that the experiment measured an incoming neutrino flux 2/3 smaller than the one Bahcall predicted based on the solar nuclear reactions theory. This discrepancy became known as the Solar Neutrino Problem.

The discrepancy between Bahcall's Solar neutrino flux prediction and the one observed by the Homestake experiment could be explained by Bruno Pontecorvo's 1967 hypothesis that neutrinos could oscillate in flavour [16, 17]. This extraordinary theory means that an electron neutrino created at the core of the Sun can change its flavour to a muon neutrino, for example, on its way to Earth.

The neutrino oscillation explanation of the Solar Neutrino Problem was experimentally confirmed by the Sudbury Neutrino Observatory (SNO) [18]. The SNO experiment was a large heavy-water (D_2O) tank located in Canada. The advantage of this experiment is that deuteron can interact with neutrinos via three different reactions

$$\nu_e + d \rightarrow 2p + e^- \tag{2.11}$$

$$\nu_x + d \rightarrow n + p + \nu_x, \qquad x = e, \mu, \tau \tag{2.12}$$

$$\nu_x + e^- \rightarrow \nu_x + e^-, \tag{2.13}$$

where Equation 2.12 is sensitive to all neutrino flavours. For this reason the detector was able to measure the solar flux of all neutrino flavours and confirm that the total incident neutrino flux was in agreement with the predicted one in theory. Therefore the missing flux observed by Homestake could be explained by neutrinos changing flavour throughout their travel from the Sun to Earth.

2.2 Neutrino Oscillation

The current neutrino oscillation model considers three neutrino flavours: the electron neutrino (ν_e), the muon neutrino (ν_μ) and the tau neutrino (ν_τ). In this model, the flavour state of a neutrino with flavour α can be described as

$$|\nu_\alpha\rangle = \sum_{i=1}^{3} U^*_{\alpha i} |\nu_i\rangle \,, \tag{2.14}$$

where $|\nu_\alpha\rangle$ are the flavour states, $|\nu_i\rangle$ are the mass states and $U^*_{\alpha i}$ is an element of the so-called Pontecorvo-Maki-Nakagawa-Sakata (PMNS) matrix [19], described in Section 2.2.1. In order to understand how neutrinos oscillate as they travel, we need to follow the time evolution expression of the flavour state in Equation 2.14,

$$|\nu_\alpha(t)\rangle = e^{-iHt} |\nu_\alpha(t=0)\rangle = e^{-iHt} \left[\sum_{i=1}^{3} U^*_{\alpha i} |\nu_i\rangle \right], \tag{2.15}$$

where the mass state $|\nu_i\rangle$ is the eigenstate of the Hamiltonian in vacuum, which means that $H|\nu_i\rangle = E_i |\nu_i\rangle$ and therefore $e^{-iHt}|\nu_i\rangle = e^{-iE_i t}|\nu_i\rangle$, Equation 2.15 becomes

$$|\nu_\alpha(t)\rangle = e^{-iHt} \left[\sum_{i=1}^{3} U^*_{\alpha i} |\nu_i\rangle \right] = \sum_{i=1}^{3} e^{-iE_i t} U^*_{\alpha i} |\nu_i\rangle \,. \tag{2.16}$$

The probability of an initial state $|\nu_\alpha\rangle$ to oscillate to a final state $|\nu_\beta\rangle$ is given by $P(\nu_\alpha \to \nu_\beta) = |\langle \nu_\beta | \nu_\alpha(t)\rangle|^2$. The final state $\langle\nu_\beta|$ can be obtained by Hamiltonian conjugation of Equation 2.14 as

$$\langle \nu_\beta| = \sum_{j=1}^{3} U_{\beta j} \langle \nu_j| \,. \tag{2.17}$$

Then, putting together Equations 2.16 and 2.17, the oscillation probability becomes

$$P(\nu_\alpha \to \nu_\beta) = |\langle \nu_\beta | \nu_\alpha(t)\rangle|^2 \tag{2.18}$$

$$= \left| \left(\sum_{j=1}^{3} U_{\beta j} \langle \nu_j| \right) \left(\sum_{i=1}^{3} e^{-iE_i t} U^*_{\alpha i} |\nu_i\rangle \right) \right|^2 \tag{2.19}$$

$$= \left| \sum_{j=1}^{3} \sum_{i=1}^{3} e^{-iE_i t} U_{\beta j} U^*_{\alpha i} \langle \nu_j | \nu_i \rangle \right|^2 \tag{2.20}$$

$$= \left| \sum_{i=1}^{3} e^{-iE_i t} U_{\beta i} U^*_{\alpha i} \right|^2 \tag{2.21}$$

$$= \sum_{j=1}^{3} \sum_{i=1}^{3} U^*_{\beta j} U_{\alpha j} U_{\beta i} U^*_{\alpha i} e^{-i(E_i - E_j)t}. \tag{2.22}$$

Because neutrinos are very light particles travelling close to the speed of light, they are in the relativistic regime, and their energy can be written as

$$E_i = \lim_{m_i/p_i \to 0} \left(p_i^2 + m_i^2\right)^{1/2} \approx p_i + \frac{m_i^2}{2p_i} \approx E + \frac{m_i^2}{2E}, \tag{2.23}$$

using the Taylor approximation, where p_i and m_i are the momentum and the mass of the neutrino mass state i, respectively. Note that all neutrino mass states are produced coherently and therefore their momenta are the same, $p_i = p$, and since they are in the relativistic regime, the neutrino energy $E = E_i = p_i c = pL/t$, where L is the distance travelled in the time t.

In the neutrino oscillation phenomenon Equation 2.22 can be written as

$$\begin{aligned} P(\nu_\alpha \to \nu_\beta) = \delta_{\alpha\beta} - 4 \sum_{i<j}^{3} \mathfrak{Re}\left[U^*_{\beta j} U_{\alpha j} U_{\beta i} U^*_{\alpha i}\right] sin^2\left(\frac{\Delta m^2_{ij} L}{4E}\right) + \\ 2 \sum_{i<j}^{3} \mathfrak{Im}\left[U^*_{\beta j} U_{\alpha j} U_{\beta i} U^*_{\alpha i}\right] sin\left(\frac{2\Delta m^2_{ij} L}{4E}\right), \end{aligned} \tag{2.24}$$

where $\Delta m^2_{ij} \equiv m^2_i - m^2_j$, and L is the distance travelled by the neutrino. The probability for antineutrino oscillations, $P(\bar{\nu}_\ell \to \bar{\nu}_\beta)$, has the same format as Equation 2.24 with the imaginary term changing sign. Equation 2.24 shows that the neutrino oscillation probability depends on the ratio between the distance travelled by the neutrino and its energy, L/E. This quantity is important when it comes to comparing results from different experiments, since it is possible to reproduce results by tuning this parameter, either by changing the neutrino energy in a controlled neutrino source, or placing the detector at a specific distance from it.

2.2.1 Neutrino Oscillation Parameters

The neutrino oscillation phenomenon is described by three groups of parameters: neutrino masses, mixing angles and the Charge-Parity (CP)-phase. The neutrino masses can be experimentally determined by measuring the oscillation probability between neutrino flavours. However, as shown in Equation 2.24, oscillation measurements are only sensitive to measuring the mass splitting $\Delta m^2_{ij} \equiv m^2_i - m^2_j$ instead of the individual neutrino masses. The current experimentally measured values for those parameters are listed in Table 2.2 for Normal Ordering (NO) and Inverted Ordering (IO). The concept of NO and IO will be explained in Section 2.5.

The remaining parameters, mixing angles and CP-phase, are present in the oscillation equations as elements of the PMNS matrix. In a 3-flavour neutrino scenario, the PMNS matrix can be written as the product of 3×3 matrices as:

$$U = \underbrace{\begin{pmatrix} 1 & 0 & 0 \\ 0 & c_{23} & s_{23} \\ 0 & -s_{23} & c_{23} \end{pmatrix}}_{\text{Atmospheric}} \underbrace{\begin{pmatrix} c_{13} & 0 & s_{13}e^{-i\delta_{\text{CP}}} \\ 0 & 1 & 0 \\ -s_{13}e^{i\delta_{\text{CP}}} & 0 & c_{13} \end{pmatrix}}_{\text{Reactor}} \underbrace{\begin{pmatrix} c_{12} & s_{12} & 0 \\ -s_{12} & c_{12} & 0 \\ 0 & 0 & 1 \end{pmatrix}}_{\text{Solar}} \underbrace{\begin{pmatrix} e^{i\eta_1} & 0 & 0 \\ 0 & e^{i\eta_2} & 0 \\ 0 & 0 & 1 \end{pmatrix}}_{\text{Majorana}} \tag{2.25}$$

where $c_{ij} \equiv cos(\theta_{ij})$, $s_{ij} \equiv sin(\theta_{ij})$, θ_{ij} are the so-called mixing angles, and δ_{CP} is the CP complex phase [19], and η_1 and η_2 are the Majorana phases[3]. The mixing angles describe the mixing between mass and flavour neutrino eigenstates, and the CP phase describes if neutrino oscillation violates charge-parity.

As shown in Equation 2.14 the neutrino flavour states, α, are a quantum superposition of mass eigenstates, i, and the ratio of each contribution is determined by the mixing angles θ_{ij} from the PMNS matrix, Equation 2.25. It was experimentally measured that the mass eigenstates ν_1 and ν_2 are dominated by ν_e, and that ν_3 is dominated by ν_μ, as shown in Figure 2.8. For this reason, the term Δm^2_{12} is commonly known as $\Delta m^2_{\text{solar}}$ (because the majority of the solar neutrinos are ν_e), and the

[3]Because neutrinos are massive, chargeless and have spin 1/2, they are the only leptons that can either be a Dirac particle or a Majorana particle. Dirac particles are characterised as being different from their own antiparticles, whereas Majorana particles are the same as their own antiparticles. It is still unknown if neutrinos are Dirac or Majorana particles, and neutrino oscillation measurements cannot answer this question because the "Majorana matrix" becomes unitary in Equation 2.24 and does not contribute to the probability of oscillation.

term Δm^2_{23} is commonly known as Δm^2_{atm} (because the reactions involving cosmic rays in the atmosphere produce ν_μ).

Table 2.2 displays the best-fit-parameter in a 1σ range for all the parameters mentioned in this section.

Parameter	Normal Ordering	Inverted Ordering
$\sin^2\theta_{12}$	$\left(3.2^{+0.20}_{-0.16}\right) \times 10^{-1}$	$\left(3.2^{+0.20}_{-0.16}\right) \times 10^{-1}$
$\sin^2\theta_{23}$	$\left(5.47^{+0.20}_{-0.30}\right) \times 10^{-1}$	$\left(5.51^{+0.18}_{-0.30}\right) \times 10^{-1}$
$\sin^2\theta_{13}$	$\left(2.16^{+0.083}_{-0.069}\right) \times 10^{-2}$	$\left(2.22^{+0.074}_{-0.076}\right) \times 10^{-2}$
Δm^2_{21}	$\left(7.55^{+0.20}_{-0.16}\right) \times 10^{-5}$ eV^2	$\left(7.55^{+0.20}_{-0.16}\right) \times 10^{-5}$ eV^2
Δm^2_{32}	$\left(2.424^{+0.03}_{-0.03}\right) \times 10^{-3}$ eV^2	$\left(2.50^{+0.04}_{-0.03}\right) \times 10^{-3}$ eV^2
δ_{CP}	$\left(218^{+38}_{-27}\right)^o$	$\left(281^{+23}_{-27}\right)^o$

Table 2.2: Summary of the neutrino oscillation parameters in a 3ν scenario for the normal ordering and inverted ordering [20].

2.3 Neutrino Sources

There are many neutrino sources in the universe, this section will give a quick overview of some the possible neutrino sources and their energy range:

- **Sun**: solar neutrinos are produced via nuclear reactions and decays in the Sun. The main reaction is $p + p \rightarrow {}^2H + e^+ + \nu_e$ and produces a neutrino energy smaller than 1 MeV. Solar neutrinos are produced as ν_e.
- **Accelerators**: particle accelerators first accelerate protons until a desired energy, and then collide them to a fixed target usually made of carbon. This collision creates secondary particles that decay into neutrinos. The neutrino energy vastly depends on the initial proton energy, but accelerators usually produce neutrinos with a few GeV of energy. Accelerators primarily produce ν_μ.
- **Atmosphere**: cosmic rays coming from the universe create secondary particles when they interact with our atmosphere. Those secondary particles undergo decays and/or interactions with the atmosphere on their way to Earth, this

effect creates the so-called "cascade of particles", producing neutrinos. The energies of atmospheric neutrinos vary from hundreds of MeV to a few TeV. Atmospheric neutrinos are primarily ν_μ and ν_e and have a ratio of 2 : 1 of ν_μ/ν_e.

- **Nuclear reactors**: reactor neutrinos are generated via beta decays, as explained earlier in this chapter. They are mostly $\bar{\nu}_e$ with energy up to $\sim 10\,\text{MeV}$.
- **Supernovae**: the end of the life of massive stars is characterised by a powerful explosion called supernova which creates neutrinos of all flavours. Supernovae produces primarily ν_e and the typical neutrino energy varies from 10-20 MeV.

2.4 Accelerator Neutrino Experiments

In this thesis the emphasis is on accelerator neutrinos, and this section explains about accelerator neutrino experiments. Neutrino beams from accelerators are produced by colliding high-energy protons onto a target. This collision produces π and K that decay into neutrinos, resulting in a dominant muon neutrino (or antineutrino) beam, such as $\pi^\pm \to \mu^\pm + \nu_\mu(\bar{\nu}_\mu)$ and $K^\pm \to \mu^\pm + \nu_\mu(\bar{\nu}_\mu)$ as explained in Section 5.1. The produced neutrino beam has a broad energy spectrum typically around the GeV range. Accelerator neutrino experiments are often characterised by two detectors placed along a human-made neutrino beam. The distance between the detectors and the neutrino energy is chosen in a way in which L/E maximises the oscillation effects of interest. The first detector, the closest one to the neutrino source, is known as "near detector". The near detector provides information such as the initial neutrino flux and energy spectrum. The second detector, also known as "far detector", is placed at a distance L from the near detector such that the ratio L/E maximises the probability of observing oscillation. Figure 2.5 shows the neutrino oscillation probabilities for different CP phases and mass ordering for the Deep Underground Neutrino Experiment (DUNE) [21]. There are two kinds of experiments, a short-baseline, for L around a few hundred of meters (such as Short-Baseline Neutrino (SBN) programme [22] made of Short-Baseline Near Detector (SBND), Micro Booster Neutrino Experiment (MicroBooNE) and Imaging Cosmic And Rare Underground Signals (ICARUS) detectors), and a long-baseline for L of many kilometres (such as Kamioka Liquid Scintillator Antineutrino Detector (KamLAND) [23], Main Injector Neutrino Oscillation Search (MINOS) [24], Tokai to Kamioka (T2K) [25], NuMI Off-axis ν_e Appearance (NOνA) [26] and DUNE).

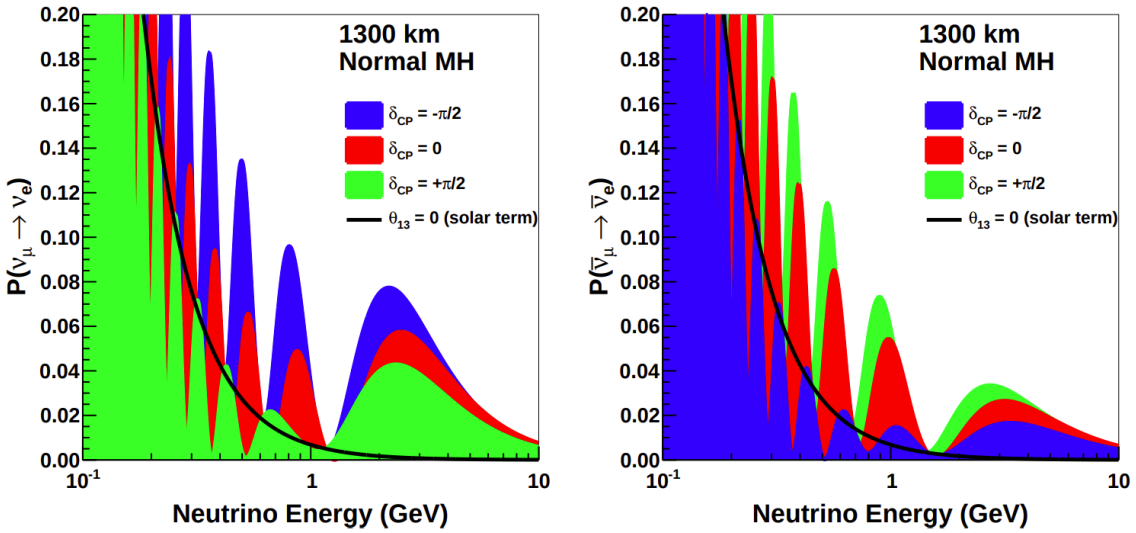

Figure 2.5: Neutrino oscillation probability for different CP phases and mass ordering as function of the neutrino energy for a fixed distance of 1300 km. Figure from [21].

In addition to choosing the distance between the near and far detectors, it is also important and possible to select the relevant neutrino energy. Neutrinos generated from π decays have an energy spectrum as a function of the neutrino direction, ϕ. For small ϕ, the neutrino energy spectrum is

$$E_\nu = \frac{[1 - (m_\mu/m_\pi)^2]E_\pi}{1 + (E_\pi/m_\pi)^2\phi^2}, \tag{2.26}$$

where E_ν and E_π are the energy of neutrino and π respectively. Therefore, on-axis experiments (where $\phi = 0$) are characterised by a broad band beam where the energy of neutrino is linearly proportional to the energy of pions. Off-axis experiments (where $\phi \neq 0$) are characterised by a narrow energy spectrum determined by ϕ. This method is used by off-axis neutrino experiments such as T2K and NOνA. From Equation 2.24 it is possible to see that the parameter $sin^2\theta_{ij}$ is related to the amplitude of oscillation, whilst the parameter Δm^2_{ij} is related to the frequency of oscillation. Therefore, it is possible to extract those parameters by measuring the oscillation probability, as shown in Figure 2.6.

The numerical value of the oscillation parameters were obtained by a combination of measurements and experiments. Solar experiments, such as SNO and SK, have provided the most precise measurement of θ_{12} via electron neutrino survival

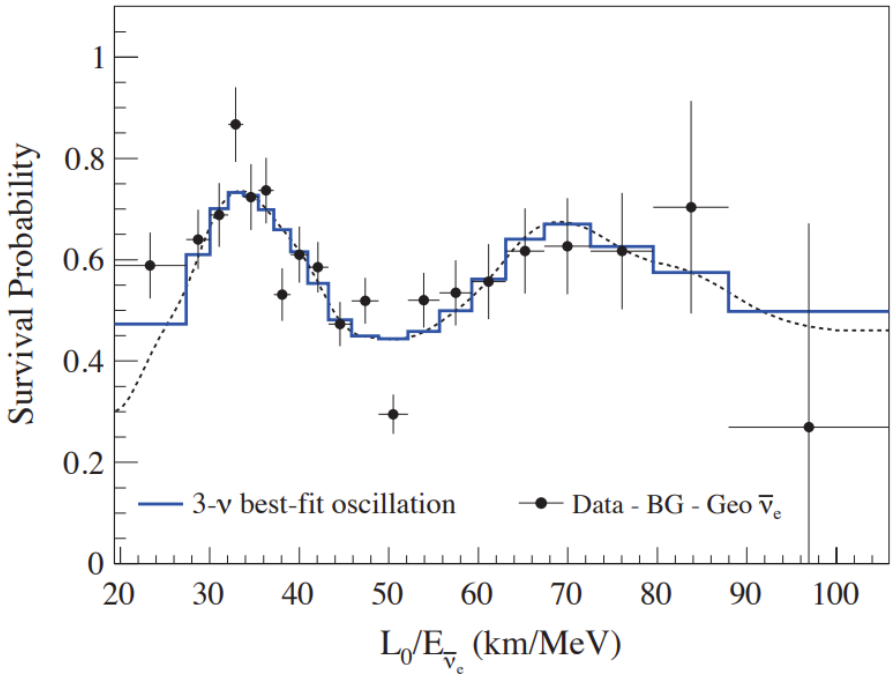

Figure 2.6: Probability of $\bar{\nu}_e \to \bar{\nu}_e$, also known as "survival probability", versus $L_0/E_{\bar{\nu}_e}$ for the KamLAND data, where $L_0 = 180\,\text{km}$. The best-fit survival probability for a standard neutrino oscillation is shown as the blue curve. Figure from [27].

measurements, $P_{\nu_e \to \nu_e} \simeq \sin^2(\theta_{12})$. The long-baseline reactor KamLAND have contributed to the measurement of Δm^2_{21} via the strong effect of the oscillation phase in the distortion of the reactor energy spectrum. The $\bar{\nu}_e$ survival probability for KamLAND is given by:

$$P_{\bar{\nu}_e \to \bar{\nu}_e} = 1 - \sin^2(2\theta_{12}) \sin^2 \frac{\Delta m^2_{21} L}{4E_\nu}. \tag{2.27}$$

Reactor medium baseline experiments such as Daya-Bay, Reno and Double-Chooz have provided the most precise determination of θ_{13} via ν_e survival probability measurements:

$$P_{\nu_e \to \nu_e} = 1 - \sin^2(2\theta_{13}) \sin^2 \frac{\Delta m^2_{ee} L}{4E_\nu}, \tag{2.28}$$

where $\Delta m^2_{ee} = \cos 2\theta_{12} \Delta m^2_{31} + \sin^2 \theta_{12} \Delta m^2_{32}$. Comparisons between ν_μ disappearance measurements at long-baseline experiments with ν_e disappearance measurements at medium-baseline experiments have provided information about Δm^2_{ee}, proportional

to Δm^2_{31} and Δm^2_{32}.

At present, ν_μ disappearance measurements at long-baseline experiments (such as MINOS, T2K, and NOνA) have provided the best determination of $|\Delta m^2_{31}|$, $|\Delta m^2_{32}|$ and θ_{23}. Whilst ν_e, $\bar{\nu}_e$ appearance measurements at long-baseline experiments (such as MINOS, T2K, and NOνA) have provided hints of δ_{CP}. More information on experimental measurements of the neutrino oscillation parameters can be found in [28].

2.5 Open Questions in Neutrino Physics

Charge-parity in the lepton sector

Charge and parity conjugations are mathematical transformations performed on the particle reaction. Charge conjugation is an operation of replacing particles by their antiparticles, whilst parity conjugation is an operation of reversing all the vector quantum quantities of the particles in a reaction. CP conjugation is the product of those two transformations.

The δ_{CP} phase measures if there is CP symmetry, and in the case of a neutrino measurement, it is commonly referred to as "charge-parity in the lepton sector". Measuring δ_{CP} could help explain the matter-antimatter asymmetry in the universe. The Big Bang theory predicts the production of equal amounts of matter and antimatter if CP symmetry is conserved. However current observations of a universe dominated by matter contradict this theory. The reason why the current universe is matter-dominated is still unknown. In 1967, Andrei Sakharov proposed that three necessary conditions should be met to explain the matter and antimatter asymmetry: (1) baryon number violation[4], (2) thermal inequilibrium, and (3) CP violation. Neutrino physics might provide a means to satisfy the third condition. One of the theories trying to answer this question is called "leptogenesis" [29]. This theory predicts that there was a process at the beginning of the universe, responsible for

[4]Baryons are particles made of 3 quarks, for instance protons (uud) and neutrons (ddu). According to the SM, the baryon number (equals +1 for baryons and −1 for antibaryons) is conserved in a reaction. Because proton is the lightest baryon, the baryon number conservation implies that protons are stable. Therefore, if a proton decay is observed it would be the first experimental evidence of baryon number violation. No proton decay has been observed to date though.

breaking the CP symmetry in the lepton sector. Confirming this theory relies on measuring the δ_{CP} phase. The leptogenesis theory is viable if $\delta_{\text{CP}} \neq 0, \pi$, otherwise if $\delta_{\text{CP}} = 0, \pi$ the leptogenesis would be ruled-out and the question of matter-antimatter asymmetry in the universe would remain unsolved.

The CP-phase can be measured by comparing the oscillation probability of neutrinos and antineutrinos individually, $P(\nu_\mu \rightarrow \nu_e)$ and $P(\bar{\nu}_\mu \rightarrow \bar{\nu}_e)$[5], respectively, where the oscillation probability is given by Equation 2.24. The difference between those probabilities can be written as

$$\begin{aligned}
\Delta P &\equiv P(\nu_\mu \rightarrow \nu_e) - P(\bar{\nu}_\mu \rightarrow \bar{\nu}_e) && (2.29)\\
&= -16\mathfrak{Jm}\left(U^*_{\beta j} U_{\alpha j} U_{\beta i} U^*_{\alpha i}\right) sin\Delta_{12} sin\Delta_{23} sin\Delta_{31} && (2.30)\\
&= -16 s_{12} c_{12} s_{23} c_{23} s_{13} c^2_{13} sin(\delta_{CP}) sin\Delta_{12} sin\Delta_{23} sin\Delta_{31} && (2.31)\\
&\sim sin(\delta_{CP}), && (2.32)
\end{aligned}$$

where $\Delta_{ij} \equiv \Delta m^2_{ij} L/4E$. Therefore measuring the difference between neutrino and antineutrino oscillation probability is directly related to measuring δ_{CP}. If $P(\nu_\mu \rightarrow \nu_e) \neq P(\bar{\nu}_\mu \rightarrow \bar{\nu}_e)$, then $\delta_{\text{CP}} \neq 0, \pi$ and it would configure CP violation in the lepton sector. Otherwise, if $P(\nu_\mu \rightarrow \nu_e) = P(\bar{\nu}_\mu \rightarrow \bar{\nu}_e)$, then $\delta_{\text{CP}} = 0, \pi$ it would configure CP conservation in the lepton sector.

The measured value for δ_{CP} displayed in Table 2.2 [20] however has a large spread. The 3σ range covers $157^o \rightarrow 347^o$ for NO and $202^o \rightarrow 349^o$ for IO. The range for NO comprises 180^o, which is one of the critical angles to establish if there is CP violation in the lepton sector or not, which leads to the conclusion that more measurements are needed.

[5]Neutrino flavours are identified in the detector when they undergo a charged-current interaction with the medium, because we can identify the produced charged lepton. In other words, when an electron/muon/tau neutrino undergo a charged-current interaction, it will produce an electron/muon/tau respectively. However, most of the neutrino oscillation experiments operate in an energy range not high enough to produce tau leptons. For this reason, even though tau neutrinos appear during the oscillation phenomenon, they do not have enough energy to undergo a charged-current interaction in the detector and produce a tau, so they end up not being identified. For this reason, it is common for neutrino oscillation experiments to measure "electron neutrino appearance" and "muon neutrino survival" rates in a muon neutrino beam.

Are neutrinos Dirac or Majorana particles?

Dirac particles are characterised by being different from their antiparticles, whilst Majorana particles are the same as their own antiparticles. The charge conjugation explained in the previous section transforms a particle into its antiparticle. Therefore it is straightforward that charged particles cannot be Majorana since their charge would flip sign under charge conjugation resulting in an antiparticle that, at least, has opposite charge when compare to its particle. The properties of neutrinos allows them to be either Dirac or Majorana particles. Many experiments, such as SuperNEMO [30], are trying to determine the nature of neutrinos by trying to observe a neutrinoless double beta decay ($0\nu\beta\beta$). This interaction is characterised by the production of two electrons and by the absence of neutrinos, as shown in Figure 2.7. The interactions vertices in Figure 2.7 are written according to the SM, which means that both beta decays produce an electron and a left-hand chiral neutrino. This signature can only be observed if neutrinos are Majorana particles. The "X" connecting the two neutrinos is the so called "Majorana mass insertion".

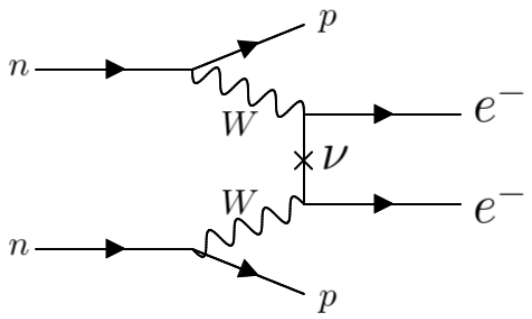

Figure 2.7: Feynman diagram of a neutrinoless double beta decay.

How do neutrinos get mass?

The neutrino oscillation phenomenon can only be described by the SM if neutrinos have a non-null mass, because oscillation probability is zero if neutrinos are massless, as shown in Equation 2.24. In theory, the standard approach to introduce a mass term to the particles is via the Higgs mechanism. The Higgs mechanism works for all quarks and charged leptons because they are Dirac particles, which means they have both a left-hand and right-hand chiral components. Having both chiralities is a requirement for the Higgs mechanism because the mass term is a result of the

simultaneous Higgs coupling with both the left-hand and right-hand components. This mass term is called "Dirac mass".

As mentioned, neutrinos are neutral left-hand chiral particles, and for this reason the standard Higgs mechanism does not directly work for them. However we know neutrinos have mass, therefore there is an effort in the theoretical particle physics to find a way to introduce a mass term for neutrinos as well. One of the solutions is to manually introduce a right-hand chiral neutrino that would not interact via weak force, which is in agreement with experimental observations. This solution implies that neutrinos are also Dirac particles, allowing the creation of a Dirac mass term for neutrinos as well.

It is also possible to introduce a Majorana mass term to neutrinos. A Majorana mass term does not require the existence of a right-hand chiral neutrino. As the name suggests, this solution applies in the scenario where neutrinos are Majorana particles. If neutrinos are Majorana particles, reactions that do not conserve flavour lepton number, such as neutrinoless double beta decays, are allowed. However the SM predicts conservation of flavour lepton number, and for this reason a Majorana mass term to neutrinos is not allowed in the SM.

The second solution is called the Seesaw Mechanism [31]. Again, this solution imposes the existence of a right-hand chiral neutrino, but now this particle is considered very heavy. In addition to the imposition of an Unitarian Lagrangian, a very heavy right-hand chiral neutrino results in a very light left-hand neutrino, as observed experimentally. The mass of this new right-hand chiral neutrino particle is so high that this particle has not been observed yet.

Neutrino mass hierarchy and absolute mass scale

Another open question in neutrino physics regards determining the order of the neutrino masses, i.e. which one is the heaviest and which one is the lightest, which is still unknown.

The sign of $\Delta m^2_{21} \sim 7 \times 10^{-5}\text{eV}^2 > 0$ was the only one to be measured, since states ν_1 and ν_2 are dominated by ν_e. Despite knowing the magnitude of $|\Delta m^2_{32}| \sim 2 \times 10^{-3}\text{eV}^2$, its sign is still unknown [20]. For this reason it is not possible to establish which mass eigenstate is the heaviest. The two possible scenarios,

shown in Figure 2.8, are the so called "normal hierarchy" where $m_1^2 < m_2^2 < m_3^2$, and the "inverted hierarchy", where $m_3^2 < m_1^2 < m_2^2$.

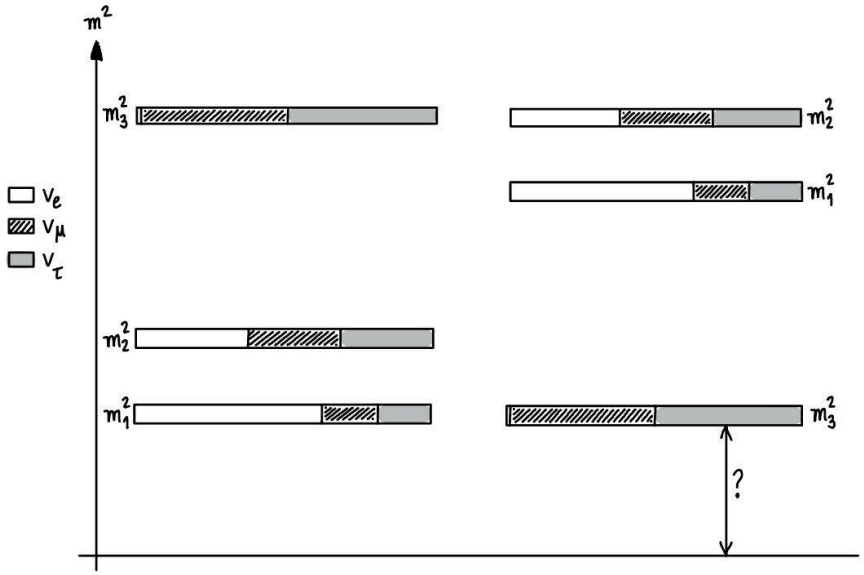

Figure 2.8: The two possible scenarios for the order of the neutrino masses. The "normal hierarchy" (left) describes the scenario where $m_1^2 < m_2^2 < m_3^2$, and the "inverted hierarchy" (right) where $m_3^2 < m_1^2 < m_2^2$. The absolute neutrino mass is also unknown and it is indicated with the question mark at the bottom of the diagram.

Establishing the sign of Δm^2_{21} was possible because of the "matter-effect". The neutrino oscillation *in vacuum* is described by Equation 2.24 as a function of the neutrino mass. However this dependency lives in the term $\sin^2\left(\Delta m^2_{ij} L/4E\right)$ and for this reason measuring the oscillation probability in vacuum is not enough to determine if $\Delta m^2_{ij} \equiv m^2_i - m^2_j$ is positive or negative, since it is a sine squared dependency. On the other hand, the neutrino oscillation probability *in matter* is sensitive to the sign of Δm^2_{ij} due to the Mikheyev-Smirnov-Wolfenstein (MSW) effect [32]. This effect exists because the presence of electrons in matter creates an additional effective potential $V = \sqrt{2} G_F n_e$, where G_F is the Fermi coupling constant and n_e is the number density of electrons in the matter. It is important to note that the matter effect is only noticeable on the ν_e oscillation. This is because the effective potential is a result of the weak interaction between matter and the crossing neutrino, and matter is made up mostly of electrons. The neutral-current weak interaction between neutrinos and electrons is the same for all neutrino flavours, which ends up generating an "overall phase" that has no impact on the oscillation probability. Figure 2.9 shows the Feynman diagram of neutral and charged-current interactions

between neutrinos and matter. On the other hand, charged-current weak interactions between neutrinos and electrons only exist for ν_e, which generates a non-null effective potential only for ν_e.

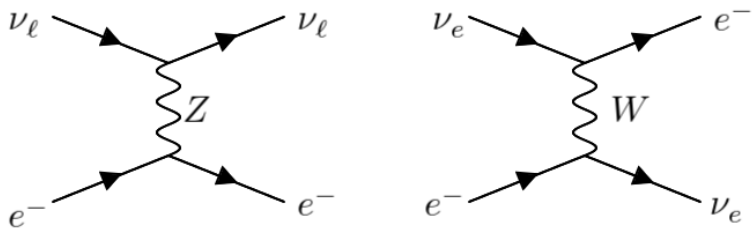

Figure 2.9: Feynman diagrams of the neutrino interactions with matter. Ordinary matter has a much bigger concentration of electrons when compared to muons and taus. For this reason, the charged-current interaction between electron neutrino and electrons (right) is the largest contribution to the matter effect. The neutral-current interaction between neutrinos and electrons (left) happens at same rate regardless of the neutrino flavour and does not contribute to the matter effect.

This potential modifies the hamiltonian of the system to $H = H_0 + V$, where H_0 is the Hamiltonian in vacuum, used to deduce Equation 2.24. This phase shift results in a new oscillation probability given by

$$P_{\text{MSW}}(\nu_\alpha \to \nu_\beta) = \frac{\sin^2 2\theta}{W^2} \sin^2 \left(\frac{\pi L W}{\lambda} \right), \tag{2.33}$$

where

$$W^2 = \sin^2 2\theta + \left(\sqrt{2} G_F n_e \frac{2E_\nu}{\Delta m^2_{ij}} - cos2\theta \right)^2, \tag{2.34}$$

L is the distance travelled by the neutrino, λ is the neutrino oscillation length[6], and E_ν is the neutrino energy [33]. Equation 2.33 shows that the matter effect affects the oscillation probability in a way that it becomes sensitive to the sign of Δm^2_{ij}, because the numerical value of W^2 changes according to the sign of Δm^2_{ij}.

Existence of sterile neutrinos

The Liquid Scintillator Neutrino Detector (LSND) was an experiment located at the Los Alamos Neutron Science Centre aiming to perform neutrino oscillation measurements. In 2001, LSND observations of $\bar{\nu}_\mu \to \bar{\nu}_e$ oscillations showed an excess of

[6]Distance between any closest minima or maxima peaks of the oscillation probability.

events, consistent with $\bar{\nu}_e$ interactions [34]. This excess was above the expected background in a $\bar{\nu}_\mu$ beam, and would correspond to a neutrino oscillation with a parameter Δm^2 orders of magnitude higher than previously measured values of Δm^2_{12} and Δm^2_{23} in the three neutrino model. One possible explanation for this phenomenon is that the observation was actually detecting a fourth kind of neutrino, known as a "sterile" neutrino. This new particle would not interact via the weak force, since measurements of the decay width of the Z^0 resonance led to the current theory of the existence of three active neutrinos.

The MiniBooNE experiment [35] was built at Fermilab to test the LSND result. MiniBooNE operated from 2002 to 2017. MiniBooNE was a Cherenkov detector[7] placed along the Booster Neutrino Beam, one of the main neutrino beams at Fermilab. The detector used 800 tons of mineral oil as the scintillation medium and over 1200 photomultiplier tubes to collect the Cherenkov radiation.

The location of this experiment and the neutrino beam to which it would be exposed were chosen in a way that the ratio $(L/E)_{\text{MiniBooNE}} = 500$ m/700 MeV would be similar to the one that produced the LSND result, $(L/E)_{\text{LSND}} = 30$ m/40 MeV. During its operation period from $2002 - 2017$, MiniBooNE has observed an anomalous excess of electron neutrino events at low energy, as shown in Figure 2.10.

Recent results using the full MiniBooNE dataset confirm the observed low-energy excess. Electron and photons have very similar signatures in a Cherenkov detector. In both cases a fuzzy ring is created, as shown in Figure 2.11. One of the hypotheses is that the observed excess might be photons being misidentified as electrons.

The SBN program [22] at Fermilab consists of a set of experiments that will explore this excess further. These experiments (SBND, MicroBooNE and ICARUS [38]) are all LArTPCs that are sensitive to distinguishing between photons and electrons. For this reason the SBN program should be able to confirm if the excess is indeed caused by misidentified photons.

The necessity of understanding neutrino cross sections

To resolve the open questions mentioned above, current neutrino experiments

[7] Cherenkov detectors are particle detectors that detect the light generated by the Cherenkov radiation when a particle travels faster than light in the medium.

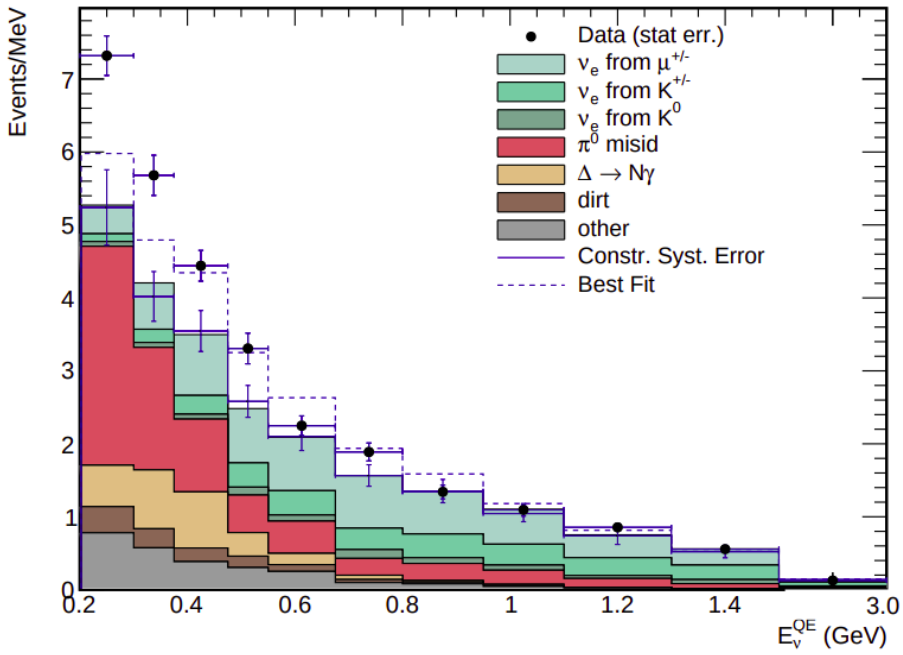

Figure 2.10: Observed ν_e data by MiniBooNE neutrino mode as a function of the reconstructed neutrino energy under charged-current quasielastic (CCQE) scattering, E_ν^{QE}. The dashed histogram shows the best fit to the neutrino-mode data assuming the standard oscillation.
The data points do not match the predicted distribution assuming a standard oscillation model. Figure from [36].

are investing billions of dollars to develop and perfect accurate detection techniques. However, to ensure maximal sensitivity, it is still crucial to understand how neutrinos interact with matter. Once we know how neutrinos interact with matter it will be possible to characterise and measure their precise energy, E, used in the ratio L/E from the oscillation probability.

The two main sources of information required in any neutrino interaction measurement is characterising the incident neutrino flux[8], and being able to identify a neutrino interaction inside the detector. Note that both cases are highly dependent on understanding how neutrinos interact. Therefore, measuring the CP phase, defining the neutrino mass hierarchy and establishing if there is a sterile neutrino depend

[8]Most of the neutrino oscillation experiments consist of two detectors placed along an artificially-made neutrino beam. The neutrino flux referred in this paragraph is the rate of neutrinos from the neutrino beam incident at the detector. If we do not know how neutrinos interact, characterising the incident neutrino flux in situations in which the neutrino source is unknown becomes an almost impossible task.

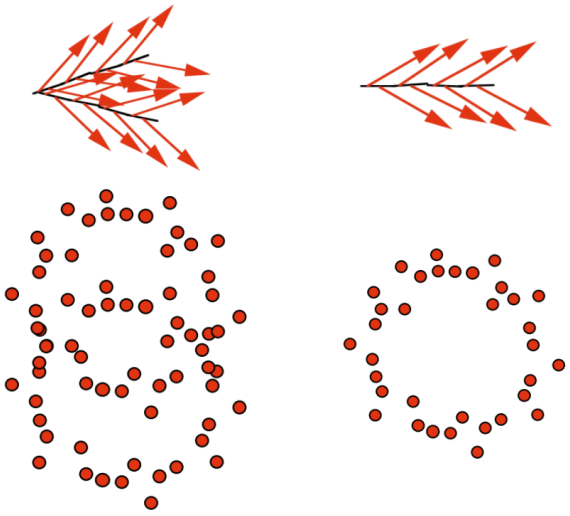

Figure 2.11: Cherenkov signature for photons (left) and electrons (right). The top diagrams show the interactions from a side-view, and the bottom diagrams show the signature in a Cherenkov detector. Both cases create fuzzy rings and the photon-induced signal can be misidentified as an electron-induced signal if there is not enough and/or clear separation between the generated rings. Figure adapted from [37].

on ν_e appearance (and CP also on $\bar{\nu}_e$ appearance). Several of the experiments aiming to perform these measurements use liquid argon as the target medium, mostly because argon is a heavy and abundant element in the atmosphere. Being heavy increases the probabilities of neutrino interactions in the detector, and the fact that argon is abundant in the atmosphere with easy extraction makes its use affordable, which is crucial for large argon detectors. This thesis will show the first combined measurement of the ν_e and $\bar{\nu}_e$ cross section on argon using the MicroBooNE detector at Fermilab.

Chapter 3

Neutrino Interactions

All neutrino oscillation measurements rely on measuring neutrino interactions. In particle physics theory, a particle interaction can be "translated" to a mathematical expression. The terms in this equation will depend on the particles involved and the type of interaction. Each vertex in a Feynman diagram will contribute to a specific matrix Γ made of the product of Dirac γ-matrices. The restriction of being Lorentz invariant results in only five possible combinations of Dirac γ-matrices, called "bilinear covariants": scalar, pseudoscalar, vector, axial vector and tensor [39]. Each case characterises the exchange of a boson with a specific spin. Weak interactions in particular exchange a spin-1 boson and are mathematically described as a linear combination of vector (V) and axial (A) vector currents. However this description is not enough to describe the parity-violating property of the weak interaction. A solution was to introduce the V-A theory [39].

As mentioned, neutrinos can interact with matter via the weak force. This interaction happens via the exchange of the $W^{\pm}$ and Z bosons, and it is known as Charged-Current (CC) and Neutral-Current (NC) interactions, respectively. CC interaction is the only one whose detectable products depend on the incoming neutrino flavour, and for this reason neutrino flavour can only be identified via CC interactions. Understanding these interactions with the nucleus and their products is crucial for studying neutrinos. These mechanisms can be broken down into three main types: Quasi-Elastic (QE), Resonant (RES) and Deep Inelastic Scattering (DIS). Their energy operating regions are distinct. The QE mechanism dominates for low-energy neutrinos from 100 MeV up to 1 GeV. The RES model is significant around a few

GeV. And the DIS effect starts from 2 GeV, becoming the dominant effect for energies of a few GeV. Figure 3.3 shows a global overview of neutrino cross section measurements, broken down into the various interactions modes.

Today, the majority of accelerator-based neutrino experiments operate in the energy regime of a few GeV, where all interaction mechanisms occur, QE, RES and DIS. The relevant interaction mechanisms can be described as follows:

- **Quasi-Elastic Scattering:** is the dominant neutrino interaction mechanism in the low-energy range, from 100 MeV to 1 GeV. The Charged-Current Quasielastic (CCQE) interactions are given by

$$\nu_\ell + n \to \ell^- + p \tag{3.1}$$
$$\bar{\nu}_\ell + p \to \ell^+ + n, \tag{3.2}$$

  where $\ell = e, \mu, \tau$. A Feynman diagram of an interaction is shown in Figure 3.1.

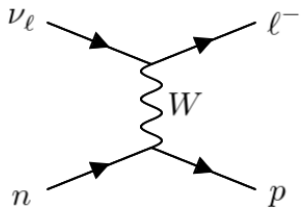

Figure 3.1: Example of a Feynman diagram for $\nu_\ell + n \to \ell^- + p$.

- **Resonant pion production:** happens when the inelastic scattering transfers energy to a nucleon, inciting a short-lifetime resonance excitation that decays emitting pions. This phenomenon happens for higher energy neutrinos in the energy range around and above 1 GeV. The CC interactions are given by

$$\nu_\ell + p \to \ell^- + p + \pi^+, \qquad \bar{\nu}_\ell + p \to \ell^+ + p + \pi^- \tag{3.3}$$
$$\nu_\ell + n \to \ell^- + p + \pi^0, \qquad \bar{\nu}_\ell + p \to \ell^+ + n + \pi^0 \tag{3.4}$$
$$\nu_\ell + n \to \ell^- + n + \pi^+, \qquad \bar{\nu}_\ell + n \to \ell^+ + n + \pi^- \tag{3.5}$$

  where $\ell = e, \mu, \tau$. A Feynman diagram of an interaction is shown in Figure 3.2. Neutrinos can also interact coherently with a nucleus, when a neutrino elastically scatters off an entire nucleus and produces pions. This process is

called coherent (COH) pion production. The CC interactions are given by

$$\nu_\ell + A \to \ell^- + A + \pi^+ \tag{3.6}$$

$$\bar{\nu}_\ell + A \to \ell^+ + A + \pi^- \tag{3.7}$$

where $\ell = e, \mu, \tau$, and A is the nucleus. The Feynman diagram of this process is very similar to Figure 3.2, but this time the entire nucleus is in resonance.

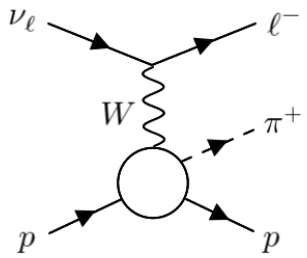

Figure 3.2: Example of a Feynman diagram for $\nu_\ell + p \to \ell^- + p + \pi^+$, where the circle represents the resonance of the nucleon.

- **Deep-Inelastic Scattering:** in the case of high-energy neutrinos with energy above several GeV, neutrinos can resolve the internal structure of a nucleon and interact directly with a quark. As shown in Figure 3.3 this process usually happens for energy above 2 GeV, and it gives linear dependence on energy. This process results in the nucleus breaking apart.

Figure 3.3 summarises the existing measurements of CC muon neutrino and antineutrino cross sections up to about 10^2 GeV. These are the results accumulated over many decades and contain measurements of a variety of nuclear targets and detector technologies. The larger uncertainty at lower neutrino energies is caused by the lack of high statistics data available in this energy range and by the challenges of describing all the physical processes that can participate in this region. Historically there was a larger abundance of neutrino data in comparison to antineutrino, which led to a better cross section measurement of neutrinos than antineutrinos. The helicity suppression is the main cause of the difference in amplitude between neutrino and antineutrino cross sections. However, it should be noted that Figure 3.3 shows results for scattering from nuclear targets, meaning that more complex effects come into play.

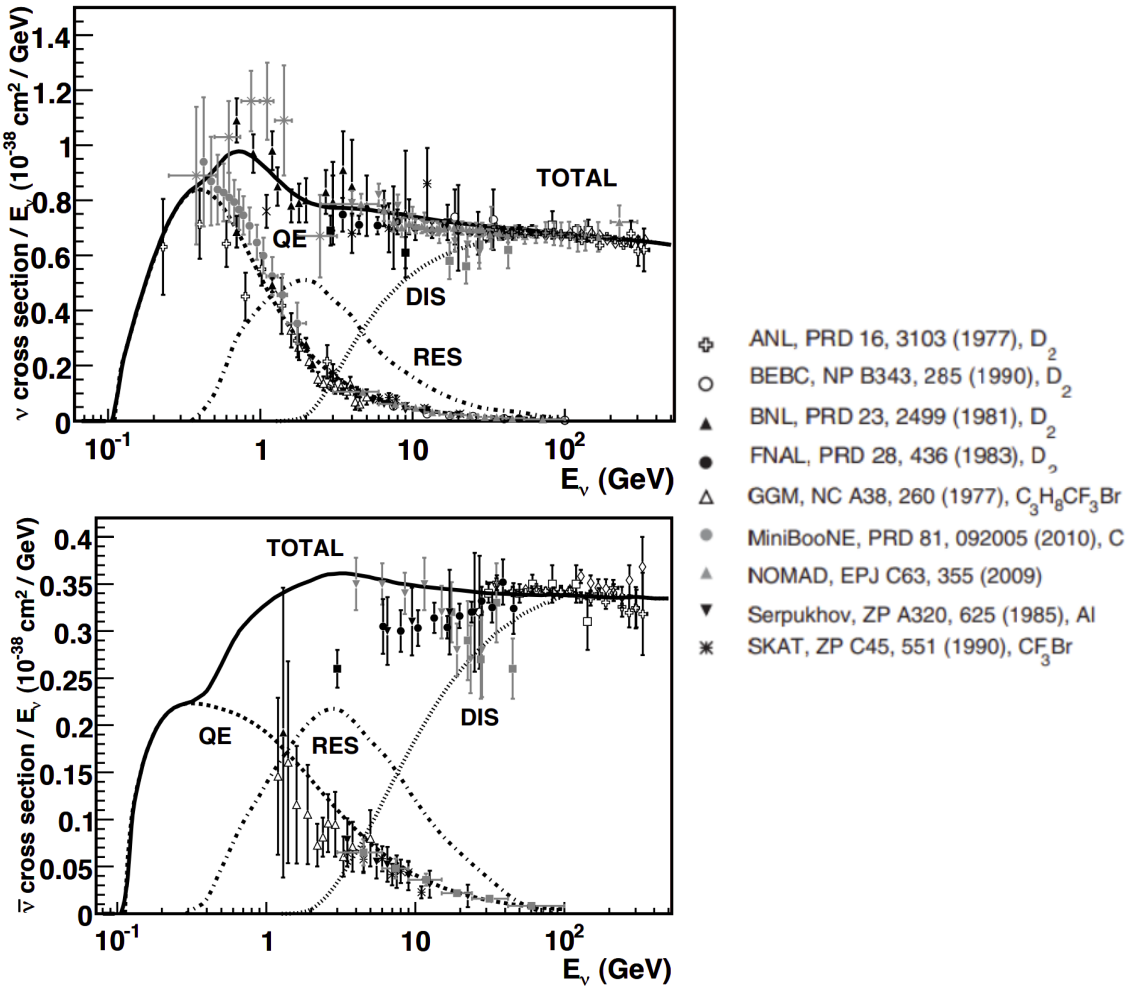

Figure 3.3: Total neutrino (top) and antineutrino (bottom) charged-current cross section per nucleon, divided by the neutrino energy as a function of energy [40]. The prediction for each interaction process is shown as dashed line for quasielastic scattering, dot-dashed line for resonance production and dotted line for deep inelastic scattering. The solid line represents the total prediction.

3.1 Nuclear Effects

The neutrino interactions described in the previous section such as quasi-elastic scattering, resonant pion production and deep inelastic scattering assume that the neutrino interaction happens on free nuclei. In the free nucleus assumption, neutrino interactions are limited to interactions with free protons and neutrons, which is a valid assumption for light targets such as hydrogen. The free nucleus assumption, however, is not a good approximation for experiments using heavier targets such as

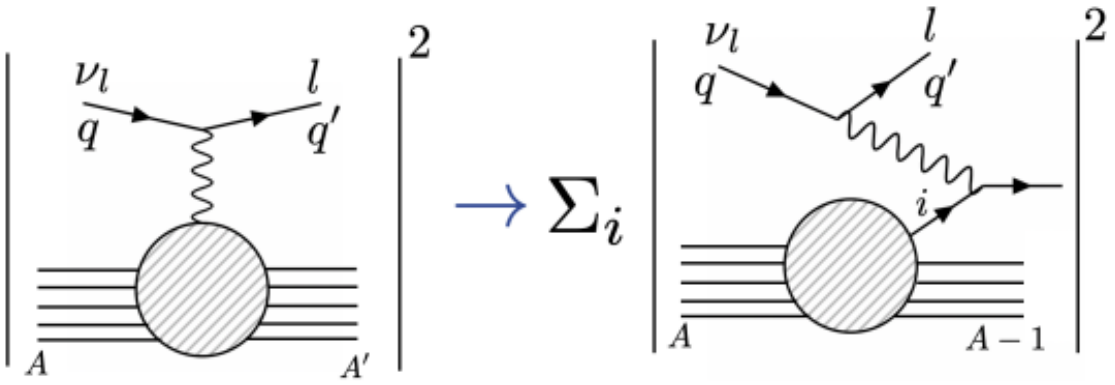

Figure 3.4: Scheme showing how a neutrino scattering on a free nucleon (left) is modified in the impulse approximation (right). This approximation considers the neutrino cross section as being the incoherent sum of elementary processes involving one nucleon. Figure adapted from

[41]

carbon and argon because, in this case, nuclear effect start playing an important role.

Nuclear effects account for extra particle interactions inside the nucleus that modify the final produced particles from an interaction. Heavy targets are therefore a many-body system that is very complicated to solve. This section describes the main elements involved in modelling neutrino interactions with a nucleus.

This thesis uses data collected by the MicroBooNE detector whose target is liquid argon. Therefore the above description of quasi-elastic neutrino interactions is not appropriate. A realistic description of quasi-elastic neutrino interactions with heavy targets, such as argon, can be done using the Impulse Approximation (IA) [41]. In the IA regime the scattering off a nuclear target process is reduced to the incoherent sum of elementary processes involving one nucleon, as shown in Figure 3.4. This approximation is valid under two assumptions: first, it considers that the incoming neutrino has large enough momentum that the target nucleus is seen as a collection of individual nucleons, and second, it considers that the particles produced at the interaction vertex and the recoiling (A-1)-nucleon system evolve independently of one another.

The IA approximation considers the nucleus as a collection of individual nucleons whose dynamics are described by a spectral function. The two main forms for this spectral function are the "global relativistic Fermi gas" and the "local Fermi gas".

The global relativistic Fermi gas treats the nucleus as if they are in a non-interacting constant potential. Whereas the local Fermi gas also includes the local position of the nucleons within the nucleus.

Despite being a better approximation than the free-nucleus assumption, the IA does not include nucleon-nucleon correlations. These correlations, as it has been shown in electron-nucleus scattering experiments [42], can result in nucleon bound states inside the nucleus that modifies the measured cross section. Meson-Exchange Current (MEC) is a generic term used to describe states with n nucleons bond via the exchange of virtual mesons, it has been recently found that the MEC plays a significant role in describing the neutrino interactions. This model has been developed to fix disagreement between data and simulations in the region between QE-dominant and RES-dominant neutrino interactions, around $E_\nu \sim 1\,\text{GeV}$.

The experimental implementation of this effect was tuned using MiniBooNE ν_μCC interactions. [43]. Figure 3.5 shows the prediction with and without MEC. In this case, 2 nucleon correlations are used, also known as 2 particle 2 hole (2p2h). It shows that QE+2p2h is not enough to have a good agreement with data. It is necessary to include an extra correction known as Random Phase Approximation (RPA), that accounts for the average effect of microscopic interactions in a many-body strongly interacting system.

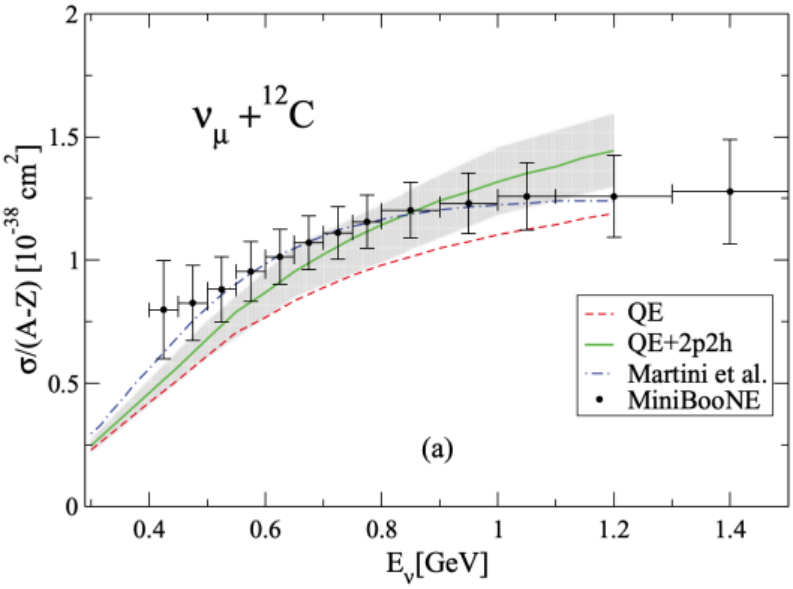

Figure 3.5: MiniBooNE ν_μCC cross section on ^{12}C in comparison to predictions with MEC (green solid), without MEC (red dashed) and Martini *et al.* prediction (dot-dash blue). Figure from [43].

3.1.1 Final State Interactions

Using heavy targets such as argon introduces challenges to simulate the particle interactions. This is because secondary interactions can happen within the large nucleus before the particle escapes, making it impossible to identify the interaction from the primary daughter particles. Figure 3.6 shows an illustration of these effects, also known as Final State Interactions (FSI). In this scheme, an incoming muon neutrino (coming from the right) undergoes a charged-current weak interaction producing a muon and a proton. The produced muon exits the nucleus intact without undergoing secondary interactions, however the produced proton undergoes secondary interactions (such as elastic scattering, pion production) producing secondary daughter particles along the way. The detector can only detect the particles exiting the nucleus, which means that, from the detector point of view, the interaction in Figure 3.6 produced 1 muon, 2 protons, 2 negative pions, 1 positive pion and 1 neutron, which is a signature very different than the one expected for a muon neutrino undergoing a CCQE weak interaction.

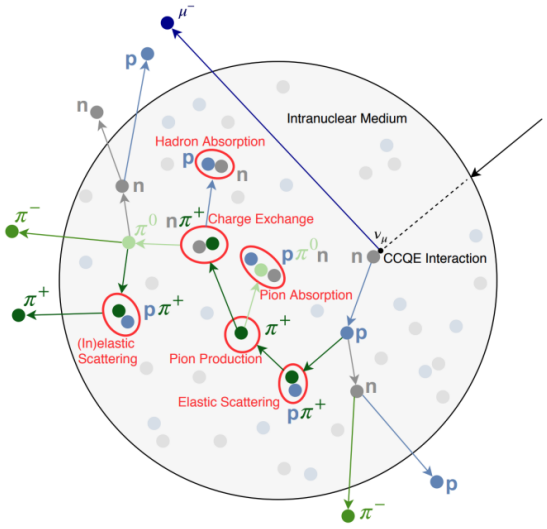

Figure 3.6: Sketch of possible interactions within the nucleus after an initial neutrino-nucleus interaction, and its final state particles. Figure from [44].

3.1.2 Topological classification

The difficulty in identifying interaction mechanisms directly, introduced by the fact that we might not necessarily have access to the primary daughter particles from an interaction, induces the need for topological classification rather than interaction type. A topological classification relies on the signature of the interactions in the detector, for instance, the formation of a long straight track crossing the detector. In this case, rather than labelling reconstructed interactions as CCQE, one classifies them as "1 muon, 1 proton, and 0 pions" ($1\mu 1p0\pi$) for instance.

3.2 Helicity suppression

The neutrino cross section is roughly three times larger than the antineutrino one. This difference is caused by a weak interaction property called "helicity suppression", related to the fact that weak interactions couple with LH chiral particle states and RH chiral antiparticle states.

This section will use the neutrino-electron scattering ($\nu_\mu + e^- \rightarrow \nu_e + \mu^-$) and the antineutrino-electron scattering ($\bar{\nu}_e + e^- \rightarrow \bar{\nu}_\mu + \mu^-$) in the relativistic approximation to illustrate this effect. In the relativistic scenario, chirality and helicity are equivalent, so the weak interaction will only couple with LH helicity particle states and RH helicity antiparticle states. The Feynman diagrams for these scatterings are shown in Figure 3.7, and the graphic representation of their momentum and spin directions in the centre of mass is shown in Figure 3.8.

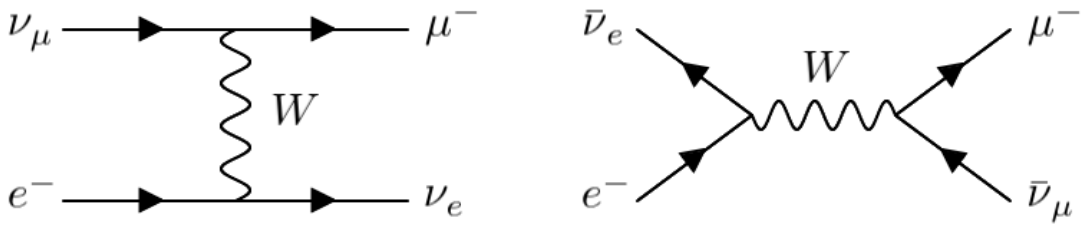

Figure 3.7: Feynman diagram for the neutrino-electron (left) and antineutrino-electron (right) scatterings for a charged-current weak interaction.

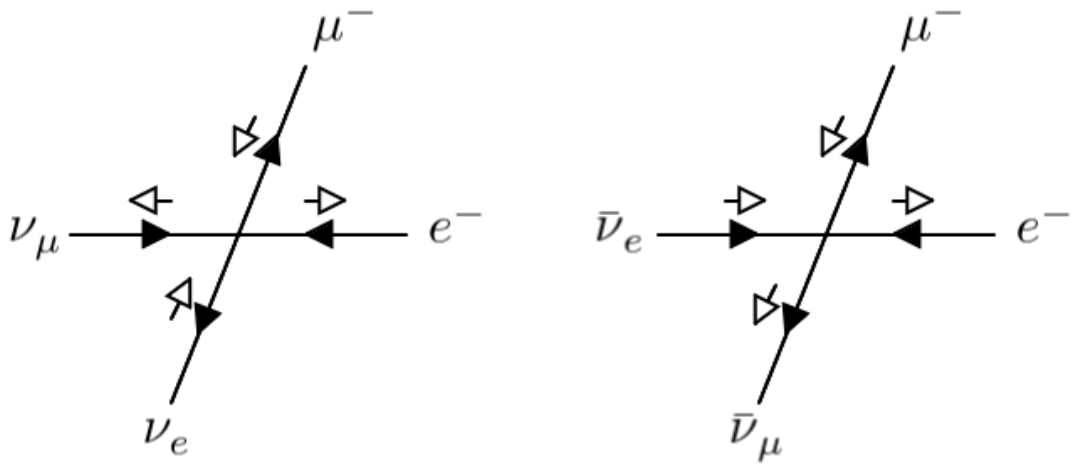

Figure 3.8: Momentum (black arrow) and spin (white arrow) directions represented in the centre of mass of the scattering. In the relativistic approximation, all particles are LH helicity states, and all antiparticles are RH helicity states.

In the neutrino-electron scattering, the initial and final total spin along the interaction axis is 0 ($J_z = 0$), and for this reason the total angular momentum is conserved regardless of the scattering direction. In this case, the differential cross section can be written without any dependency on the scattering solid angle (θ^*) as

$$\frac{d\sigma(J_z = 0)}{dq^2 d\theta^*} \propto \frac{1}{(q^2 - M_W^2)^2}, \tag{3.8}$$

where $1/(q^2 - M_W^2)$ is the mathematical representation of the W-boson propagator, and q and M_W are the four-momentum and mass carried by the W boson [45], respectively.

On the other hand, in the antineutrino-electron scattering, the total spin along the scattering axis is 1 ($J_z = 1$) after the scattering, which adds an angular dependency to this process, and the differential cross section is written as

$$\frac{d\sigma(J_z = 1)}{dq^2 d\theta^*} \propto \frac{1}{(q^2 - M_W^2)^2} \left(\frac{1 + cos\theta^*}{2} \right)^2. \tag{3.9}$$

Equation 3.9 has a maximum at $\theta^* = 0, 2\pi$ and a minimum at $\theta^* = \pi$, as shown in Figure 3.9.

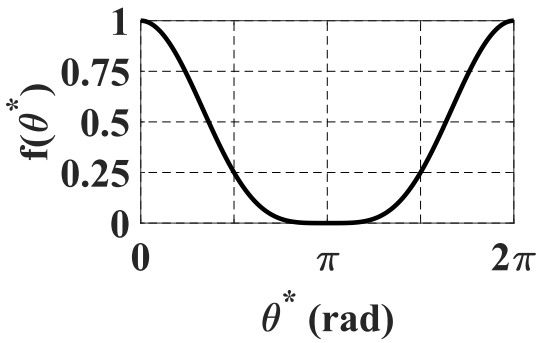

Figure 3.9: Plot of the function $f(\theta^*) = (1/2)^2 (1 + cos\theta^*)^2$ as a function of the angle θ^*.

It is easier to understand the angular dependency in the extreme scenario of a backward scattering process, where $\theta^* = \pi$. In this case, the direction of the outgoing $\bar{\nu}_\mu$ is opposite to the incoming $\bar{\nu}_e$, as shown in Figure 3.10. It is possible to see that the momentum is naturally conserved because it is a representation in the centre of mass, however the spin is flipped. In this case, the backward scattering is not allowed because it does not conserve the total angular momentum along the interaction axis, and indeed Equation 3.9 becomes zero for $\theta^* = \pi$. The same exercise can be done to demonstrate that forward scattering is fully allowed, and that any other scattering angle in between follows the angular dependency shown in Equation 3.9. These demonstrations are out of the scope of this thesis.

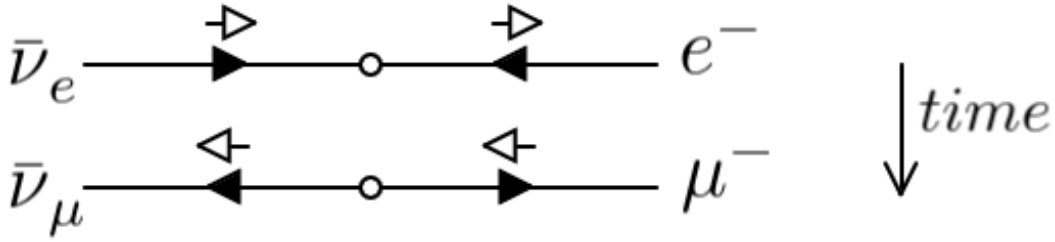

Figure 3.10: Scheme of the antineutrino-electron backward scattering.

Integrating Equations 3.8 and 3.9 over all solid angles leads to $\sigma(J_z = 1) = (1/3)\sigma(J_z = 0)$, where the reduced cross section is a result of the suppression of non-forward scattering due to the projection of spin from the initial to the final state axes. This means that antineutrino cross-sections are expected to be smaller than neutrino ones, which is shown in Figure 3.3, and that forward angles are going to be

preferred in antineutrino interactions.

3.3 Existing Electron Neutrino Cross-Section Measurements

This section describes the existing electron-neutrino cross section measurements. There are only a handful of ν_e cross-section measurements up to date, and most of them do not use argon as a target, like in this analysis.

Gargamelle

The first experiment to publish ν_e and $\bar{\nu}_e$ cross section measurements was Gargamelle in 1978 [46]. Gargamelle was a bubble chamber filled with freon, CF_3Br, located at CERN. The incident neutrino energy range was from 200 MeV to 10 GeV. The detector measured the

$$\nu_e + N \rightarrow e^- + \text{hadrons}, \tag{3.10}$$

$$\bar{\nu}_e + N \rightarrow e^+ + \text{hadrons}, \tag{3.11}$$

processes, with the advantage of being able to distinguish between electrons and positrons due to the presence of a magnetic field.

The cross section was measured by hand-scanning the photos of the interactions, a total of 200 electron and 60 positron events were selected [47]. The measurements found a linear $\nu_e(\bar{\nu}_e)$ cross sections as a function of energy given by

$$\sigma_{\nu_e} = (0.7 \pm 0.2) \times 10^{-38}\, E_\nu\, \text{cm}^2/\text{nucleon} \tag{3.12}$$

$$\sigma_{\bar{\nu}_e} = (0.25 \pm 0.07) \times 10^{-38}\, E_{\bar{\nu}}\, \text{cm}^2/\text{nucleon}. \tag{3.13}$$

T2K

The T2K experiment [25] is a water Cerenkov detector located in Japan. The cross section measurements were performed using the Near Detector (ND280) placed 280 m

away from the neutrino production point.

The T2K experiment has performed two ν_e cross section measurements. The first one was a total flux-averaged cross section of ν_eCC interactions for the average flux energy of $\sim 1\,\text{GeV}$ [48], published in 2014,

$$< \sigma_{\nu_e \text{CC}} >= (1.1 \pm 0.09\ (\text{stat}) \pm 0.18\ (\text{sys})) \times 10^{-38} \text{cm}^2/\text{nucleon}, \tag{3.14}$$

which is in agreement with the one published earlier by Gargamelle.

Then, in 2020, T2K has published a measurement of the electron neutrino and electron antineutrino cross sections using both the neutrino and antineutrino beams, with an average energy of 1.28 GeV and 1.98 GeV respectively [49]. Neutrino beams, as better explained in Section 5.1, can be configured in a neutrino (also known as Forward Horn Current, FHC) and antineutrino mode (also known as Reverse Horn Current, RHC), producing a majority muon neutrino and muon antineutrino beams, respectively. Figure 3.11 shows the differential cross sections with the limited phase-space of $p > 300\,\text{MeV}$ and $\theta \leq 45^0$. The selection chain used to select CC-ν_e and CC-$\bar{\nu}_e$ is very similar. The difference is that, in addition to the selection used for CC-ν_e, the CC-$\bar{\nu}_e$ selection has an extra set of cuts dedicated to remove proton background.

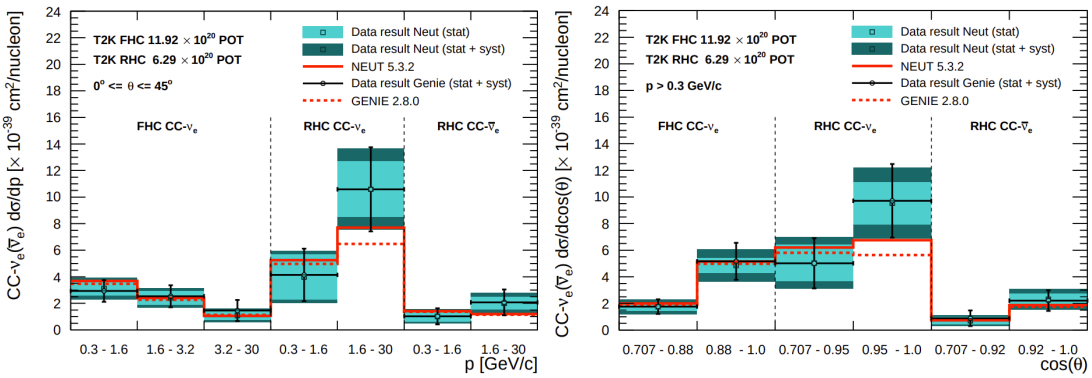

Figure 3.11: Flux integrated electron neutrino and antineutrino charged-current inclusive total
cross sections as a function of momentum (left) and angle (right). Figure from [49].

The reason why the "FHC CC-ν_e" is smaller than the "RHC CC-ν_e" cross sections in value is because the neutrino energy spectrum peaks at higher energy for RHC and it is much broader with larger contribution from higher energy neutrinos. The average neutrino energy is 1.28 GeV for FHC and 1.98 GeV for RHC.

MINERνA

Shortly after the first T2K paper, MINERνA released a ν_eCC cross-section measurement [50]. MINERνA was a detector located at Fermilab made of layers of parallel scintillator strips. The detector is on-axis to the NuMI beam, created by 120 GeV protons colliding on a graphite target, resulting in a neutrino beam of energy of 3.1 GeV. The detector is not able to differentiate between ν_e and $\bar{\nu}_e$ interactions, and for this reason the reported result is the combined $\nu_e + \bar{\nu}_e$ cross section.

MINERνA has performed and reported a "CCQE-like" measurement. CCQE-like is an event with a prompt electron or positron from the primary vertex plus any number of nucleons, but without any other hadrons or γ-ray conversions. The reported cross section on hydrocarbon, shown in Figure 3.12, was calculated as a function of the squared four-momentum transfer Q^2_{QE} based on 2105 ν_e CCQE-like candidates with an average energy of 3.6 GeV.

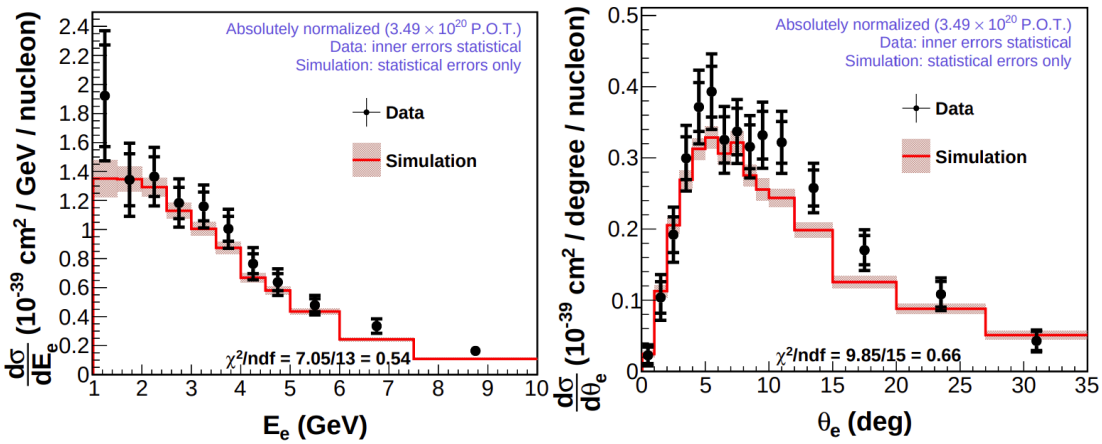

Figure 3.12: Flux-integrated differential ν_e CCQE-like cross section on hydrocarbon versus electron energy (left) and electron angle (right). Neutrino interactions are simulated using the GENIE 2.6.2 event generator.

Figure from [50].

ArgoNeuT

ArgoNeuT was the first experiment to report the electron-neutrino cross section on argon, in 2020 [51]. ArgoNeuT was a small-scale LArTPC located at Fermilab. The experiment was on-axis to the NuMI beam, the same one used by MINERνA. Unable

to distinguish between ν_e and $\bar{\nu}_e$, it has reported a combined $\nu_e + \bar{\nu}_e$ cross section on argon based on 13 selected events of

$$< \sigma >= \left(1.04 \pm 0.38\ (\text{stat})^{+0.15}_{-0.23}\ (\text{sys})\right) \times 10^{-36}\text{cm}^2. \tag{3.15}$$

The differential cross section as a function of the outgoing electron angle is shown in Figure 3.13, with an average energy of $< E_{\nu_e} >= 4.3\,\text{GeV}$ and $< E_{\bar{\nu}_e} >= 10.5\,\text{GeV}$.

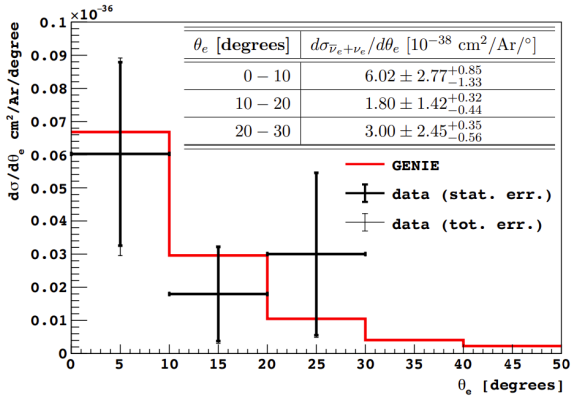

Figure 3.13: Differential $\nu_e + \bar{\nu}_e$ cross section on argon as a function of the outgoing electron angle, measured by the ArgoNeuT experiment. Figure from [51].

MicroBooNE

MicroBooNE is another LArTPC located at Fermilab that has recently published three electron neutrino cross-section measurements on argon. MicroBooNE is located in a way that the detector benefits from collecting data from two neutrino beams, it is on-axis to the Booster Neutrino Beam (BNB) and off-axis to the NuMI beam. The on-axis beam BNB is made mostly of muon neutrinos, whilst the off-axis beam NuMI has a larger fraction of electron neutrinos. This effect is commonly known as off-axis electron neutrino enhancement, more details on Section 5.3. In 2021 MicroBooNE published the first inclusive $\nu_e\text{CC} + \bar{\nu}_e\text{CC}$ cross section on argon using NuMI data, for neutrino energies above 250 MeV, and an average energy of 905 MeV [52]. The measurement was performed based on 80 selected candidates and gives a cross section on argon of

$$< \sigma >= (6.84 \pm 1.51\ (\text{stat}) \pm 2.33\ (\text{sys})) \times 10^{-39}\text{cm}^2/\text{nucleon}. \tag{3.16}$$

Shortly after, in 2022, MicroBooNE published the first measurement of the inclusive ν_eCC and $\bar{\nu}_e$CC differential cross section in charged lepton energy on argon using the NuMI beam [53]. This cross section measurement, shown in Figure 3.14, was performed with a much larger statistics of 243 ν_eCC + $\bar{\nu}_e$CC candidates.

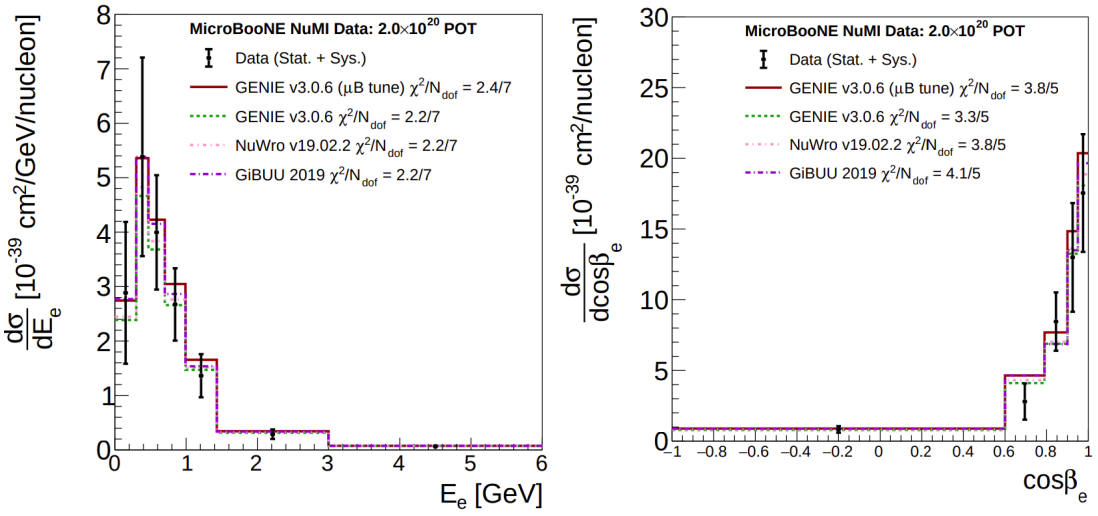

Figure 3.14: Differential cross section on argon as a function of the electron energy (left) and angle (right), measured by the MicroBooNE experiment. The angle β_e represents the electron's deflection from the neutrino direction. Figure from [53].

Later in 2022, MicroBooNE published the first exclusive ν_eCC cross section on argon using the BNB data [54]. The signal is defined as ν_eCC interactions with an electron energy above 30 MeV and without charged pions with kinematic energy $KE_{\pi^\pm} > 40$ MeV or any neutral pions. The events with visible protons ($KE_p \geq 50$ MeV) are defined as $1eNp0\pi$, and the events with visible protons ($KE_p < 50$ MeV) or no protons existing the nucleus are defined as $1e0p0\pi$. The cross section was performed with 111 $1eNp0\pi$ and 14 $1e0p0\pi$ events. The result is reported as a function of the electron and the leading proton, as shown in Figures 3.15 and 3.16 respectively.

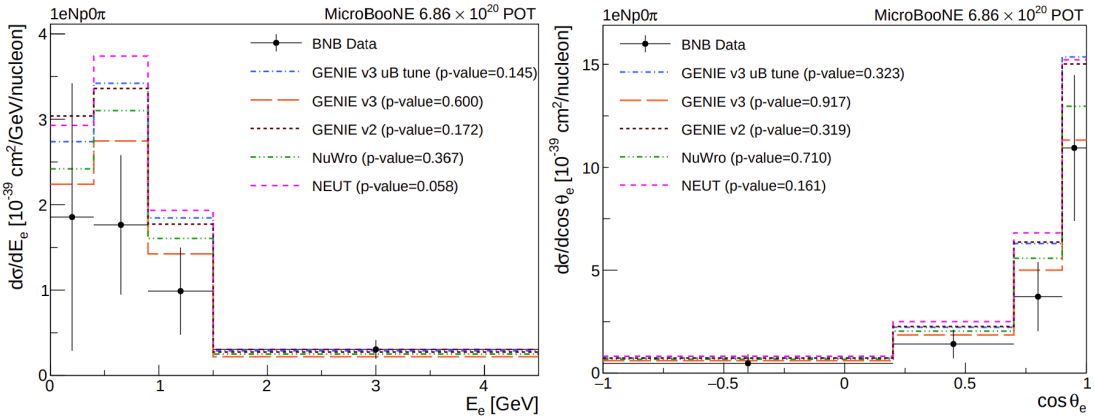

Figure 3.15: Differential cross section on argon as a function of the electron energy (left) and angle (right) for interactions with one electron, N visible protons and no pions, defined as $1eNp0\pi$, measured by the MicroBooNE experiment. The angle θ_e represents the angle between the neutrino beam and electron direction. Figure from [54]. The "p-value" is the probability value

.

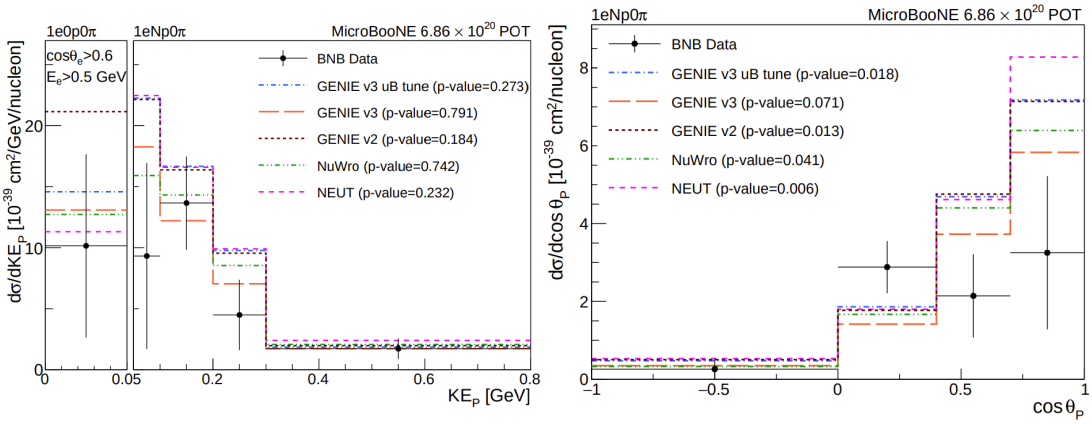

Figure 3.16: Differential cross section on argon as a function of the leading proton energy (left) and angle (right) for interactions with one electron, N visible protons and no pions, defined as $1eNp0\pi$, measured by the MicroBooNE experiment. The angle θ_p represents the angle between the neutrino beam and the leading proton direction.

Figure from [54]. The "p-value" is the probability value.

NOνA

Also in 2022, the experiment NOνA published the ν_e-nucleus[1] [55]. charged-current double-differential cross section [55]. The detector is located at Fermilab, off-axis to

[1]The NOνA near detector is segmented into cells filled with a blend of 95% mineral oil and 5% pseudocumene with trace concentrations of wavelength shifting fluors. The resulting composition

the NuMI beam and is made of grained liquid scintillator detectors. Electron neutrino candidates are identified by the presence of an electron in the final state that produces an electromagnetic cascade within the detector. The double differential cross section as a function of the electron angle and energy is displayed in Figure 3.17.

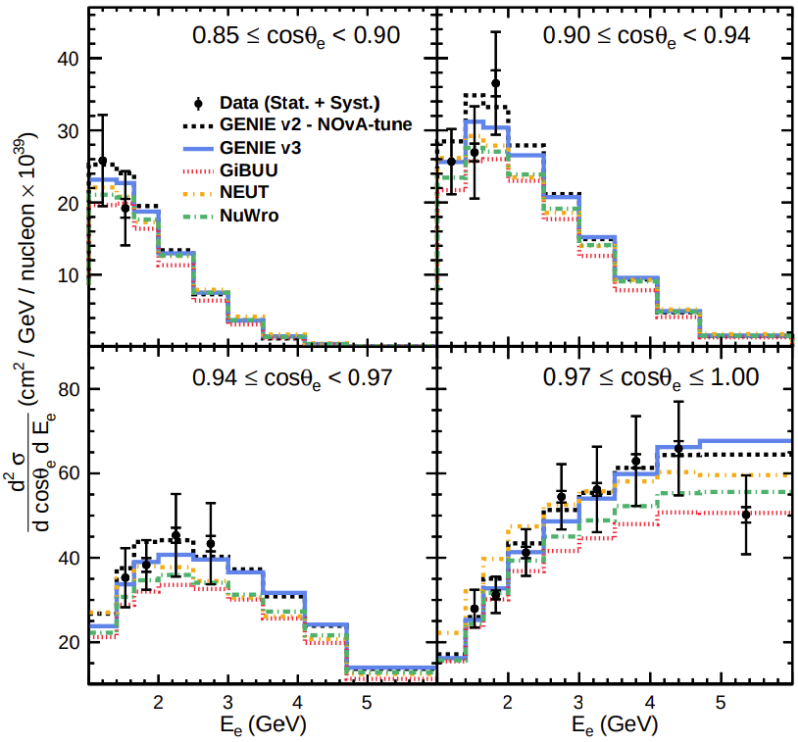

Figure 3.17: Double differential cross section on carbon as a function of the electron angle and energy, measured by NOνA. Figure from [55].

3.3.1 Summary

The existing measurements of this cross section on argon and their properties are summarised in Table 3.1. This work provides the next point by measuring the electron neutrino and antineutrino cross sections on argon, the latter for the first time, using the MicroBooNE detector.

It is not possible to directly compare the measurements in Table 3.1 because they were performed using different neutrino energies. Despite that, all of these results were compatible with the neutrino generators used in simulation.

by mass is 67% carbon, 16% chlorine, 11% hydrogen, 3% titanium, 3% oxygen with other trace elements

Measurement	Description
ArgoNeuT (2020) [51]	- NuMI beam - average energy of $< E_{\nu_e} >= 4.3\,\text{GeV}$ and $< E_{\bar{\nu}_e} >= 10.5\,\text{GeV}$ - differential $d\sigma_{\nu_e+\bar{\nu}_e}/d\phi_e$ - 13 selected candidates
MicroBooNE (2021) [52]	- NuMI beam - neutrino flux energy of 905 MeV - inclusive $\sigma_{\nu_e+\bar{\nu}_e}$ - 80 selected candidates and an average
MicroBooNE (2022) [53]	- NuMI beam - average energy of $< E_{\nu_e} >= 768\,\text{MeV}$ and $< E_{\bar{\nu}_e} >= 961\,\text{MeV}$ - inclusive differential $d\sigma_{\nu_e+\bar{\nu}_e}/dE_e$ and $d\sigma_{\nu_e+\bar{\nu}_e}/d\cos\beta_e$ - 243 selected candidates
MicroBooNE (2022) [54]	- BNB beam - average energy of 0.8 GeV - exclusive differential $d\sigma_{\nu_e}/dE_e$ and $d\sigma_{\nu_e}/d\cos\theta_e$ (14 $1e0p0\pi$ selected candidates) - differential $d\sigma_{\nu_e}/dK_p$ and $d\sigma_{\nu_e}/d\cos\theta_p$ (111 $1eNp0\pi$ selected candidates)

Table 3.1: Summary of the existing electron neutrino cross-section measurements on argon.

Chapter 4

The MicroBooNE LArTPC Detector

LArTPCs are a technology increasingly used in experimental neutrino physics. The MicroBooNE, the detector used in this analysis, is a LArTPC located at Fermilab. This chapter covers the LArTPC working principle followed by a description of the MicroBooNE detector, and its readout and trigger systems.

4.1 Liquid Argon Time Projection Chambers

A LArTPC consists of a volume of pure Liquid Argon (LAr) placed between cathode and anode planes, as shown in Figure 4.1, that create and maintain a strong and constant electrical field of the order of a few hundred of V/cm along the detector.

When a charged particle crosses the detector, the liquid argon volume is ionised creating a trail of electrons along the particle's trajectory. The electric field causes a number of these ionised electrons to drift towards charge-sensitive electronics, as shown in Figure 4.1, whilst the rest of them recombine with the ionised argon atoms resulting in scintillation light. This light is produced isotropically and detected by photo-sensitive detectors in a matter of nanoseconds, whilst the ionised electrons take much longer to drift and to be detected- on the order of milliseconds in a detector of MicroBooNE's dimensions. Because the light is detected almost instantly after the interaction, its arrival time, t_0, is used to determine the start time of an interaction

in the detector. The detection of the drifted ionised electrons is done via a set of three wire planes (U, V, Y as shown in Figure 4.1) located opposite to the cathode plane, and the scintillation light is captured via 32 Photomultipliers (PMT) installed behind those wire planes. A more detailed explanation of these detection systems is given in Section 4.2.

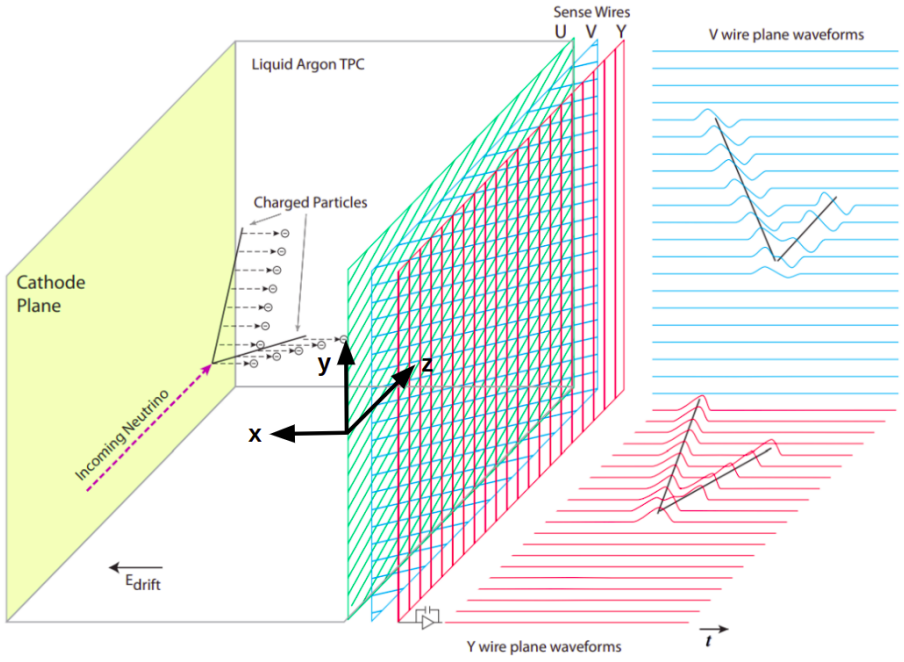

Figure 4.1: LArTPC working principle scheme. Figure adapted from [56]. The displayed coordinate system shows the "origin" of the system. The X and Z coordinates are often referred to as "drift direction" and "beam direction", respectively

.

Neutral particles such as neutrinos are not directly detectable in LArTPC detectors because their passage in the detector does not induce ionisation. The only way to detect them is indirectly by reconstructing all the charged daughter particles generated from their interaction with an atom in the medium. Therefore, a precise understanding of the detector effects on either the particle (electron, ion, photon) collection or detection process, and a high efficiency in detecting the visible particles, is crucial to correctly understand neutrino interactions.

4.1.1 Liquid argon

Argon is a good detector material because it is an abundant element in the atmosphere, easy to obtain and purify, making LArTPCs relatively affordable detectors. In neutrino detectors, it is important that the target material is dense to increase the probability of neutrinos interacting within the detector given the neutrino's small cross section. Liquid argon offers a better ratio between density ($1.4\,\mathrm{g/cm^3}$) and price, when compared to other materials commonly used in this type of detection, such as xenon (denser than argon, but more expensive) and water (cheaper than argon, but less dense). Noble elements, such as argon, are not electronegative which allows ionised electrons to have a high mobility and achieve long drift distances. Finally, liquid argon is transparent to its own scintillation light [57], resulting in high photon detection probability.

4.1.2 Scintillation Light

Liquid argon is an excellent scintillator: in an electric field of $E = 500\,\mathrm{V/cm}$ it produces around 2×10^4 photons per MeV of deposited energy. The amount of photons emitted per energy deposited is also known as "scintillation yield" (SY).

The scintillation light emission relies on producing a short-lived excimer Ar_2^* via two processes: self-trapped exciton luminescence and recombination luminescence, as shown in Figure 4.2. In the *self-trapped exciton luminescence* process, the production of the excimer Ar_2^* happens through an induced excitation of the medium with the passage of a charged particle in the detector. In the *recombination luminescence* process, the production of the excimer Ar_2^* occurs when the ionised electrons recombine with the positive Ar atoms. In both processes the excimer Ar_2^* can be produced in either the singlet (${}^1\sum_u$) or triplet (${}^3\sum_u$) state.

The scintillation light itself is emitted through the decay process of the excimer Ar_2^*

$$Ar_2^* \rightarrow 2Ar + \gamma, \tag{4.1}$$

with two exponentially-decaying photon emission profiles, one with a fast decay component of $\tau_s \approx 6\,\mathrm{ns}$ from the singlet state (${}^1\sum_u$) decay, and another one with a slow decay component of $\tau_t \approx 1500\,\mathrm{ns}$ from the triplet state (${}^3\sum_u$) decay, as

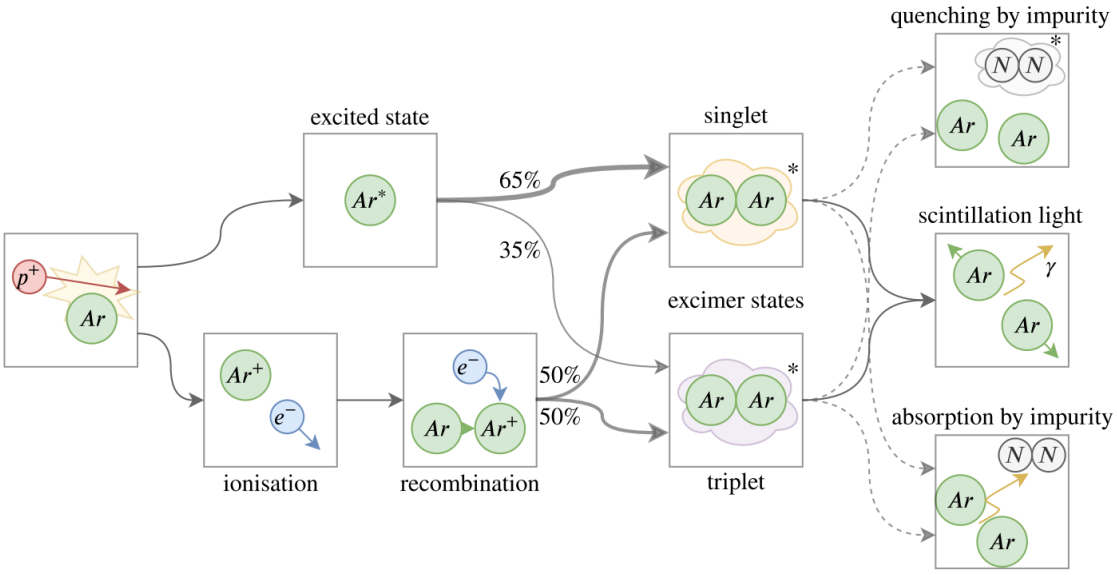

Figure 4.2: Scintillation light processes in liquid argon: self-trapped exciton luminescence (top) and recombination luminescence (bottom). Both processes produce singlet and triplet excimers of Ar_2^* that decays producing the liquid argon scintillation light of 128 nm wavelength (Ref. [58]).

shown in Figure 4.3. In both decays the emission spectrum peaks in the Vacuum Ultra-Violet (VUV) region at 128 nm [59].

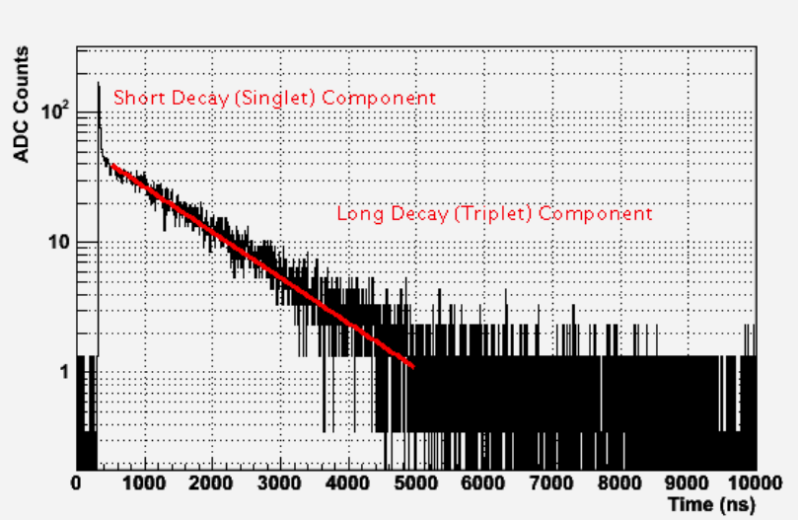

Figure 4.3: Liquid argon scintillation light recorded during tests done by the WArP collaboration. This waveform displays both, the fast decay component resulting from the singlet state decay, and the slow decay component resulting from the triplet state decay. Figure from [60].

The scintillation light intensity is highly sensitive to the concentration of contaminants in the liquid argon, as processes like quenching and absorption become more frequent as contamination increases. An oxygen purity level smaller than 0.1 ppm is required for an optimal LArTPC functioning [61], for instance.

4.1.3 Ionisation Charge

In addition to producing scintillation light, the passage of charged particles in the detector also produces ionised electrons along their path caused primarly by Coulomb scattering with atomic electrons. The mean rate of energy loss of a passing charged particle is well described by the Bethe-Bloch equation given by:

$$\left\langle -\frac{dE}{dx} \right\rangle = Kz^2 \frac{Z}{A} \rho \frac{1}{\beta^2} \left[\frac{1}{2} \ln \left(\frac{2m_e^2 c^2 \beta^2 \gamma^2 W_{max}}{I^2} \right) - \beta^2 - \frac{\delta(\beta\gamma)}{2} \right], \qquad (4.2)$$

where $K = 0.307075\,\mathrm{MeV\,g^{-1}\,cm^2}$ is a numerical conversion factor, z is the number of unit charge of the ionising radiation, Z, A and ρ are the atomic number, mass number and density of the medium, $\beta = v/c$, $\gamma = (1-\beta^2)^{-1/2}$, m_e is the electron mass, W_{max} is the maximum kinematic energy transferred to a free electron in a collision, I is the mean ionisation potential, and δ accounts for the effects on the energy loss due to the density of the medium [62].

High-energy ($> 100\,\mathrm{MeV}$) electrons and photons will produce an "Electro-Magnetic (EM) shower" in the detector. These showers are characterised by a cascade of secondary particles, as shown in Figure 4.4. A photon-induced EM shower starts with an electron-positron pair being created, and then it evolves as two electron-induced showers. For this reason, one way to distinguish these two events is by analysing the energy loss at the beginning of the shower. In the case of photon-induced showers, the energy loss at the beginning of the shower will be twice that of electron-induced showers.

The ionised electrons drift towards the anode plane under the effect of the electric field, but not all of them arrive at the wire planes. A realistic reconstruction of this process involves understanding a few detector effects:

- **Electron-Ion Recombination:** The ionised electrons can be thermalised by the medium and recombine with Ar^+ ions rather than being drifted until the

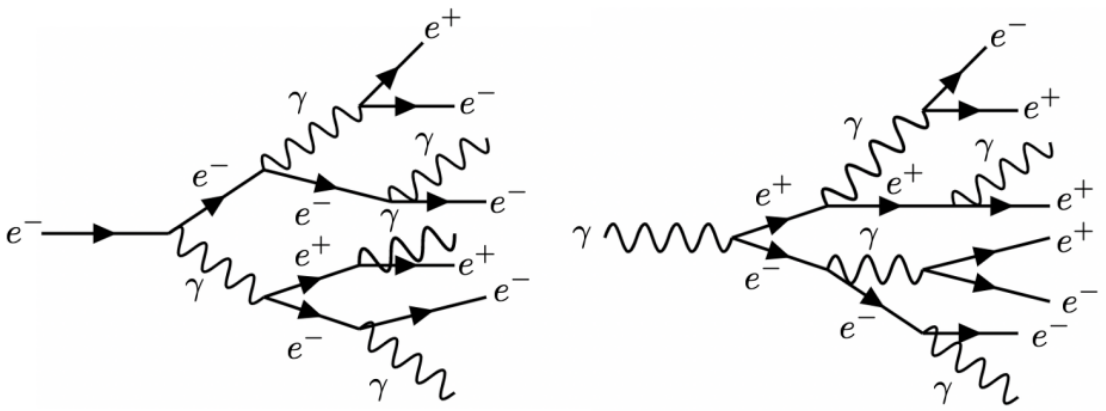

Figure 4.4: Diagram of an electromagnetic shower induced by an electron (left) and by a photon (right). Figure from [63].

anode by the electric field. As a result not all of the ionised electrons produced at the beginning of this process are detected on the wire planes. This process introduces a non-linear relationship between the original amount of charge deposited per unit length (dE/dx) and the amount of charge measured per unit length (dQ/dx). The equation describing this effect used by MicroBooNE was developed by the ArgoNeuT collaboration as a modification of the "Box Model"[1] [64], and it is given by

$$\frac{dE}{dx} = \frac{exp\left(\frac{\beta' W_{\text{ion}}}{\rho E}\left(\frac{dQ}{dx}\right)\right) - \alpha}{(\beta'/\rho E)}, \tag{4.3}$$

where β' and α are parameters tuned using experimental data, $W_{\text{ion}} = 23.6\,\text{eV}$ [65] is the ionisation work function of argon, ρ is the liquid argon density and E is the drift electric field.

- **Argon Purity:** The ionised electrons can be captured by electronegative impurities in the liquid argon volume, such as oxygen and water. Therefore the amount of detected charge is highly influenced by the purity level of the argon. The amount of impurities per unit of volume needs to be monitored and purified daily to minimise this effect.

- **Diffusion:** The clouds of electrons spread out in two orthogonal directions

[1]The Box Model describes the recombination process in the detector, it assumes a Gaussian spatial distribution around the particle trajectory during recombination, identical charge mobility for ions and electrons, and negligible electron diffusion and ion mobility in liquid argon during recombination.

during their drift process. This process is non-isotropic because of the presence of the electric field. The transverse diffusion causes the pulse to be wider in the Y-Z coordinates, which decreases the position resolution of the detector. The longitudinal diffusion results in a wider pulse along the drift direction, resulting in an effective longer signal in time. Diffusion has a bigger impact on electrons produced near the cathode, as their drift distance is larger when compared to those produced near the anode, as shown in Figure 4.5.

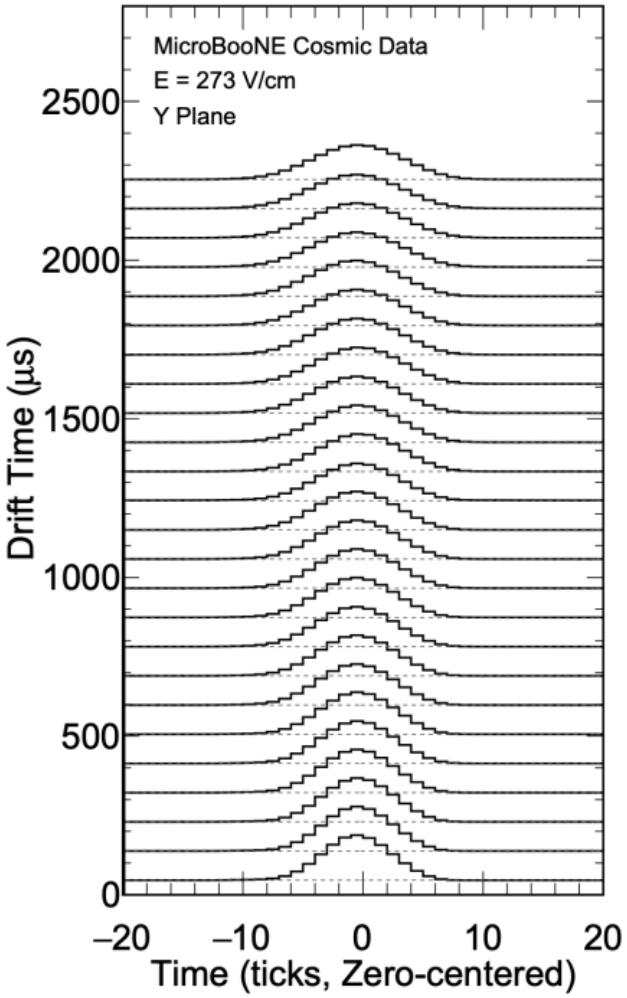

Figure 4.5: Effect of the longitudinal diffusion on the recorded waveform as a function of the drift time. A larger effect is observed on waveforms created closer to the cathode, that have longer drift times until their detection at the anode. Figure from [66].

- **Space Charge Effect:** The ionisation process also creates Ar^+ that are drifted in opposite direction to the electrons, towards the cathode. Due to their slow drift velocity (a few millimetres per second), there are clouds of

positive ions throughout the detector that distort the electric field, making it non-uniform. This is the Space Charge Effect (SCE). As a result the path of the drifting electrons will be diverted and the detector will lose space precision. Figure 4.6 shows the SCE effect in detecting cosmic rays at the MicroBooNE detector. The points represent the interaction location of entering cosmic rays under the assumption of a uniform electric field in the detector. Instead of being on top of the edge of the detector (dashed line), the entry/exit points exhibit an offset from the edges of the Time Projection Chamber (TPC) that increases in magnitude as the track origin point is further from the anode in x [67].

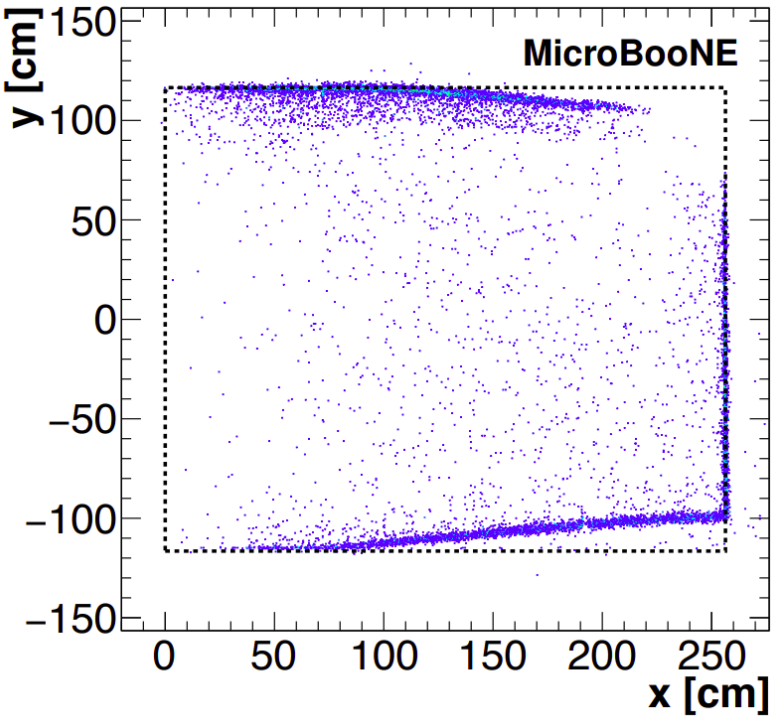

Figure 4.6: Entry/exit points of reconstructed cosmic muon tracks coincident with a signal from a muon counter located outside of the cryostat. In the absence of SCE and the associated non-uniform electric field in the detector volume, the points should be located strictly along the TPC boundaries (dashed lines). The anode is located at $x = 0\,\text{cm}$ while the cathode is at $x = 256\,\text{cm}$. Figure from [67].

4.1.4 Particle Signatures in MicroBooNE

Charged particles crossing a LArTPC detector can create two main kinds of signatures: a track or a shower. Tracks are characterised by a straight line signature, whilst showers are characterised by a particle cascade. Examples of tracks and showers signatures is shown in Figure 4.7.

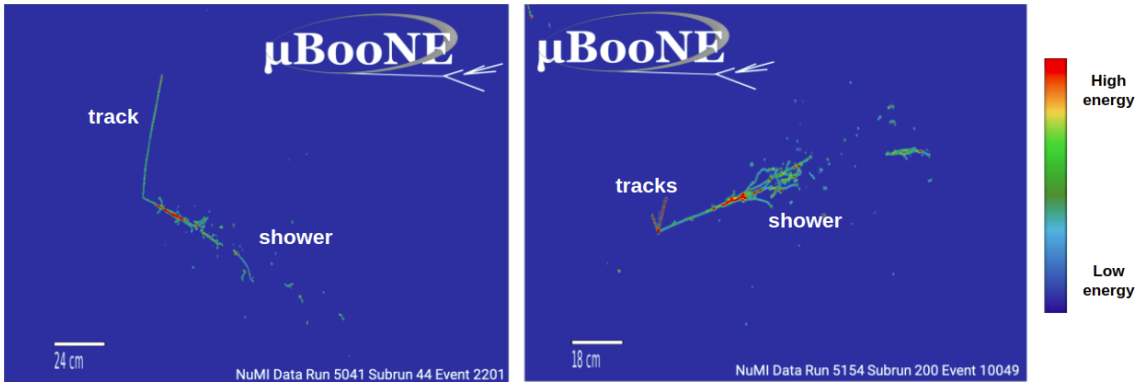

Figure 4.7: Examples of event displays collected by MicroBooNE showing the signal generated by tracks and showers. Figure adapted from [63]. The colour scheme shows the amount of energy deposited, high energy in red and low energy in blue.

Protons, muons and pions are examples of particles that produce **tracks**. The particle identification in this case is done by analysing the energy loss. Protons produced from neutrino interactions have a high dE/dx, and therefore are identified as a short track with high energy deposition. Muons and pions, on the other hand, are produced as minimum ionising particles (MIPs), whose energy loss is a minimum of the Bethe-Bloch formula, and therefore produce long tracks with a medium energy deposition. The Bethe-Bloch formula has a steep increase for low-momentum particles, which means that there is an abrupt energy deposition as particles loose energy during their trajectory.

Electrons, positrons, photons and pions[2], as explained in the previous section, have a different signature. These particles produce **showers**. It is possible to perform particle identification by measuring the amount of deposited energy at the beginning of the shower. Figure 4.8 shows the amount of deposited energy dE/dx by particle type of the leading shower. As explained in the previous section, photon-induced showers have twice the amount of deposited energy at the beginning of the shower

[2]Pions generate showers via their decay into two photons, $\pi^0 \rightarrow 2\gamma$.

when compared to electron-induced ones.

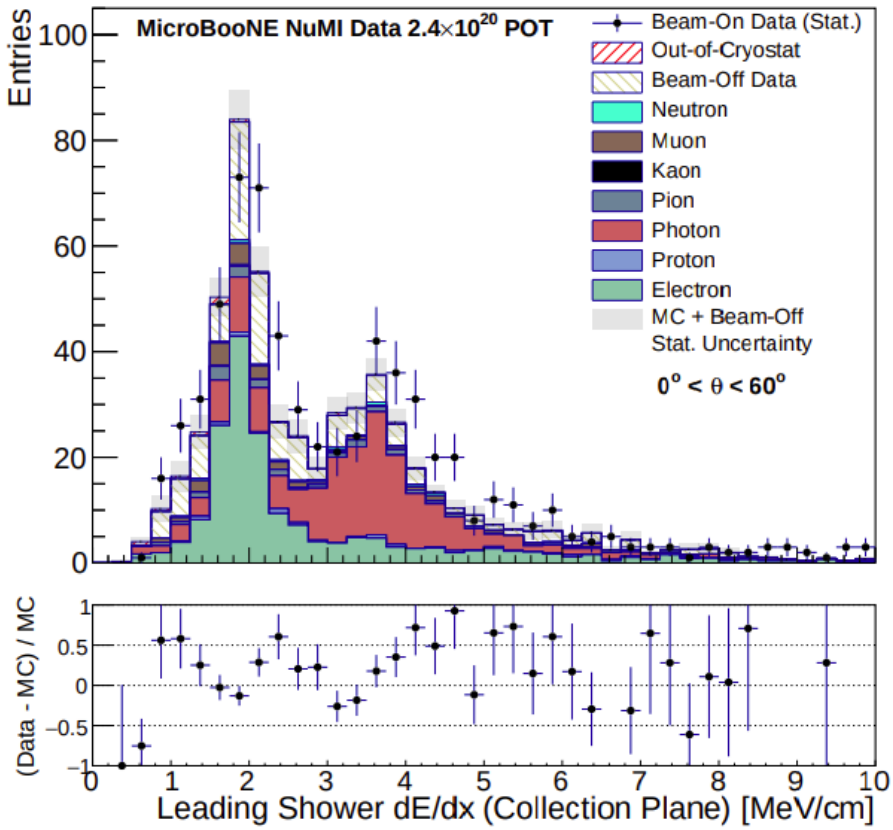

Figure 4.8: The dE/dx for electron neutrino shower candidates split by particle type of the leading shower. The energy deposition is evaluated at the start of the shower. It is possible to see that electron-induced showers peak at 2 MeV/cm, whilst photon-induced showers peak at ∼4 MeV/cm. This distribution is limited to forward-going showers, whose angle with respect to the neutrino beam, θ, ranges from $0^o < \theta < 60^o$. Figure from [63]

.

4.2 The MicroBooNE Detector

The MicroBooNE detector [56] consists of a 2.6 m (width, along the drift direction, x) × 2.3 m (height, along the vertical direction, y) × 10.4 m (length, along the main neutrino beam direction, z) LArTPC placed inside of a cryostat that maintains the working temperature at 87 K, Figure 4.9. The cryostat is filled with 170 tonnes of liquid argon, from which the 87 tonnes inside the TPC is referred to as the "active

volume". Due to technical difficulties, MicroBooNE was not able to set its operation electrical field up to 500 V/cm, and operated with an electric field of $E = 273.9\,\mathrm{V/cm}$.

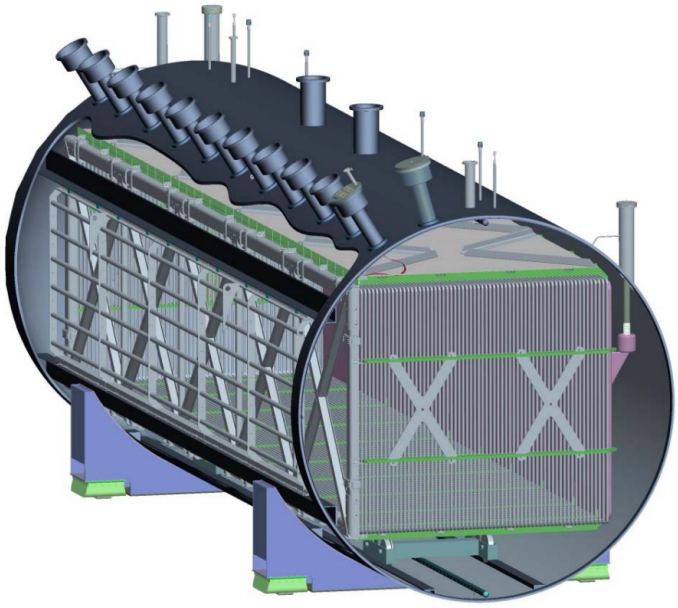

Figure 4.9: Schematic diagram of the MicroBooNE LArTPC. The outer surface represents the cryostat, the the rectangular block inside represents the TPC, volume which defines the "active volume" of the detector. Figure from [56].

Charge Detection System.

The detection of the ionised electrons is performed by 3 charge-sensitive planes at the anode. Each plane is made of thin wires, $\sim 150\,\mu$m in diameter, with a wire pitch of 3 mm. The planes have different orientations, which allows to combine their information to perform a 3-dimensional reconstruction of the particle interaction position inside the detector. Planes U, V and Y are oriented at $\pm 60^0$ and 0^0 with respect to the vertical, respectively, as shown in Figure 4.1.

A voltage of $-70\,\mathrm{kV}$ is applied to the cathode and a different voltage is applied to each wire plane. The first two planes are biased with voltages of $-110\,\mathrm{V}$ (U plane) and $0\,\mathrm{V}$ (V plane) such that the drift electrons pass through the wire planes which induces a bipolar signal on them, as shown in Figure 4.10. These planes are also known as "induction planes" for this reason. The third plane is biased at $230\,\mathrm{V}$ such that the drift electrons are collected producing a unipolar signal. This plane is also known as the "collection plane". The signal generated by each plane is shown in Figure 4.10, and the wire-plane properties are summarised in Table 4.1. Signals from

the wires are sampled with a frequency of 2 MHz. Despite both being "induction planes", the generated signal by planes U and Y have different shapes because there is no "shield plane" in front of the U plane. The disagreement between data and simulation for plane U can be attributed to the finite number of wires that are adjacent to the wire closest to the drifting ionisation electrons. A better agreement is observed using a larger number of those wires, as shown in Figure 4.11.

The signal processing of the collected charge is performed by two sets of electronics, one inside the cryostat (cold electronics) and one outside the cryostat (warm electronics). The cold electronics act as pre-amplifiers with an excellent sensitivity due to the cryogenic temperatures. The pre-amplifiers generate analog signals that are guided out the cryostat to a warm analogue-to-digital converter front-end module.

	U plane	V plane	Y plane
Voltage	−110 V	0 V	230 V
Signal	Bipolar	Bipolar	Unipolar
Number of Wires	2400	2400	3456
Orientation w.r.t vertical	60^o	-60^o	0^o

Table 4.1: Summary of technical information about the wire planes used in the MicroBooNE detector.

Light Detection System.

The light detection system is made of 32 8-inch Hamamatsu PMTs installed behind the anode plane. Glass is not transparent to the 128 nm VUV light emitted by the liquid argon scintillation process, and for this reason direct scintillation light is not detectable by a common PMT. The solution found was to place a plate coated with a thin layer of TetraPhenyl Butadiene (TPB) WaveLength Shifter (WLS) in front of the PMTs, as shown in Figure 4.12. This WLS converts the wavelength of the 128 nm liquid-argon scintillation light to 425 nm, making it detectable by the glass window of the PMT.

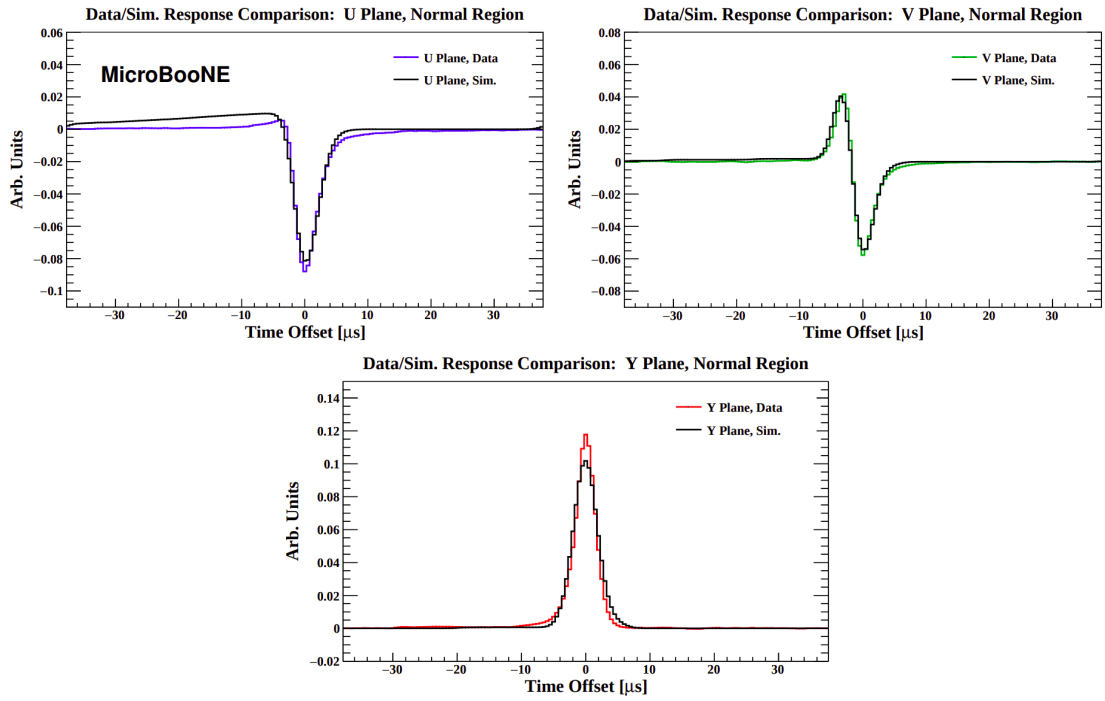

Figure 4.10: Shape of the signals recorded on the U, V and Y planes in MicroBooNE. These signals show the bipolar behaviour of the induction planes, U and V, and the unipolar behaviour of the collection plane, Y. Figure from [68].

4.3 Cosmic Ray Tagger

The Cosmic Ray Tagger (CRT) [69] is a system developed to help identify the cosmic-induced activity inside the detector. Without this tool, cosmogenic muon tracks can be misidentified as ν_μ interactions or, in combination with δ rays, Michel electrons[3] and radiative energy depositions can be misidentified as ν_e interactions. The CRT system is made of scintillation panels installed around the detector, as shown in Figure 4.13.

Each CRT panel is made of many scintillation strips placed in parallel to each other that generate a light signal when there is a crossing particle. A CRT self-trigger system uses cross-module coincidence signals within a 150 ns window to identify crossing muons. The cosmic-induced background activity can be removed when the LArTPC trigger and the CRT trigger are synchronised. Figure 4.14 shows the increase in number of CRT triggers during the beam window, corresponding to the

[3] A Michel electron is an electron produced when a muon decays at rest: $\mu^- \to e^- + \bar{\nu}_e + \nu_\mu$.

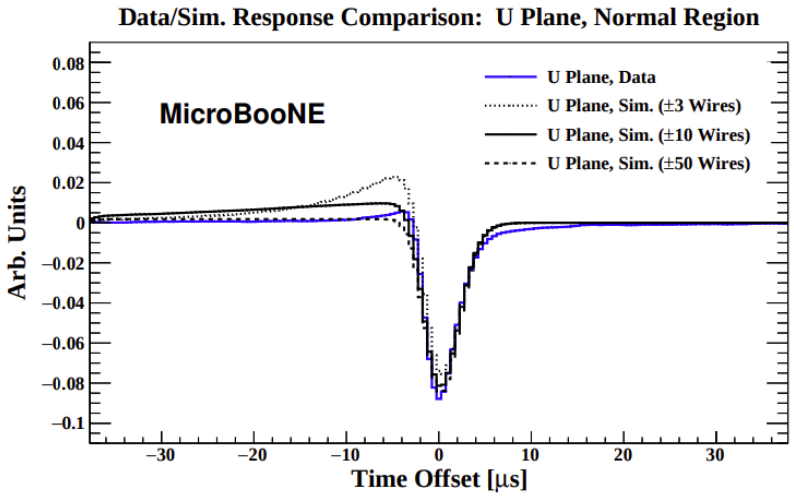

Figure 4.11: Comparison between data and simulation using a variable number of wires adjacent to the wire closest to the ionisation electrons. Figure from [68]

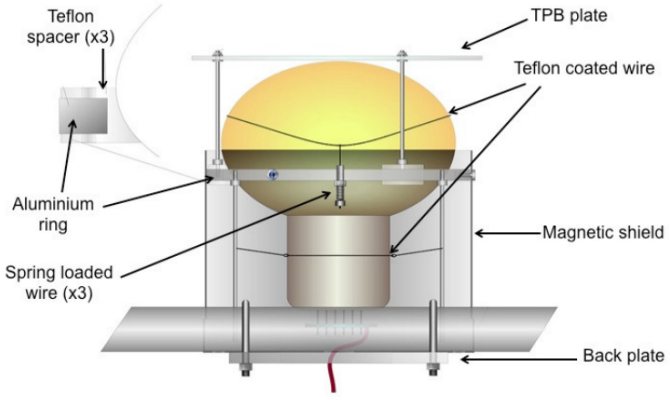

Figure 4.12: A picture of the PMT structure used in the MicroBooNE detector. The acrylic plate is coated with TPB that allows the scintillation light to be detected by the PMT [56].

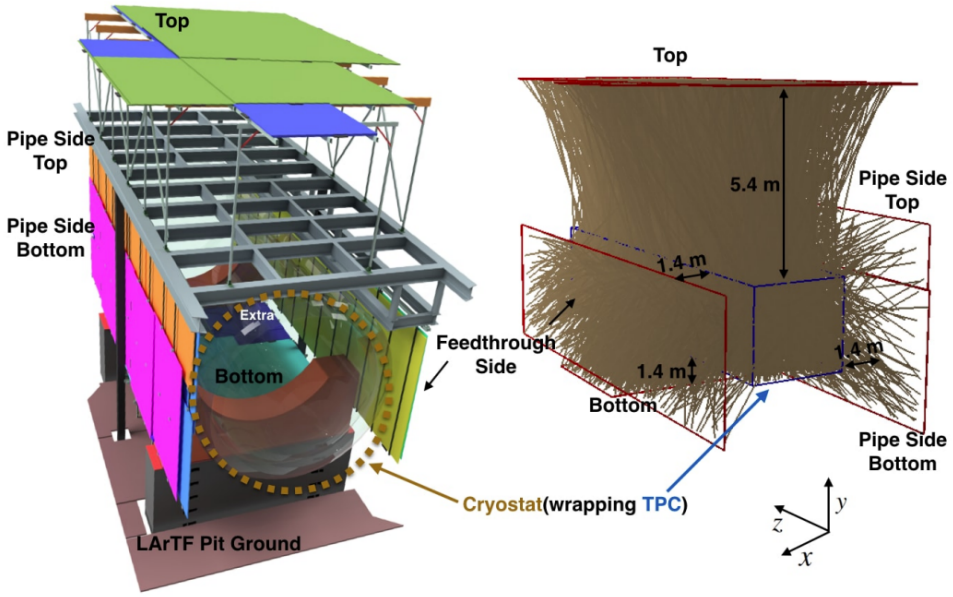

Figure 4.13: (left) Scheme of the CRT system installed in the MicroBooNE detector. (right) Simulation of cosmic rays crossing the CRT, where the lines represent possible cosmic ray tracks. Figure from [69].

increase of outgoing muons from ν_μ interactions. The NuMI beam has a longer time window in comparison to the BNB beam because of how the neutrino beam is made in each case. Whilst BNB only makes use of the Booster Synchrotron, NuMI also uses the Main Injector, which is a much longer synchrotron, as shown in Figure 5.1. The Main Injector has a proton storage capacity seven times larger than the Booster, and it accelerates six Booster batches. Each Booster batch is 1.6 μs long.

4.4 Detector Performance Over the Run Period

It was observed that the detector performance was not entirely stable during its running period. This section describes two of the main changes: the decrease in the light response, and the observation of dead-wire regions.

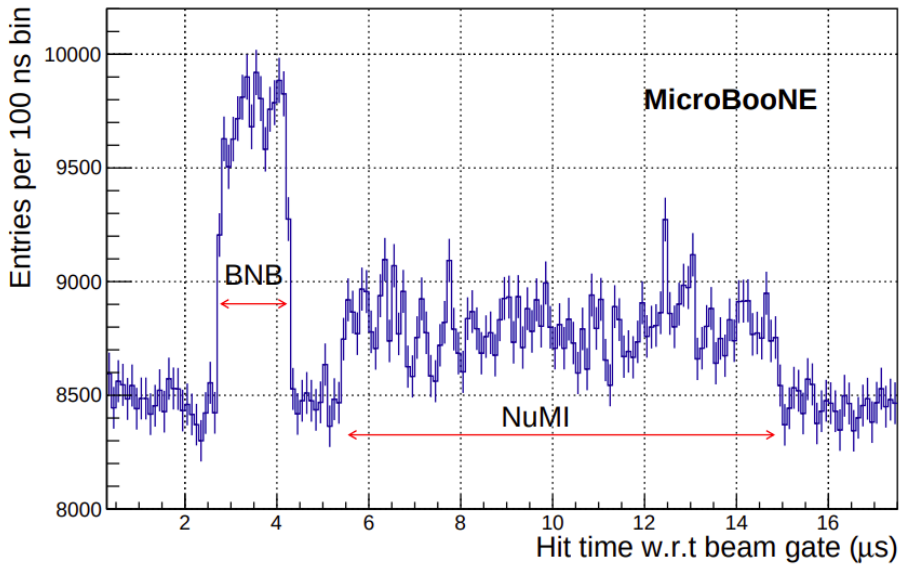

Figure 4.14: Number of events seen by the CRT system. The increase from $\sim 2.5\,\mu$s to $\sim 4.1\,\mu$s is related to BNB-induced events, and the increase from $\sim 5\,\mu$s to $\sim 15\,\mu$s is related to NuMI-induced events, as indicated on the plot. Figure from [69].

4.4.1 Light Response

The performance of the light detection system depends on factors such as the amount of impurities in the argon, as it affects the amount of produced scintillation light, the ageing of the PMTs, and/or degradation of the TPB. Understanding the effect of those factors on the scintillation light is crucial for a more precise interpretation of the collected data over time. A time-dependent calibration [70] was developed using samples of cosmic-induced muon tracks that cross the anode, known as Anode-Piercing Track (APT), or the cathode, known as Cathode-Piercing Track (CPT), of the detector.

The number of photons observed across all PMTs divided by the length of the muon track was observed throughout the working period of the detector, from October 2015 to March 2020. The number of photons observed is highly dependent on the location of the muon track in the detector. For instance, the same muon track will result in much more observed light if it happens closer to the anode, where the PMTs are installed, than if it happens closer to the cathode. For this reason, this calibration focused on the relative change in the observed number of photons rather than the absolute number for APT and CPT events. The percentage change

is displayed on Figure 4.15.

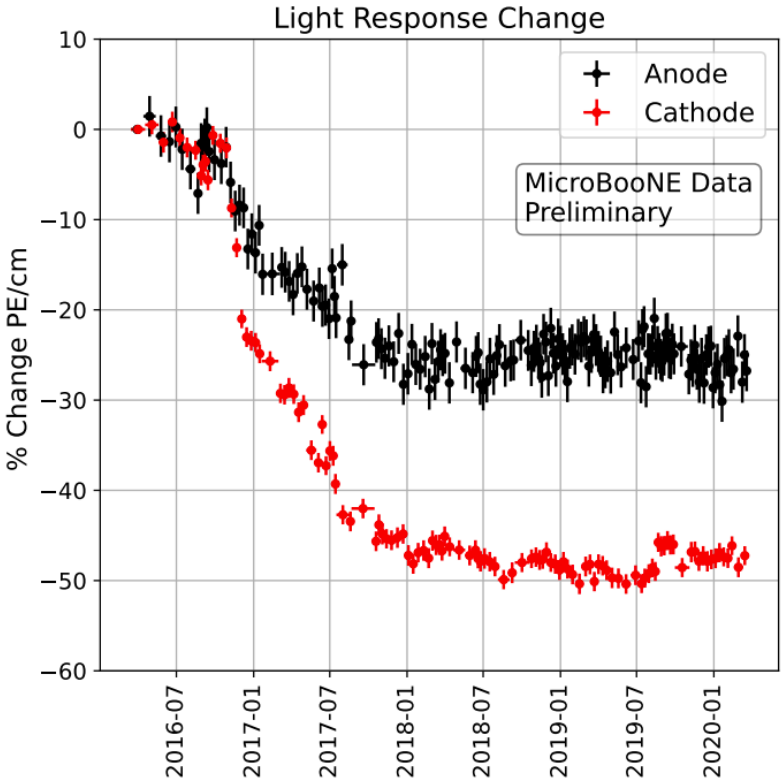

Figure 4.15: Percentage change in the observed light over time for the APT (black) and CPT (red) events. Figure from [70].

A possible cause of the decrease in the amount of observed light is the introduction of impurities in the detector in September 2016. Those impurities would increase the amount of effects such as absorption and quenching, whilst not affecting the ionisation charge, since no change in the latest was observed in the same time period. However the real cause of the observed decrease in the amount of observed light is still unknown.

In order to soften the abrupt change shown in Figure 4.15, a time-dependent calibration was developed as being the midpoint between APT and CPT measurements with an uncertainty corresponding to half of the distance between them.

4.4.2 Unresponsive Wires

Around 10% of the wires used on the charge sensitive planes in MicroBooNE are unresponsive. The reason for this behaviour is not fully understood. A possible cause would be wires from a plane physically touching wires from a different plane, even though a visual inspection (prior to filling the cryostat with liquid argon) did not find any wire physically touching another. The faulty wires are identified and this information is used during the reconstruction process.

Chapter 5

The NuMI Beam at MicroBooNE

Fermilab produces two main neutrino beams used by most of the neutrino experiments onsite: the Booster Neutrino Beam (BNB) and the Neutrino at the Main Injector (NuMI) beam [71]. The MicroBooNE detector is located on-axis to the BNB beam and off-axis to the NuMI beam. The analysis presented in this thesis uses only NuMI data, and for this reason this chapter will focus on this beam.

5.1 Neutrino Beam Production

The NuMI beam production starts by accelerating protons in three stages: first the protons are accelerated up to 400 MeV in a Linear Accelerator (LINAC), then up to 8 GeV in the Booster Synchrotron, and then up to 120 GeV in the Main Injector, as shown in Figure 5.1. The accelerated protons then collide with a graphite target creating a cascade of particles, mostly dominated by pions and kaons. The produced charged particles are collimated by two two large and intense magnetic horns, Figure 5.2, which have two polarities. In the Forward Horn Current (FHC) polarity, +200 kA, positive particles such as π^+ and K^+ are focused, whilst the Reverse Horn Current (RHC) polarity focuses π^- and K^- under a -200 kA current. The focused charged particles (such as $\pi^\pm$ and $K^\pm$) travel 675 m down the Decay Pipe where they decay to neutrinos (for instance $\pi^\pm \rightarrow \mu^\pm + \nu_\mu(\bar{\nu}_\mu)$, a list of the other decays is provided on Section 5.2) which are boosted in the direction of the charged particles. An absorber made of aluminium, steel and concrete is placed at

the end of the Decay Pipe and stops those particles that have not decayed. All the existing particles at the end of this process end up surrounded by the natural rock of the ground that acts as a "muon-shield". As a result, the non-neutrino particles are stopped and a neutrino beam is formed along the beamline direction. The number of Protons on Target (POT) at the beginning of this chain is used as a measure of the amount of neutrino flux.

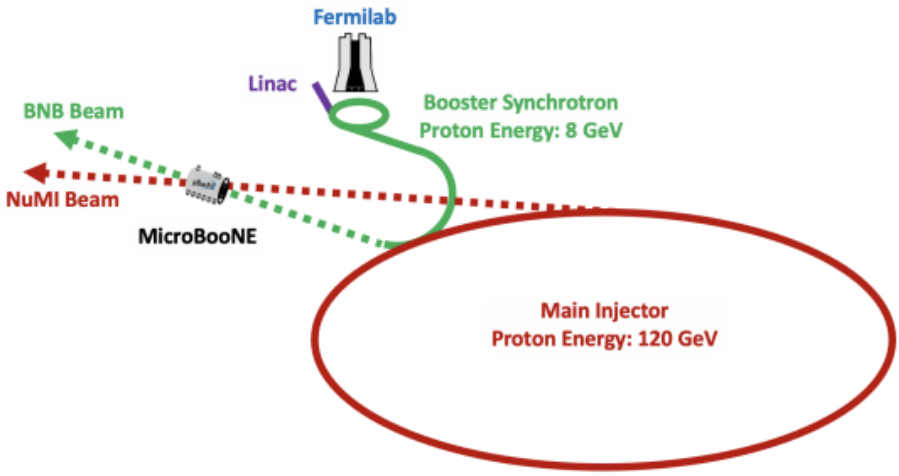

Figure 5.1: Diagram illustrating the production of the BNB and NuMI beams production at Fermilab. Figure from [63].

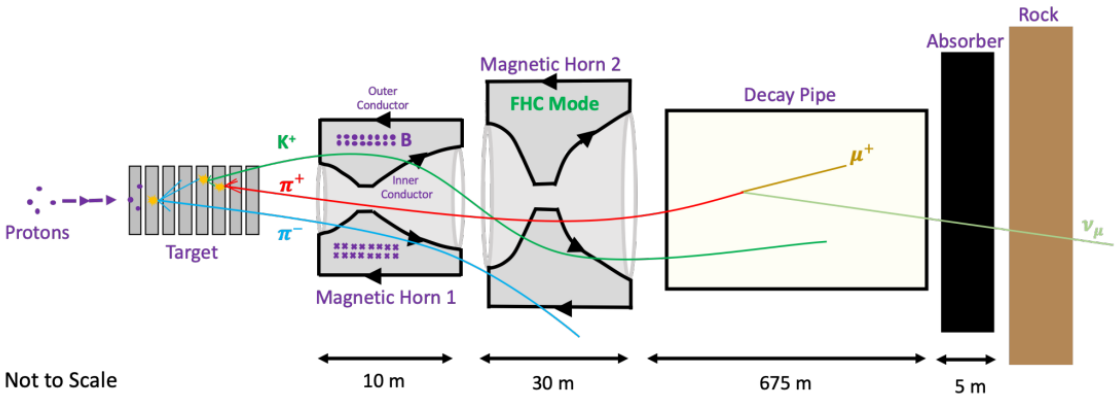

Figure 5.2: A diagram of the NuMI neutrino beamline. The change between the FHC and RHC polarities is achieved by inverting the polarity of the magnetic horns. Figure from [63].

5.2 Neutrino and Antineutrino Modes

The neutrino beam is formed by the decay of the produced $\pi^{\pm}$ and $K^{\pm}$ particles. The main decay channels can be summarised as

$$\text{FHC: } \pi^{+} \rightarrow \mu^{+} + \nu_{\mu} \text{ and } K^{+} \rightarrow \mu^{+} + \nu_{\mu} \tag{5.1}$$

$$\text{RHC: } \pi^{-} \rightarrow \mu^{-} + \bar{\nu}_{\mu} \text{ and } K^{-} \rightarrow \mu^{-} + \bar{\nu}_{\mu} \tag{5.2}$$

for this reason FHC(RHC) is also known as "neutrino(antineutrino) mode". In reality other decays happen simultaneously to the processes described by Equations 5.1 and 5.2 that populate the produced beam with ν_e and $\bar{\nu}_e$. These decays are subdominant electronic decay modes of $K^{\pm}$ hadrons, decays of K^0 particles, and decays of tertiary muons [71, 72], the relevant decay modes are shown in Table 5.1. The smaller branching ratio for the electron-neutrino decays is caused by the helicity suppression[1] similarly to the effect explained in Section 3.2. The breakdown of the NuMI flux per neutrino flavour is shown in Figure 5.4 as a function of the mother particle and the Feynman diagram of these decays is shown in Figure 5.3.

The NuMI beam was on during the full MicroBooNE running period, and explored different beam modes, as shown in Table 5.2. The cumulative POT delivered by the NuMI beam during the working period of the MicroBooNE detector is shown in Figure 5.5. This thesis uses the FHC Run 1 data collected by MicroBooNE.

5.3 Advantages of Using the NuMI Beam

The number of produced kaons and pions from the proton-target collision at the beginning of the beamline chain depends on the incident proton energy. More energetic accelerated protons (like in the NuMI beam, $E_p \sim 120\,\text{GeV}$) will generate more daughter-kaons in comparison to less energetic ones (like in the BNB beam,

[1] Pion has spin zero, therefore the produced particles from a pion decay must also result in a system whose overall spin is zero. In a relativistic approximation, the π^{+} decay $\pi^{+} \rightarrow \mu^{+} + \nu_{\mu}$, creates a LH ν_{μ} and a RH μ^{+}, resulting in spin-1 system in the centre-of-mass reference frame. However spin should be conserved, and it is only possible if the outgoing μ^{+} is LH, which is possible if the particle is slow enough to have a RH component. The same argument is valid for the decay $\pi^{+} \rightarrow e^{+} + \nu_{e}$, however it is much less likely for a e^{+} to have a RH component when compared to μ^{+} because e^{+} is much lighter. For this reason the branching ratio for this decay is more favourable in the muon channel.

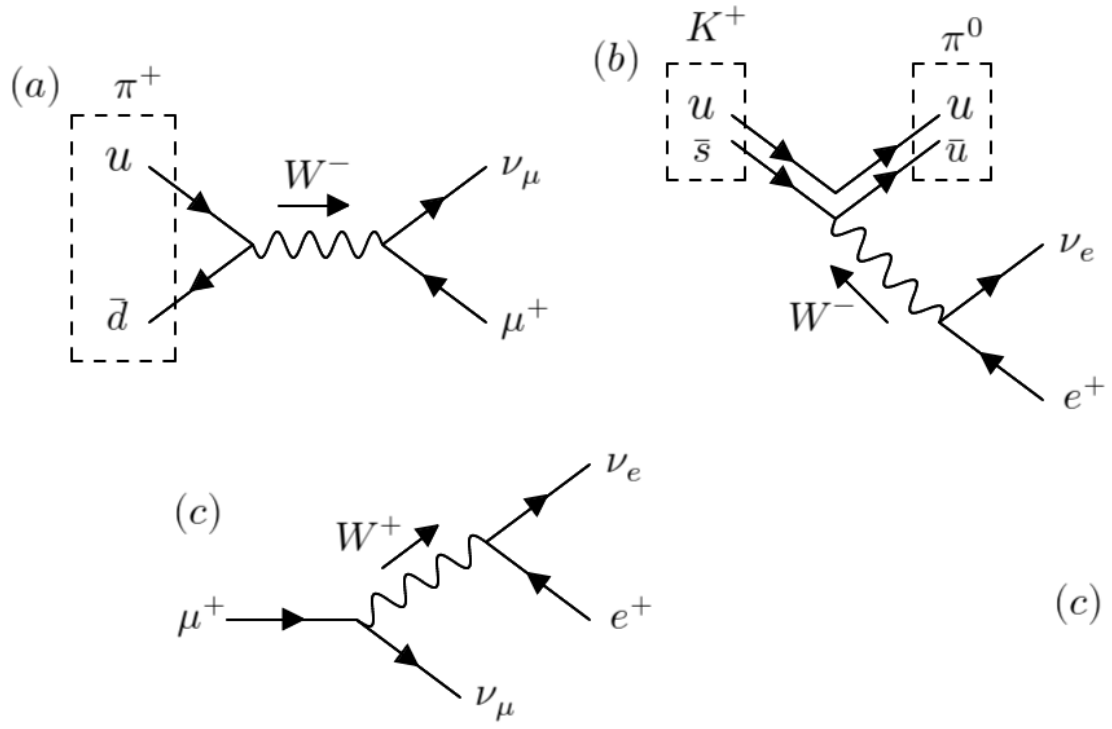

Figure 5.3: Feynman diagram of the decays in Table 5.1. (a) Feynman diagram for decays $\pi^\pm \to \mu^\pm + \nu_\mu(\bar{\nu}_\mu)$, $\pi^\pm \to e^\pm + \nu_e(\bar{\nu}_e)$ and $K^\pm \to \mu^\pm + \nu_\mu(\bar{\nu}_\mu)$, where $\pi^+ = u\bar{d}$, $\pi^- = \bar{u}d$, $K^+ = u\bar{s}$ and $K^- = \bar{u}s$. (b) Feynman diagram for decays $K^\pm \to \pi^0 + e^\pm + \nu_e(\bar{\nu}_e)$, $K^\pm \to \pi^0 + \mu^\pm + \nu_\mu(\bar{\nu}_\mu)$, $K^0_L \to \pi^\mp + e^\pm + \nu_e(\bar{\nu}_e)$ and $K^0_L \to \pi^\mp + \mu^\pm + \nu_\mu(\bar{\nu}_\mu)$, where $K^0_L = (1/\sqrt{2})(d\bar{s} + s\bar{d})$. (c) Feynman diagram for decay $\mu^\pm \to +e^\pm + \nu_e(\bar{\nu}_e) + \nu_\mu(\bar{\nu}_\mu)$.

Decay modes	Branching Ratio (%)
$\pi^{\pm} \rightarrow \mu^{\pm} + \nu_{\mu}(\bar{\nu}_{\mu})$	99.9877
$\pi^{\pm} \rightarrow e^{\pm} + \nu_{e}(\bar{\nu}_{e})$	0.0123
$K^{\pm} \rightarrow \mu^{\pm} + \nu_{\mu}(\bar{\nu}_{\mu})$	63.55
$K^{\pm} \rightarrow \pi^{0} + e^{\pm} + \nu_{e}(\bar{\nu}_{e})$	5.07
$K^{\pm} \rightarrow \pi^{0} + \mu^{\pm} + \nu_{\mu}(\bar{\nu}_{\mu})$	3.353
$K^{0}_{L} \rightarrow \pi^{\mp} + e^{\pm} + \nu_{e}(\bar{\nu}_{e})$	40.55
$K^{0}_{L} \rightarrow \pi^{\mp} + \mu^{\pm} + \nu_{\mu}(\bar{\nu}_{\mu})$	27.04
$\mu^{\pm} \rightarrow +e^{\pm} + \nu_{e}(\bar{\nu}_{e}) + \nu_{\mu}(\bar{\nu}_{\mu})$	100.0

Table 5.1: Relevant decay modes and their branching ratios for the production of the NuMI beam neutrinos (antineutrinos) [72].

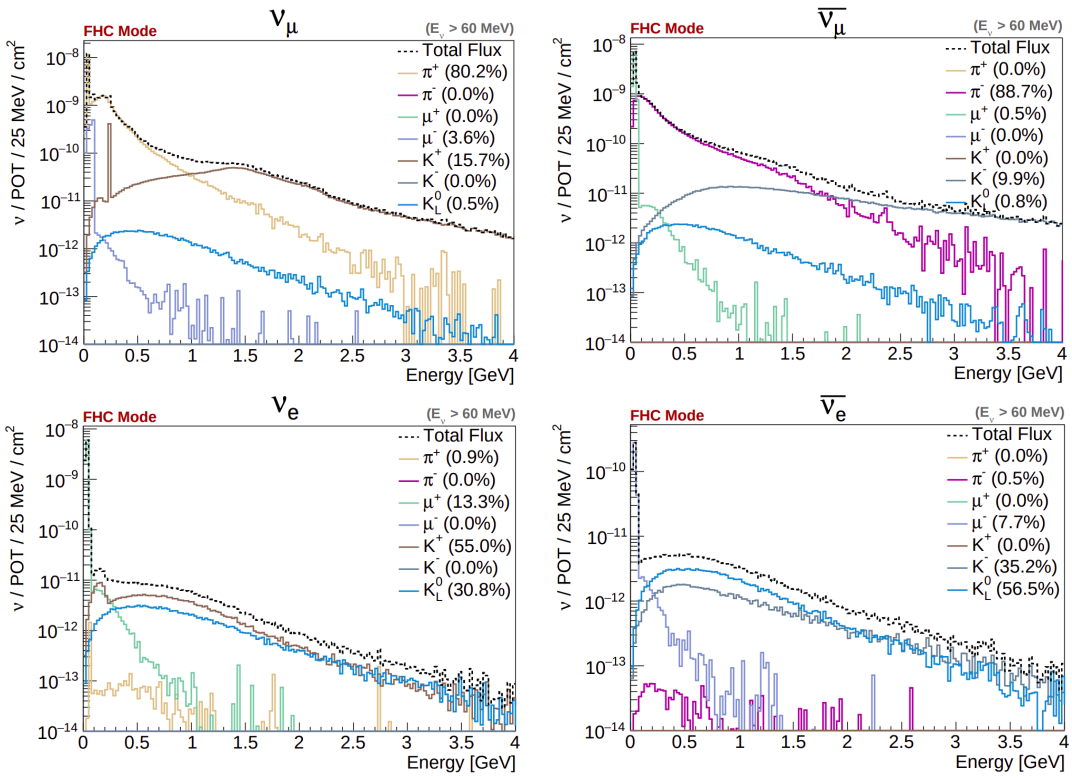

Figure 5.4: NuMI neutrino flux as a function of the mother particle. The percentages consider a neutrino energy threshold of 60 MeV to remove the large contribution from the muon decay for low neutrino energies. Figure from [63].

Run Number	Neutrino Mode	Period
Run 1	FHC	23 October 2015 - 2 May 2016
	RHC	29 June 2016 - 29 July 2016
Run 2	RHC	11 November 2016 - 14 November 2016
	FHC	14 November 2016 - 20 February 2017
	RHC	20 February 2017 - 7 July 2017
Run 3	RHC	7 November 2017 - 6 July 2018
Run 4	RHC	20 October 2018 - 26 February 2019
	FHC	26 February 2019 - 6 July 2019
Run 5	FHC	29 October 2019 - 20 March 2020

Table 5.2: NuMI neutrino modes during MicroBooNE working period.

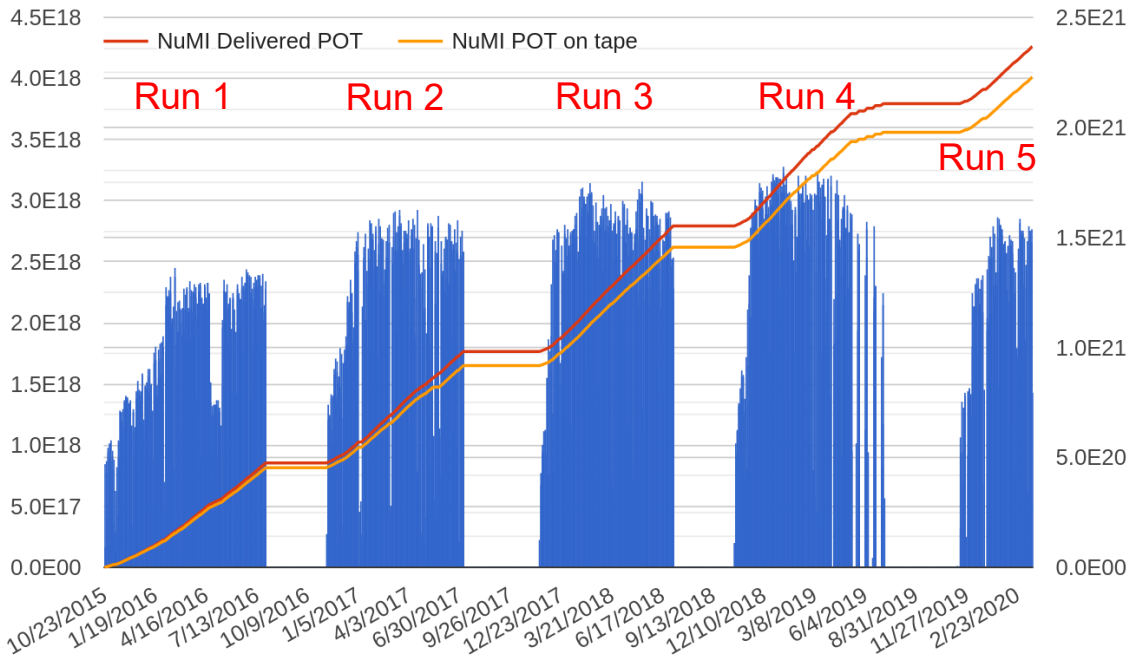

Figure 5.5: Cumulative POT delivered by the NuMI beam throughout MicroBooNE's working period, from Run 1 to Run 5. Figure adapted from [73].

$E_p \sim 8\,\text{GeV}$). As a consequence such a neutrino beam would have a larger population of ν_e and $\bar{\nu}_e$ because, as shown in the previous section, the kaon decay ($m_K = 490\,\text{MeV}$) is responsible for increasing the ν_e and $\bar{\nu}_e$ population in the final neutrino beam.

The neutrino beamline schematised in Figure 5.2 and the decay modes in Table 5.1 show that the ν_μ and $\bar{\nu}_\mu$ portion of the neutrino beam is mostly a result of the decay of the particles focused by the magnetic horns. Whilst the ν_e and $\bar{\nu}_e$ portion of the produced neutrino beam is a result of the decay of heavy particles that decay before passing the magnetic horns, and the decay of focused charged muons. As a result, the more off-axis the detector is, the greater fraction of $\nu_e/\bar{\nu}_e$ in comparison to $\nu_\mu/\bar{\nu}_\mu$. It is common to refer to this effect as off-axis enhancement of the $\nu_e/\bar{\nu}_e$.

The MicroBooNE detector is off-axis to the NuMI beam in both horizontal ($\sim 5^o$) and vertical ($\sim 6^o$ from the target location) directions, as shown in Figure 5.6.

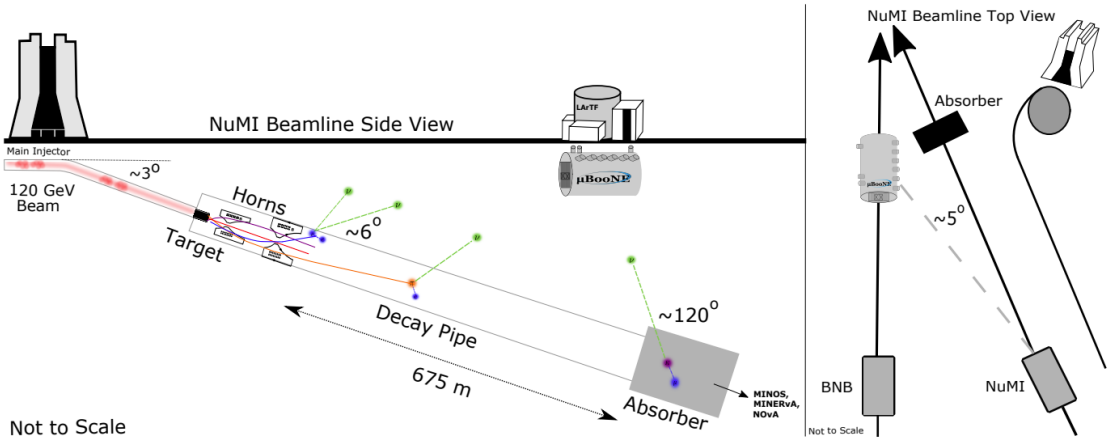

Figure 5.6: Relative position of the MicroBooNE detector with respect to the NuMI beam. Figure from [63].

Finally, the NuMI beam has a large cumulative POT throughout the 5 runs of functioning: 1.0×10^{21} POT for the neutrino mode (FHC), and 1.3×10^{21} POT for the antineutrino mode (RHC), offering large statistics for the analysis.

5.4 Readout and Trigger Systems

Using data from the NuMI beam requires understanding the readout and trigger systems of this neutrino beam.

The MicroBooNE detector is located on the surface and for this reason it is exposed to a large cosmic-ray contamination all the time. Therefore it is crucial to develop an efficient trigger system to efficiently save the events with a neutrino

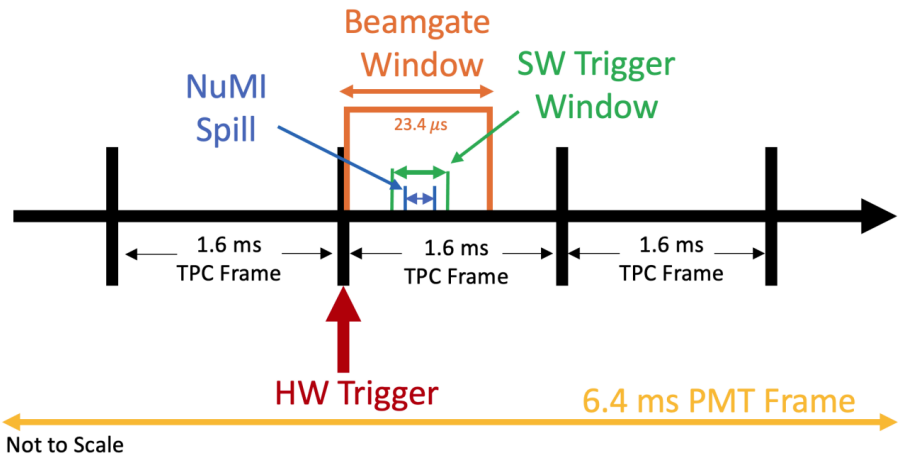

Figure 5.7: Scheme of the MicroBooNE readout and trigger systems. Figure from Ref. [63].

interaction in the detector without acquiring a huge amount of background. The readout process starts when Fermilab's Accelerator Division sends a signal when a new batch of protons collides on the NuMI target (known as a "spill"). This signal is known as the Hardware (HW) trigger. The HW trigger defines the beginning of the 23.4 μs wide unbiased readout (no light intensity requirements), known as the beamgate window, in which all the information is stored at the first stage. The neutrinos produced during the HW-trigger spill are expected to arrive at the detector within 5.64 μs and 15.44 μs after the start of the beamgate window. This interval is known as "NuMI beam spill time window".

The complete MicroBooNE readout cycle takes a total of 4.8 ms, divided into 3 TPC readout frames, each of them being 1.6 ms long, as shown in Figure 5.7. This first stage of data collection is determined by the presence of a HW trigger to increase the chances of witnessing a beam event.

Only 2-3% of the spills from the NuMI beam will generate a neutrino interaction in the detector, so using the HW trigger by itself will result in many events without neutrino interactions. For this reason, it is important to determine which HW-triggers will permanently be saved, and which will be rejected. This is done via a Software (SW) trigger that requires a minimum of 9.5 Photo-Electrons (PE) of scintillation light in a time window of 4.69 μs to 16.41 μs after the HW trigger. The events passing the SW trigger are saved and used for analysis.

It is possible that a few cosmic interactions will pass both the HW and SW

triggers. A special set of data, known as "external", is produced to understand those interactions. The external data is made of events that pass the light trigger threshold when there is no beam, to ensure no beam-induced interactions are preserved in the sample. In addition, a few external events that do not pass the SW trigger are also recorded, and comprise a set of cosmic events without timing and light intensity requirements. This last set of data is known as "external unbiased".

Chapter 6

Simulation and Reconstruction in MicroBooNE

In the process of performing a physics analysis, the MicroBooNE experiment employs a set of simulation samples. The simulation provides information about the particle that is being simulated as well as the effects of the reconstruction of its neutrinos in the detector. Therefore it allows us to understand how well the reconstruction is functioning and explain failure modes. The simulation and reconstruction processing is a complex chain that will be explained in this chapter together with the samples used.

6.1 Simulation Overview

The process of simulation has several stages. It starts with the beam simulation, responsible for generating a distribution of neutrino flavours and momenta to mimic the NuMI beam composition at MicroBooNE. The information of those neutrinos, such as direction and energy, is then used to simulate neutrino interactions within the detector. The daughter particles originating from the interactions are then propagated in the detector and their energy deposition and trajectory are simulated and saved. The light and charge signals generated by the charged particles are propagated to the detection systems. The final stage is to reconstruct the detected signal and make it ready and available for data analysis. In this thesis simulation samples

are often referred to as Monte Carlo (MC).

6.1.1 The NuMI Beam Simulation

The first step in the simulation chain is to simulate the neutrinos in the beamline. The NuMI beam has been used by many other experiments at Fermilab, such as NOνA [26], Main Injector Neutrino ExpeRiment to study ν-A interactions (MINERνA) [74], and MINOS [24]. Therefore the NuMI beam flux simulation software has been continuously improved and developed for many years. To mimic the actual neutrino beam described in Chapter 4, the software simulates the proton-target collision and its products. The physics models used in this simulation are described by a Geant4-based package [75] called *g4numi*. This package is also used to describe the beamline geometry, meaning the shape and material of the objects in the beamline, such as the target and the horns. The final outputs of this simulation are called *dk2nu* files. These are ntuple-like files with information about the produced neutrinos and their ancestry, such as their full kinematics. Information about the neutrino parent particle is used later on to implement hadron production constraints in the neutrino flux simulation. The *dk2nu* files contain all the information required to calculate the neutrino flux for a specific detector location and size.

Flux Prediction

The Package to Predict the FluX (PPFX) [76], developed by L. Aliaga Soplin, is used in the NuMI simulation to constrain the hadron production modelling and to propagate uncertainties for the NuMI beamline simulation. This package was originally developed for the MINERνA experiment and has been used by other experiments using the NuMI beamline such as MicroBooNE, NOνA and MINOS+. This package uses information of the neutrino parentage from the *dk2nu* to apply constraints to the flux prediction. These constraints use a correction weight to each decay used in the generation of the flux prediction. The final weighed flux is known as "Central Value (CV) flux prediction", and its distribution for the NuMI beam at MicroBooNE is shown in Figure 6.1 for both FHC and RHC configurations.

As explained in Section 5.1, the neutrino beam production starts by colliding accelerated protons on a target. The PPFX package can simulate this process using

two different assumptions: thick and thin targets. The predictions from both sets were compared to the flux calculated using an *in situ* method from the study of neutrino interactions by the MINERνA experiment. The thin target assumption resulted in a better agreement to data, and has been the one used by the MicroBooNE experiment.

The corrections applied by the PPFX package can be split into a few categories: attenuation and absorption, extending data coverage, extrapolation in areas with no applicable data.

Attenuation and absorption corrections

This correction takes into account the particle interactions with the beamline components such as the target, beam monitors, horns, decay pipe volume and decay pipe walls. These interactions can decrease and/or modify the original flux depending on the cross section and the amount of material traversed by the particles. A "survival" correction is then calculated based on the probability of the traversing particle to interact with the material. This correction is not applied to neutrinos, mostly to hadrons.

Extending data coverage

This correction accounts for uncertainties on the target material. It is motivated by the fact that the available experimental data on hadron production from proton-target collisions, like the ones used in the production of neutrino beams, are not extensive. For this reason, it is often necessary to group the available data as a function of the target material (commonly expressed as function of its mass number) and/or as a function of the incident proton energy, to make it possible to extrapolate it to other materials and energies.

The first part of this correction is called "material scaling". It is related to the uncertainty associated with using hadron production data taken on carbon in other materials, different than the one in the NuMI beamline target. This extrapolation is done under the assumption that the ratio of the invariant cross section calculated using two different materials depends on the ratio between their mass numbers and on a variable $\sigma(x_F, p_T)$. The extraction of the $\sigma(x_F, p_T)$ factor[1] was done by fitting

[1]The variables x_F and p_T are called "Feynman-x" ([77, 78]) and transverse momentum, respectively.

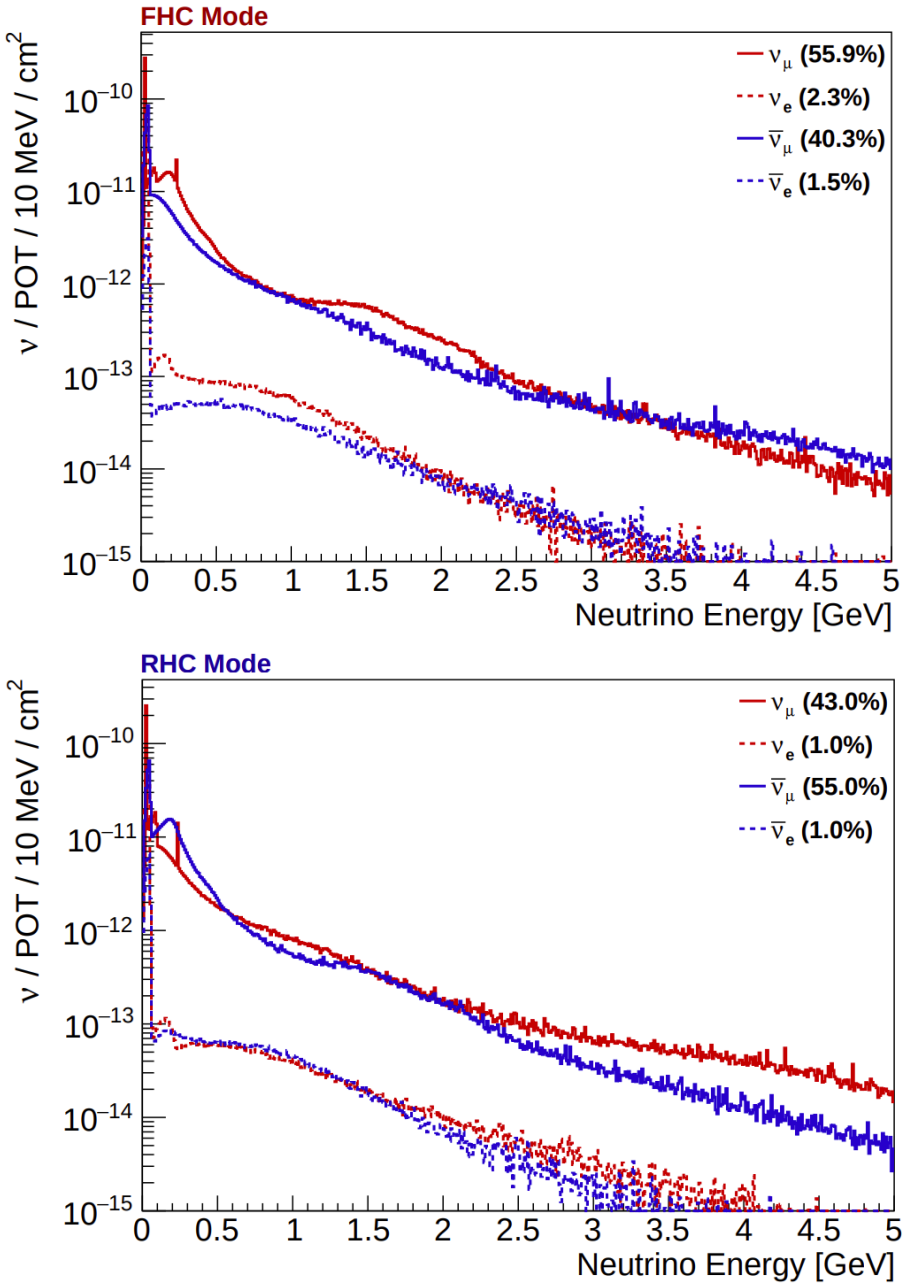

Figure 6.1: The NuMI beam central value prediction for MicroBooNE in both FHC (left) and RHC (right) configurations. The integrated proportions of the flux are shown in the legend. Figure from [63].

the Skubic data [79] that consist of invariant cross sections of K^0, Λ^0 and $\bar{\Lambda}^0$ produced from proton interacting in various nuclei at 300 GeV.

The second part of this correction comes from the isoscalar nature of ^{12}C (the main material of the NuMI target) to infer $\sigma(pC \rightarrow \pi^{\pm}X) = \sigma(nC \rightarrow \pi^{\mp}X)$, where pC and nC represent the proton-carbon and neutron-carbon interactions. The reason for that is that ^{12}C has 6 neutrons and 6 protons, and a symmetry between proton-neutron (isospin symmetry) was used. These neutrons come from the primary proton-target collision, and they can interact inelastically in the target and produce charged mesons that will decay to neutrinos. No additional uncertainty is added when using this extension.

Finally, the third part of this correction assumes isospin symmetry in a quark-parton model [80] to determine the number of neutral kaons, $N(K^0_{L(S)})$, using the number of $K^{\pm}$, $N(K^+)$ and $N(K^-)$, via the Gatignon-Wachsmuth equation

$$N(K^0_{L(S)}) = \frac{N(K^+) + 3N(K^-)}{4}. \tag{6.1}$$

It is important to include neutral kaons in the flux prediction because they can decay into pion, that can then decay into neutrinos. This estimate of the number of neutral kaons was necessary because there was no data for neutral kaon.

Extrapolation in areas with no applicable data

Another uncertainty involves areas with little data coverage, for instance high-energy mesons in the range of $10 - 40$ GeV traversing the beamline. In this case, it is assumed that the level of agreement between the simulation and existing hadron production datasets can be extrapolated to uncovered regions [76].

6.1.2 Neutrino Generation

The next step in the simulation chain is to simulate the neutrino interactions within and surrounding the detector. This is done using the GENIE v3.0.6 neutrino event generator [81]. GENIE is a software package specialised in neutrino-nucleus interactions. It provides information about the interaction type and the daughter particle properties. The list below describes the physical models used by GENIE v3.0.6 to simulate the neutrino interactions described in Chapter 2:

- **QE Model** is simulated using the Nieves model [82] with Random Phase Approximation (RPA) and Coulomb corrections [83] for the outgoing lepton [84]. This model accounts for multi-nucleon-mechanism effects to reconstruct a neutrino energy in quasielastic-like events in a way that improves agreement with data. A realistic simulation for interactions on argon includes the fact that outgoing leptons in CC interactions can undergo multi interactions before leaving the nucleus, also known as "final state interactions", once that the free-nucleon approximation does not apply to argon. RPA accounts for the effect of these multi-interactions on the effective electroweak coupling, whilst the Coulomb correction accounts for the change in the momentum of the outgoing lepton.

- **QE Vector and Axial Form Factors** describe the charge distribution of the nucleus. MicroBooNE uses a different parametrisation for each case. The vector form factor is simulated with the BBBA05 Parametrisation [85], that accounts for the nucleon form factors for non point-like nucleons. The axial form factor is simulated using the dipole [86] model, that assumes an axial form factor of quasielastic-like events described as a dipole.

- **RES Model** is simulated using the KLN [87] and Berger-Sehgal [88, 89] models. These two models accounts for modelling resonant scattering using two groups of information. The KLN model contributes with the outgoing lepton mass and spin for single pion production. And the Berger-Sehgal model contributes with information about the resonant pion production process.

- **Coherent (COH) Model** is simulated using the Berger-Sehgal model [90], that describes the coherent pion production. According to this model, the cross section for CC pion production is defined as an equation that depends on the modulus of the four-momentum transfer between the incoming virtual boson and the outgoing pion, the four-momentum transfer between the incident neutrino and the resulting lepton and the pion decay constant.

- **DIS Model** is simulated using the Bodek-Yang [91, 92] model. Deep inelastic scatterings happen for high-energy neutrinos that interact directly with the internal structure of the nucleon, the quark. The quark distribution in protons and neutrons is parametrised by parton distribution functions Parton Distribution Funtions (PDF). The Bodek-Yang model suggests modifications to GRV94 leading order PDFs [93] so it can be used to model electron, muon and neutrino DIS cross sections.

- **Nuclear Model:** Local Fermi Gas (LFG) [94] with constant binding energy correction. The LFG model calculates the potential as a function of the local nuclear density, $\rho(r)$, which, in turn, depends on the radial position of the nucleon within the nucleus, r.

- **MEC Model** is described by the Nieves [95] model, which describes the MEC reactions based on kinematic information such as the energy and momentum transfer from the lepton to the nucleus.

- **FSI Model** is described by the IntraNuclear Cascade (INC) hA2018 [96] model. This model was developed using pion cross-section measurements.

It was noted that the combination of these empirical submodels cannot reproduce the collected MicroBooNE data, and a discrepancy between MC and MicroBooNE data was observed [97]. A possible reason was a GENIE v3.0.6 mis-modelling of CCQE and MEC interactions. MicroBooNE has developed a GENIE tune (μB tune) that reweights the CCQE and MEC interactions based on T2K cross-section data [98]. T2K data was chosen for this procedure as the dataset is as close as possible to the MicroBooNE one, and contains large statistics of the interaction types of interest. The result of the μB tune on MicroBooNE is shown in Figure 6.2, where a comparison between the simulated neutrino interactions from the BNB beam with and without the μB tune is displayed. The tune works by increasing the normalisation of the simulation in a event-by-event basis, which results in decreasing the data/simulation ratio from 1.12 (untuned) to 1.01 (tuned).

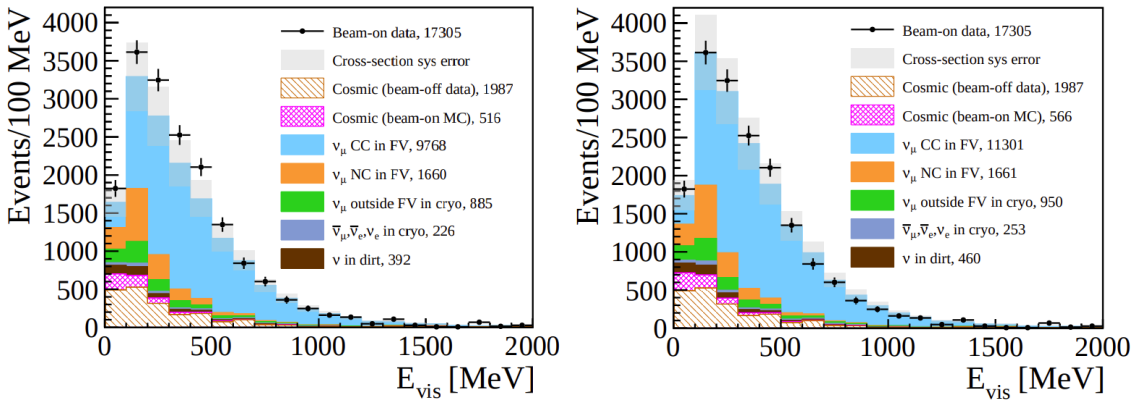

Figure 6.2: Simulated neutrino interactions predicted by GENIE v3.0.6 without (left) and with (right) the μB tune applied [97].

6.1.3 Cosmic Ray Modelling

Alongside the entering neutrinos from the beam, MicroBooNE is constantly exposed to a high rate of incoming cosmic rays from the atmosphere that also create signal inside the detector. Cosmic rays are created when particles coming from the universe interact with the particles from the atmosphere. These particles undergo many secondary interactions and, at sea-level, are made mostly of muons. In order to avoid simulating the cosmic rays individually, which demands large computational power, and to be as realistic as possible, MicroBooNE has developed an overlay technique [99]. This involves using cosmic ray data from the external unbiased trigger and overlaying the simulated neutrino interactions on top of them.

All the external unbiased events recorded during the operation period of MicroBooNE are saved. The overlay process can take place when the accumulated number of cosmic background events corresponds to the POT used to collect the beam-on data. For each beam-induced event created an external unbiased event is needed.

6.1.4 Propagation and Detector Simulation

Once the daughter particles are created from the neutrino interactions, the next step is to propagate those particles through the detector and understand the energy deposition. The particle propagation is done using GEANT4, and the physics list used is QGSP_BERT. This physics list uses three hadronic models to simulate charged pions, kaons and protons/neutrons: the Bertini Cascade model (BERT) [100] to simulate inelastic collisions of charged pions, kaons and nucleons at low energies ($< 10\,\text{GeV}$), the low energy parametrization model (LEP) [101] at intermediate energies and the quark gluon string model (QGS) [102] for high energies, responsible for simulating the de-excitation of the nucleus after high energy interactions. In this stage, GEANT4 provides the energy deposition per particle throughout their path inside the detector. With this information it is possible to extract the amount of charge and light produced at each point of the particle trajectory. In turn, the Liquid Argon Software (LArSoft) [103] is responsible for propagating the ionised charge and scintillation light in the detector.

The next step is to simulate the electronics and field response of the detector. The drifting ionisation electrons induce current on the wire planes that is parameterised

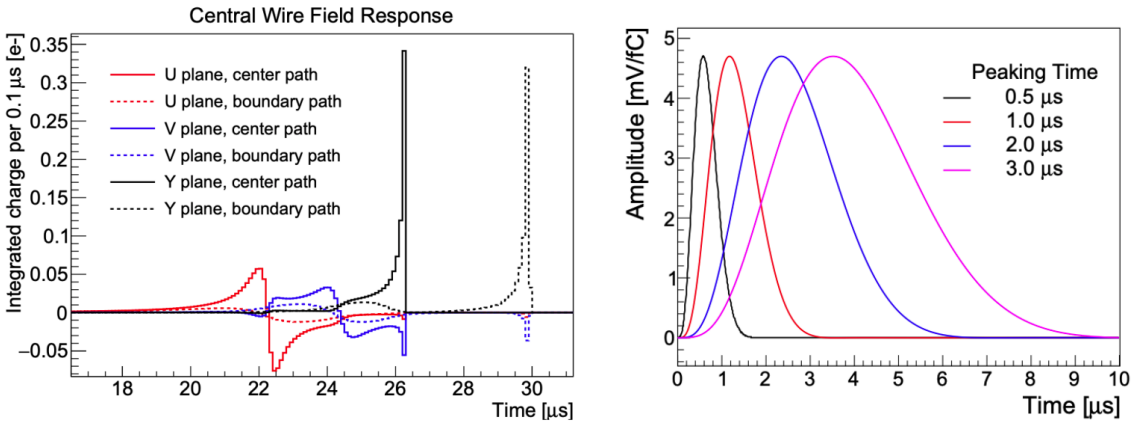

Figure 6.3: The field response for each wire plane (left) and the electronics response for different peaking time configurations (right). Figure from [104].

as a function of the drift time for different paths of ionisation electrons using the 2D Garfield program [104]. This process is described by the field response function.

The induced current on the wire is received, amplified, and shaped by a pre-amplifier. This process is performed by front-end cold electronics ASICs (placed inside the cryostat) and described by the electronics response function. These electronics can be configured to have four different gain settings (4.7 mV/fC, 7.8 mV/fC, 14 mV/fC and 25 mV/fC) and four peaking time settings (0.5 μs, 1.0 μs, 2.0 μs and 3.0 μs). The peaking time is defined as the time difference between 5% of the peak at the rising edge and the peak. MicroBooNE uses a gain of 14 mV/fC and a peaking time of 2 μs. Figure 6.3 shows the field response for each wire plane and the electronics response for different peaking time configurations.

At this point of the simulation chain, the simulated events have the same format as the collected data.

6.2 Signal Reconstruction

6.2.1 TPC Charge Reconstruction

The analysis in this thesis uses the WireCell software package [66, 105] to perform reconstruction of the MicroBooNE data. This technique uses time and geometry

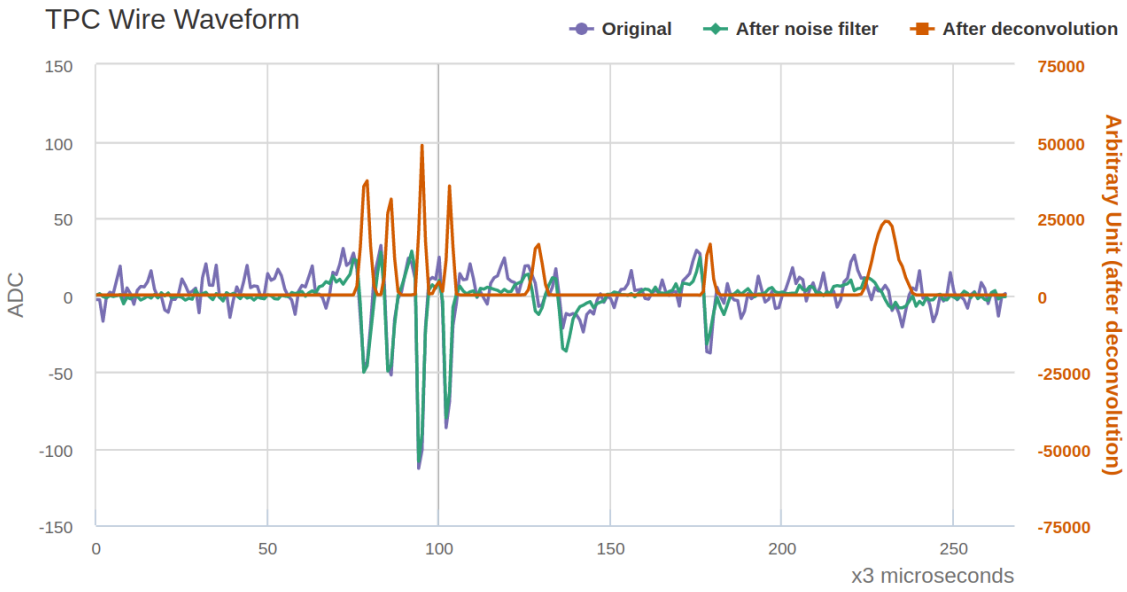

Figure 6.4: Representation of the filtering effects in the collected waveform (purple), after applying a noise filter (green), and deconvolution (orange). Figure from [108].

information to reconstruct 3D images in a tomographic way. The first step involves filtering techniques to reduce excess noise [106] and removing the induction response shape [107], to create a normalised pulse of charge for each wire [108], as shown in Figure 6.4.

This reconstruction technique relies on dividing the detector, and therefore the waveform, into $\sim 2\mu$s-thick time-slices and grouping the collected signal into *cells*. Two definitions are important in this process: a "wire" and a "cell". A *wire* is defined as a 2D region centred around the wire location with the width equal to the wire pitch. A *cell* is then defined as the overlapping region formed by the nearest wire from each plane, as shown in Figure 6.5.

The WireCell reconstruction technique relies on identifying which cells have been hit by electrons, so called "hit cell". Figure 6.6 exemplifies the ambiguity problem faced by the choice of splitting the region into hit cells. In this example, the displayed wires (19 hit wires in total, 8 hit U wires, 5 hit V wires and 6 hit Y wires) collected a signal, and the overlap region of those wires represent 55 possible hit cells, shown by the blue dots. The reconstruction tool then has to use the hit wires (known) information to establish the hit cells (unknown) information. However there is more unknown (55) than known (19) information, resulting in ambiguity. This ambiguity

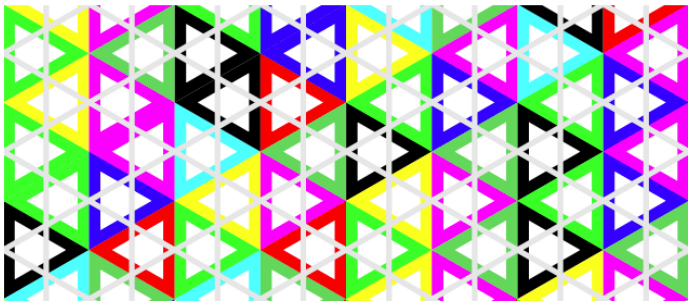

Figure 6.5: Cells constructed with the MicroBooNE detector geometry. Cell boundaries are represented by coloured lines, while the wire centres are represented by gray lines. All cells have equilateral triangular shapes due to the $\pm 60^o$ wire orientation [105].

is mitigated by a procedure called tiling, where the connected hit wires are merged as "wire bundles". The overlapping of wire bundles is called "blobs", as shown in Figure 6.6 by the blue contour, and is considered the geometric unit in the WireCell reconstructed 3D image. A "wire bundle" is a 2D form whilst a "blob" is in 3D as the combination of the wire planes. The advantage of using the tiling procedure is to completely collect the reconstructed charge smeared to the adjacent wires, to reduce the number of unknowns in the later stage of "solving", and to reduce the computational cost.

WireCell uses a 2-plane tiling, where "blobs" are formed by requiring the superposition of two wires at a time, instead of three. This is because about 10% of the wires in MicroBooNE are non functional, which causes the inactive region on the 2D anode plane to be about 30% in the 3-plane tiling approach, and 3% in the 2-plane one, as shown in Figure 6.7.

The next step is to relate the charge measured by the wires to the unknown true charges of the blobs under the assumption that the same amount of ionisation charge is seen by each wire plane. This process is done by constructing a system of equations $y = Ax$, where y is a vector of charge measurements spanning the hit wires from all planes, x is a vector of expected charge in each possible hit cell, and A is a matrix connecting wires and cells with 1 representing presence of a signal and 0 representing the absence of a signal. An example of this matrix is shown in Figure 6.8. However, as shown in Figure 6.6, this system has more unknowns (in this case the length of x is 55) than knowns (in this case the length of y is 19), which makes it unsolvable. To fix this situation, WireCell uses constraints based on characteristics of typical physics events [105] to remove the unknowns until it is a

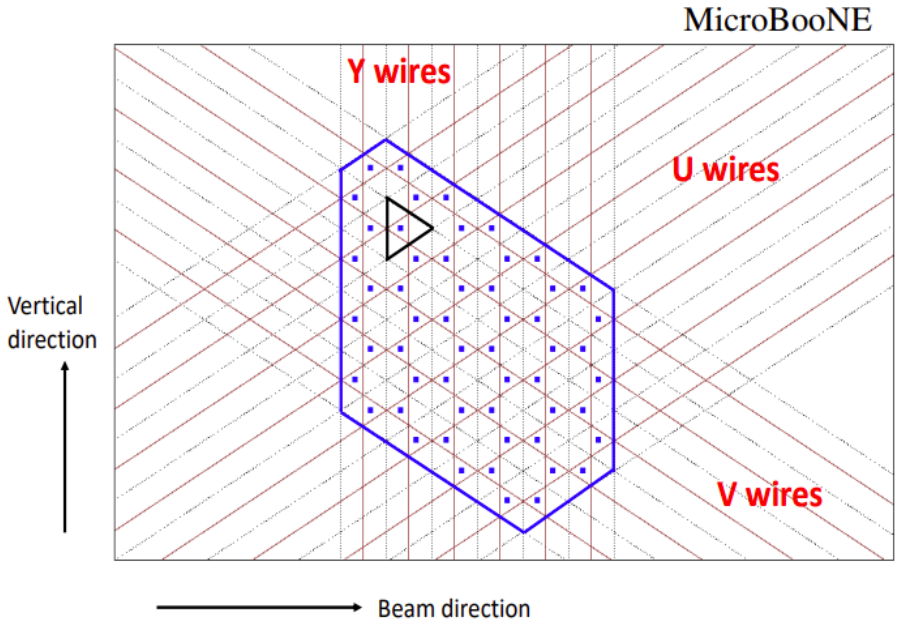

Figure 6.6: Diagram of the hit cells in the MicroBooNE detector and a "blob" constructed by the hit wires. The solid lines represent the wires, and the blue dots represent the hit cells. The "blob" is formed by the contiguous hit cells and marker by solid blue lines. Figure from [109].

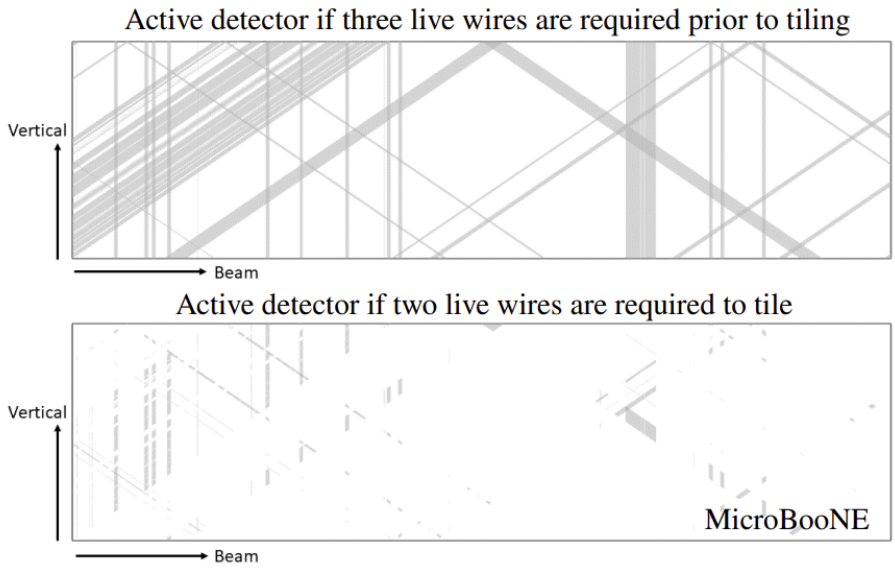

Figure 6.7: Diagram of the inactive regions on the 2D anode plane for the 3-plane tiling approach (top) and for the 2-plane tiling approach (bottom). Figure from [109].

solvable system of equations. One of the constraints, for instance, accounts for the fact that most of the elements in the solution x are "fake hits" and should be zero. This is done by using a minimisation function that minimises the number of non-zero entries of the system.

Finally, the charge deposited on each point of the 2D anode plane is established, a 3D image is formed by concatenating all the 2D cross-sectional images in the time dimension. The initial time of the interaction, t_0, is defined as the moment in which the scintillation light is detected by the PMTs. From this moment, it is possible to measure how much time the charge takes to arrive at the anode plane and measure the distance between the interaction point and the anode plane by considering their drift velocity.

6.2.2 PMT Light Reconstruction

The recorded signals from the PMTs are separated into two groups: the *beam discriminator* and the *cosmic discriminator*.

The beam discriminator is responsible for registering the beam-induced activity inside the detector. It is triggered by the neutrino beam and starts recording 4 μs

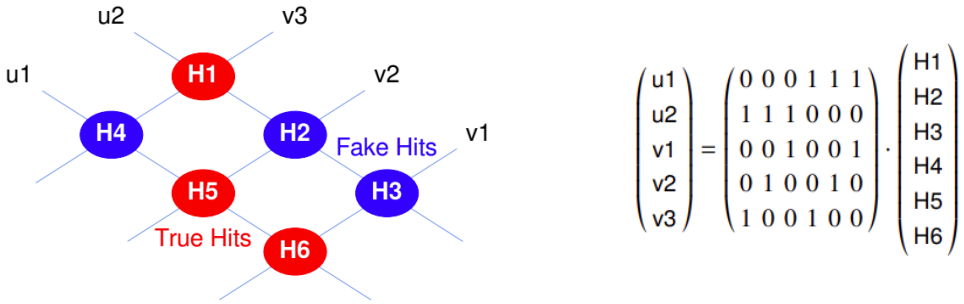

Figure 6.8: (left) Scheme of a 2-plane tiling approach where all u_1, u_2, v_1, v_2, v_3 wires registered signals coming from the true hits, in red. The blue hits represent fake hits given the registered signals. (right) Matrix representation of the diagram on the left. Figures from [105].

before the beamgate for a period of $\sim 23.4\,\mu$s. A "flash" is then formed by the group of waveforms recorded within a $7.3\,\mu$s window that satisfy the following requirements: at least 2 PMTs with a recorded signal above 1.5 PE (photo-electrons) and a total integrated PE above 6 PE in a 100 ns window. These requirements help rejecting "dark photons" created by the photomultipliers and radiological radiation in the detector. The starting time of a flash is defined as the moment where the PE sum of all PMTs is maximum.

The cosmic discriminator, on the other hand, is a self-triggered stream that records cosmic activity inside the detector during a period of $\sim 0.6\,\mu$s. This is a period shorter than the slow component of the scintillation light, see Section 4.1.2, which means that not all of the waveform is recorded. However, since cosmic activity is mostly caused by minimum ionising particles, whose signature is known, the recorded signal is scaled to take into account the slow component part of the scintillation light missing from the waveform.

6.2.3 Reconstructed-Truth Matching

The information generated by GEANT4 at the propagation stage is often referred to as "true" information. The true information contains a description of the input of the simulation, such as the particle type, the position where it was created, the energy deposits throughout its trajectory and so on. This information, however, is not considered during the reconstruction stage, as reconstruction happens

the same way for simulation and data, where the collected signals are devoid of the true information. For this reason, it is necessary to connect the true and simulated information for simulation samples after the reconstruction stage. This process is called "reconstructed-truth matching" and consists of matching the reconstructed space-points to the true energy deposits. Note that the cosmic events of the overlay MC sample, for instance, do not have true information and for this reason the reconstructed-truth matching cannot be performed. The absence of truth information for cosmic rays in the overlay sample is used as a parameter for topology classification, as shown in Section 7.2.

6.3 Data and MC Samples

This section describes the samples that are used in this analysis:

- **Beam-on Sample [data]**: The "beam-on" sample contains data that was collected whilst MicroBooNE was exposed to the NuMI beam. The collected information is passed through a software filter to select good-quality data to be used for analysis. This filtering involves ensuring the beam intensity, horn current and beam position have the correct values.
- **Beam-off Sample [data]**: The "beam-off" sample contains data that was collected whilst the beam was off. This sample is needed because, given the small neutrino cross section, the detector often records events with only cosmic ray interactions that are in-time with the beam. Since it is difficult to distinguish these events from the ones with a neutrino interaction, it is crucial to correctly model cosmic-only events. The "beam-off" sample enables a precise estimation of events without a beam-induced neutrino interaction that are mistakenly reconstructed as signal.
- **Standard Overlay Monte Carlo Sample [MC+data]**: The "Monte Carlo" sample contains GENIE-generated ν_μ, $\bar{\nu}_\mu$, ν_e, $\bar{\nu}_e$ within the cryostat overlaid with cosmic-ray data.
- **Intrinsic Electron Neutrino Sample [MC+data]**: The "intrinsic electron neutrino" sample is produced the same way as the Monte Carlo one, but it contains only ν_e and $\bar{\nu}_e$ interactions. This sample is used to mitigate the small number of these neutrinos types in the standard Monte Carlo sample.

- **Out-of-Cryostat Sample [MC]**: Beam-induced interactions can happen inside and out of the cryostat. The latter can produce daughter particles that travel inside the cryostat and produce enough light to pass the SW trigger. This kind of event would not be included in the standard overlay nor intrinsic electron neutrino samples, therefore a dedicated GENIE sample is needed to account for it.

A summary of the POT number for all the samples used in this analysis is shown in Table 6.1. The numbers are referring to FHC NuMI Run 1 only.

Sample	POT	Original Number of Events	Normalised Number of Events
Beam-on	2.01×10^{20}	6.14×10^{5}	6.14×10^{5}
Beam-off	9.35×10^{19}	1.20×10^{5}	2.53×10^{5}
Monte Carlo	3.81×10^{20}	1.46×10^{5}	7.70×10^{4}
Intrinsic ν_e	2.33×10^{22}	1.27×10^{5}	1.10×10^{3}
Out-of-Cryostat	1.29×10^{20}	4.75×10^{4}	7.41×10^{4}

Table 6.1: The corresponding number of POT for each sample used in this analysis. The beam-off sample is not recorded during beam time, therefore the equivalent-POT listed here for this sample is calculated as a ratio between the beam-on and beam-off HW triggers, multiplied by the recorded beam-on POT. The last columns display the number of simulated events in the MC sample without (third column) and with (fourth column) the data POT normalisation applied.

As shown in Table 6.1 the samples correspond to different values of POT. To be able to compare the full Monte Carlo sample (which is a combination of the beam-off, standard overlay Monte Carlo, intrinsic electron neutrino and out-of-cryostat samples) to the beam-on sample, it is necessary to scale them. It is a common approach that the recorded beam-on data should stay intact for the analysis, and for this reason the scaling is only applied to the MC samples in order for them to reflect the same beam-on POT. The scaling factor is

$$\mathrm{sf}_{\mathrm{MC}} = \frac{\mathrm{POT}_{\text{beam-on}}}{\mathrm{POT}_{\mathrm{MC}}}, \tag{6.2}$$

for each of the standard Monte Carlo, intrinsic electron neutrino and dirt samples, using their respective POT numbers.

The purpose of scaling these samples is for them to reproduce the numbers in the beam-on sample. Scaling the standard Monte Carlo, the intrinsic electron neutrino, and the dirt samples by the POT ratio is enough since each of them fully reproduce the beam-on sample but in a different scale. The beam-off sample, however, only represents 98% of the beam-on sample. This is because approximately 2% of the beam spills do result in a neutrino interaction, so 98% of the beam-on sample is pure cosmic ray events, which is the definition of the beam-off sample. The scaling factor for the beam-off sample is $\mathrm{sf}_{\text{beam-off}} = 0.98 \times \mathrm{sf}_{\text{MC}}$, to account for this fact.

Chapter 7

Electron Neutrino and Antineutrino Selection

This chapter describes the selection of electron neutrinos and electron antineutrinos in the recorded MicroBooNE data using the NuMI beam. Section 7.1 outlines the functioning operation of the machine learning tool called the Boosted Decision Tree (BDT) that will be used as one of the cores of this analysis. Section 7.3 outlines the selection that is applied to select all the ν_e and $\bar{\nu}_e$ interactions. Section 7.4 shows the selection purity and efficiency achieved after the signal selection.

7.1 Boosted Decision Tree

A BDT is an algorithm used to classify events based on a list of input variables. This analysis uses the eXtreme Gradient Boosting (XGBoost) library [110]. XGBoost is a supervised machine learning method for classification based on decision trees. The term "decision tree" refers to a tree-structured approach. First a full MC dataset is provided where its components are already classified as either "signal" or "background" based on true simulation information. This first step will tell the machinery the kind of signal to be selected. The next step is to provide parameters that will be used by the tool to classify entries as background-like or signal-like. This step works recursively, the idea is that each tree boost will fix mis-classifications from the previous tree, this process is known as "training". The training outcome is saved

into a "model". The model contains the instructions on how to use the input parameters to classify an entry as signal or background, attributing a score from 0, for pure background-like entries, to 1, for pure signal-like entries.

7.1.1 Boosting

Boosting is a technique used in machine learning to build a learning model by combining multiple weak learning models. A weak classifier is a model that performs slightly better than a random guess. This section explain two of the main boosting techniques: gradient boosting and extreme gradient boosting. A boosting technique makes use of a "decision tree" to classify data and to perform predictions. A decision tree, shown in Figure 7.1 contains many levels. The first one, "root node", contains all the entries of the dataset. Then, it is split into smaller sub-samples, "leaf nodes", based on "decision nodes". The group of decision nodes and their output leaf nodes make a "branch".

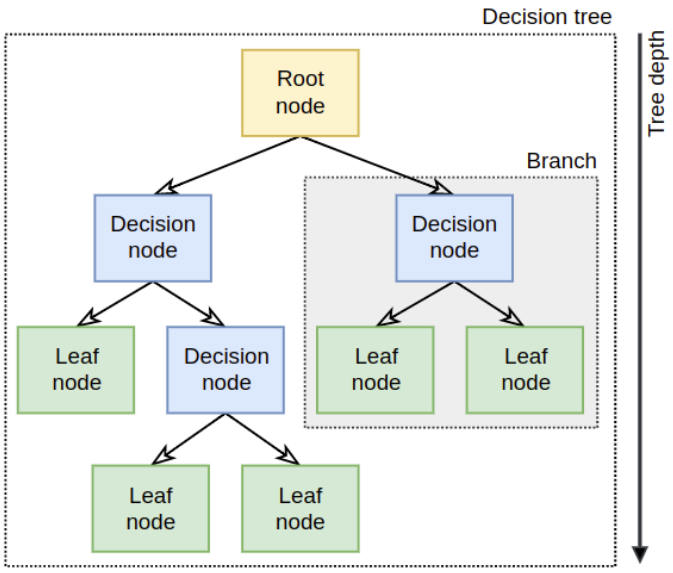

Figure 7.1: Scheme of a decision tree of depth equals 2.

Gradient Boosting

The Gradient Boosting works based on trees that are built at each step of the training. The tree uses information from the dataset to predict values for desired variables. The technique aims to decrease the difference between the real data point value and the predicted one through a "Loss Function" $L(y_i, F(x_i))$ at each step of

the training, where y_i is the observed value and $F(x_i)$ is a function that gives the predicted value. This difference is also known as "residual", r_i. The Loss Function used in this analysis is the logistic regression. The Gradient Boosting process starts by evaluating an initial constant predicted value, $F_0(x)$, defined as

$$F_0(x) = \arg\min_{F(x)} \sum_{i=1}^{n} L(y_i, F(x)). \tag{7.1}$$

To make it easier to understand, consider the following example: a small data sample with information about the height and body weight of 3 individuals, shown in the first three columns of Table 7.1. This section explains step by step the procedure of how this input data is used to train a model to predict a person's body weight based on their height. The columns in Table 7.1 between $F_0(x_i)$ and $F_2(x_i)$ show the auxiliary values as well as the predicted body weight values at each step of the process. Their numerical value is calculated throughout this section. A loss function of $L(y_i, F(x)) = (1/2)[y_i - F(x)]^2$ is used as a conceptual example.

The predicted value that minimises Equation 7.1 is the average of the observed body weights, y_i. This means that the first body weight predicted value for all entries will be $F_0(x) = (88 + 75 + 50)/3 = 71\,\text{kg}$.

Entry	Height (m)	Body Weight (kg)	$F_0(x_i)$	$r_{i,1}$	$O_{i,1}$	$F_1(x_i)$	$r_{i,2}$	$O_{i,2}$	$F_2(x_i)$
1	1.6	88	71	17	10.5	72.05	15.95	9.45	72.99
2	1.76	75	71	4	10.5	72.05	2.95	9.45	72.99
3	1.5	50	71	-21	-21	68.9	-18.9	-18.9	67.01

Table 7.1: Example of dataset to explain the working principle of the Gradient Boosting technique. The first 3 columns show the input values of the dataset: height and body weight of 3 different individuals. Columns $F_m(x_i)$ represent the prediction value per iteration m. Columns $r_{i,m}$ represent the pseudo residual per iteration m, defined in Equation 7.2. Columns $O_{i,m}$ represent the output value per iteration m, defined in Equation 7.3.

The next step is to calculate the "pseudo residuals" for each stage level, m, based

on the previous prediction, $F_{m-1}(x)$. The "pseudo residual" is defined as

$$r_{i,m} = -\left[\frac{\partial L(y_i, F(x_i))}{\partial F(x_i)}\right]_{F(x_i)=F_{m-1}(x_i)}, \tag{7.2}$$

where i is the entry number. For the loss function used in this example, the pseudo residual is the difference between the original body weight and the predicted value in the previous stage. Therefore, the pseudo residual for $m = 1$, $r_{i,1}$, is the difference between the body weight and $F_0(x_i)$ per entry, as shown in Table 7.1. The next step consists of creating a tree to split the residual values into sub-groups. Consider the tree displayed in Figure 7.2 where the dataset is split into two sub-samples based on their "heights", this example uses a threshold of "height $< 1.57\,\mathrm{m}$". An "output value", defined as

$$O_{j,m} = \arg\min_{O} \sum_{x_i \in R_{i,j}} L\left(y_i, F_{m-1}(x_i) + O\right), \tag{7.3}$$

is assigned for each leaf, j, where $R_{i,j}$ is the group of entries in leaf j. After doing the math one can see that the output value for leaf $R_{1,1}$ is $O_{1,1} = -21$, and the one for leaf $R_{2,1}$ is $O_{2,1} = 10.5$.

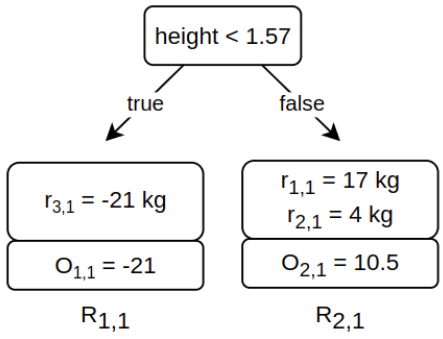

Figure 7.2: Example of a tree showing the dataset split based on the variable "height". This tree displays the first residual per entry i, $r_{i,1}$, on each leaf based on the condition "height < 1.57", as well as the output value per leaf j, $O_{j,m}$, where m is the iteration number. Each leaf is labelled as $R_{m,j}$, where m is the iteration number and j is the leaf number.

A new prediction can be made based on the output values of this tree. The new

prediction is calculated as

$$F_m(x_i) = F_{m-1}(x_i) + \nu O_{j,m}, \tag{7.4}$$

where ν is the learning rate and j leaf number the entry i belongs to. The value of the learning rate is defined by the user and it can go from 0 to 1. Considering $\nu = 0.1$, the new predicted value for entries in Table 7.1 are

$$F_1(x_1) = 71 + (0.1 \times 10.5) = 72.05 \tag{7.5}$$

$$F_1(x_2) = 71 + (0.1 \times 10.5) = 72.05 \tag{7.6}$$

$$F_1(x_3) = 71 + (0.1 \times (-21)) = 68.9. \tag{7.7}$$

The new predicted values, $F_1(x_i)$, are displayed in Table 7.1. Note that $r_{i,2} < r_{i,1}$ which means that $F_1(x_1)$ is a better prediction than $F_0(x_i)$ to the real body weight value. These steps are repeated M times, where M is defined by the user. Table 7.1 shows the residual, output and prediction values for iterations up to $m = 2$.

It is possible now to perform a prediction with this small example. If the next entry is 1.54 m tall, then this model will predict its body weight is 67.01 kg, as shown in Figure 7.3.

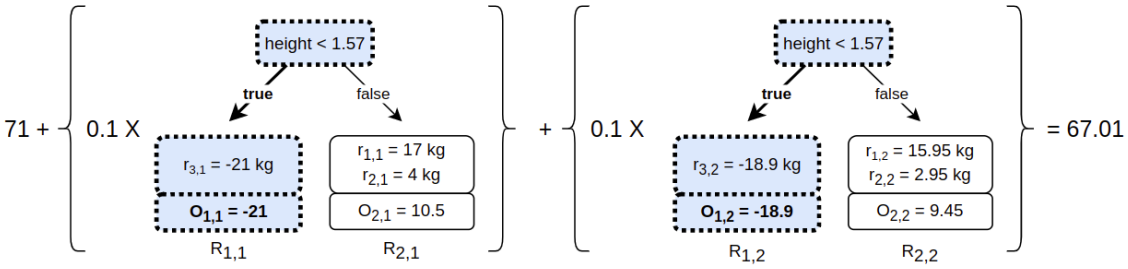

Figure 7.3: Body weight prediction for a new entry of height 1.54 m using the simple model trained in this section.

A more realistic model has a more complex tree than the one used in this example, and results in a better prediction.

Extreme Gradient Boosting

The Extreme Gradient Boosting, XGBoost, is another boosting technique that also makes use of many steps to perform a prediction. XGBoost is designed to be

used with large data-sets. The analysis done in this thesis uses XGBoost. The initial steps are similar to the ones used by Gradient Boosting. First an initial predicted value for a given value is assumed, F_0. Similarly to the Gradient Boosting technique, the Extreme Gradient Boosting fits a tree to the residuals, r_i, with respect to F_0.

There are many ways to build a tree. The example above defines the decision node as the condition "height $< 1.57\,\mathrm{m}$", however other thresholds could have been used to split the data-set into sub-samples, for instance "height $< 1.64\,\mathrm{m}$", resulting in different leafs. Extreme Gradient Boosting evaluates all possible tree and chooses the best one based on their "gain" defined as

$$G = \sum_j S_j - S_{\mathrm{root}}, \tag{7.8}$$

where S_{root} and S_j are the "similarity score" at the root of the tree, and per leaf j respectively, defined as

$$S_j = \frac{\left(\sum_i r_i\right)^2}{N_r + \lambda}, \tag{7.9}$$

where N_r is the number of residuals per leaf and λ is a regularisation parameter. The larger the gain, the better the tree is in splitting the residuals into clusters of similar values. Figure 7.4 shows the similarity score and gain for the possible trees in the previous example: with thresholds "height $< 1.57\,\mathrm{m}$" or "height $< 1.64\,\mathrm{m}$" and $\lambda = 0$.

The same exercise can be done again to continue splitting the leafs into smaller ones. This process will happen recursively until the "tree depth" is reached. The "tree depth" is chosen by the user and it represents the number of levels in a tree.

Once the tree is built, it is "pruned" the tree based on the gain values and a value chosen by the user, γ. Starting from the branches in the bottom, for each branch, the difference between its gain and γ, $\Delta\Gamma \equiv G - \gamma$ is calculated. If $\Delta\Gamma < 0$ the branch is removed, otherwise it is kept. The pruning process stops at the first branch where $\Delta\Gamma$ is positive, even if upper branches have negative $\Delta\Gamma$. The user can tune the values of λ and γ to achieve a better model performance. The larger the value of λ the smaller is the "gain" and therefore the tree is more susceptible to pruning, avoiding over fitting the training data.

Similarly to the Gradient Boosting process, the Extreme Gradient Boosting cal-

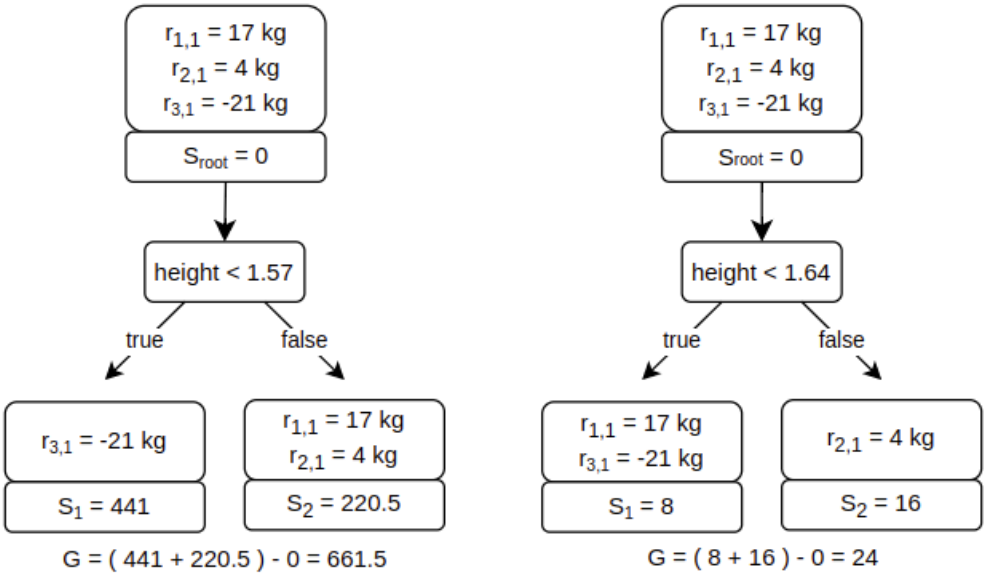

Figure 7.4: Example of tree using two different thresholds based on "height". The tree on the left has a higher gain in comparison to the one on the right, which indicates that the tree on the left clusters the entries better.

culates an "output value" for each leaf as

$$\mathrm{O} = \frac{\sum_i r_i}{N_r + \lambda}, \tag{7.10}$$

and the new prediction is calculated as the $F_1 = F_0 + (\varepsilon \times O)$, where F_0 is the first prediction, ε is the learning rate, and O is the output of the tree.

This section explained the methodology used by the Gradient Boosting and Extreme Gradient Boosting techniques to train a model. It used a simplified situation where the data sample is made of information about height and body weight of 3 different individuals. The work of this thesis uses the Extreme Gradient Boosting technique to train a model to distinguish between electron neutrino and electron antineutrino events in the MicroBooNE detector. The training is done using the kinematic information of these events as input for the model, as will be explained in Section 8.1.

7.1.2 Evaluating the performance of BDT model

The performance of the BDT model described in this section can be quantified through a Receiver Operating Characteristic (ROC) curve and a Area Under (the ROC) Curve (AUC). A ROC curve shows the performance of a classification model at all thresholds as a function of "true positive rate" and "false positive rate". A true positive is when a signal is correctly classified as signal, and background as background. Whilst a false positive is when a signal is classified as background, and vice versa.

The ROC curve can have three regimes: perfect classifier, random classifier, and good classifier, as shown in Figure 7.5. In the "perfect classifier" regime the model perfectly distinguishes signal from background, assigning the correct BDT score to each category, shown in Figure 7.5 (top left). The separation power in this case is maximum. In the "random classifier" regime, the BDT model does not have any separation power, and it is not possible to distinguish signal from background as their BDT score distributions fully overlap, shown in Figure 7.5 (top right). The most common situation is that the BDT model performs as a "good classifier". In this regime, the model presents a good separation power despite having some overlap between the signal and background distributions shown in Figure 7.5 (top centre).

The AUC measures the integrated area underneath the ROC curve. This quantity represents the probability that the model will correctly distinguish between positive class and negative class, as shown in the bottom line of Figure 7.5

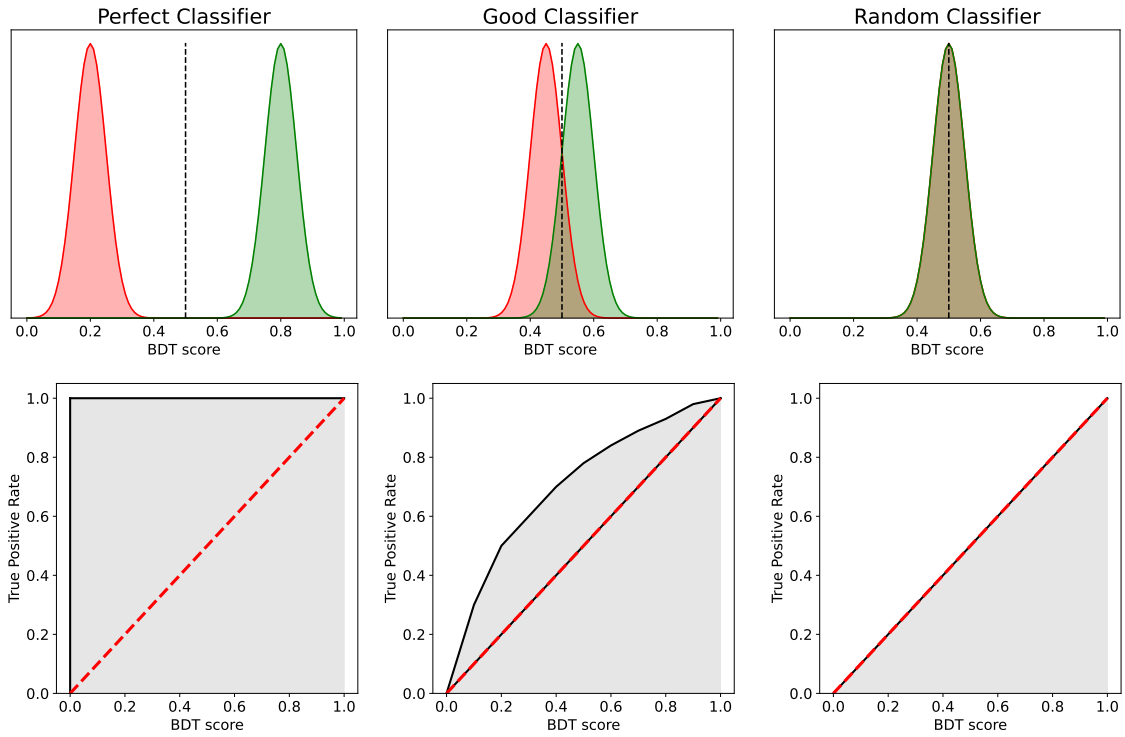

Figure 7.5: Scheme of three possible regimes for the BDT model. The top line shows the distribution for signal (green) and background (red), and the bottom line shows the AUC curve for each regime. These are illustrative plots. The left column represents the "perfect classifier" regime, where the separation power is maximum between signal and background and AUC=1. The mid columns represents the "good classifier" regime, where there is some level of overlap between the signal and background distributions but it still has a good separation power, 0.5 <AUC< 1. And the right column represents the "random classifier", where there is no separation power and AUC=0.5.

7.2 Event Classifications

To be able to understand the effect of each selection cut, it is helpful to distinguish the simulated events by their topology. The topology of the reconstructed MC events are classified using the truth matching information, described in Section 6.2.3. The ten topologies used in this analysis are:

- **Cosmic [data]**: Events classified as "cosmic activity" due to the absence of truth information.

- **OutFV** [**MC**]: Neutrino events whose vertex is simulated outside the fiducial volume, and are not cosmics. The "fiducial volume" is defined as a region 3 cm from the TPC walls.
- ν_μ**CC**π^0 [**MC**]: Any ν_μ or $\bar{\nu}_\mu$ CC interactions with a π^0 in the final state, and that do not match any classification above.
- ν_μ**CC** [**MC**]: Any ν_μ or $\bar{\nu}_\mu$ CC interactions without a π^0 in the final state, and that do not match any classification above.
- **NC**π^0 [**MC**]: All NC interactions with a π^0 in the final state, and that do not match any classification above.
- **NC** [**MC**]: All NC interactions without those with a π^0 in the final state, and that do not match any classification above.
- ν_e**CC** [**MC**]: All ν_e CC interactions that do not match any classification above.
- $\bar{\nu}_e$**CC** [**MC**]: All $\bar{\nu}_e$ CC interactions that do not match any classification above.
- **Beam-Off** [**data**]: All events collected whilst the beam was off.
- **Out-of-Cryo** [**MC**]: All neutrino interactions from the Out-of-Cryostat sample.

Explicitly classifying events based on the presence or absence of π^0 is important because, as explained earlier in the thesis, π^0 have very similar signature to $e^\pm$ in the detector, both create showers.

7.3 Signal Selection

A set of four selection cuts are used to select the $\nu_e + \bar{\nu}_e$ and reject the background interactions.

7.3.1 Cosmic Ray Rejection

The cosmic ray rejection consists of a combination of clustering techniques to separate neutrino interactions from cosmic-ray muons [109], without imposing restrictions on

the neutrino nature. For this reason it is also known as *generic neutrino selection*. Event reconstruction in the WireCell framework is done for neutrino candidates that pass the generic neutrino selection. For this reason, applying this cut is necessary for any analysis using WireCell to avoid non-reconstructed events in the sample.

The MicroBooNE detector is located at the surface, which results in 20-30 cosmic ray muons crossing the detector during the 4.8 ms readout window. Removing the cosmic ray background is, therefore, one of the main challenges and a necessity in order to be able to take full advantage of the capability of the detector [111]. Table 7.2 shows the number of events before any selection cuts are applied, demonstrating how much cosmic-ray contamination there is at the MicroBooNE detector. The topologies are classified based on the description in Section 7.2.

Classification	Events
Cosmic	105 670.09
OutFV	16 292.06
ν_μCCπ^0	2 684.07
ν_μCC	14 504.30
NCπ^0	1 232.73
NC	2 727.65
ν_eCC	708.81
$\bar{\nu}_e$CC	142.36
Out-of-Cryo	74 138.58
Beam-off	253 015.02
Beam-on	613 755

Table 7.2: Number of interactions per topology for the full NuMI Run 1 data, before any selection cut is applied.

The neutrino candidate classification starts by performing a light-charge matching, where TPC clusters and PMT flashes are checked for coincidences in time. When the reconstruction succeeds in grouping the recorded signals, one TPC cluster matches one PMT flash. However if reconstruction fails in grouping signals, one PMT flash can match with multiple TPC clusters. Another possibility is when a TPC cluster matches with zero PMT flashes (for instance for low-energy neutrino

interactions whose generated scintillation light does not pass the PMT threshold) and vice-versa (for instance for activities recorded outside the TPC active volume). Clusters matched to PMT flashes happening outside of the beam window are classified as cosmics events and rejected.

The light-charge matching process is not enough to select a pure neutrino interaction sample, since cosmic activity can happen in-time with the beam. The remaining background is dominated by Through-Going Muons (TGM) and Stopping Muons (STM).

The first group is easily identified by evaluating the extreme points of the trajectory. Tracks that cross the detector and whose extreme points lay within the borders of the active volume of the detector (defined as 3 cm from the physical boundaries of the TPC) are classified as TGMs, as shown in Figure 7.6 (right). All TPC clusters associated to TGMs are removed from the selected sample.

The second group consists of entering muons that stop inside the detector. There are two ways of differentiating STM tracks from muon tracks produced in a neutrino interaction. The first one uses the track direction, whilst neutrino-induced muon tracks start inside the detector and travel outward, cosmic STM activity is formed by tracks entering the detector. One way to determine the track direction is by evaluating the reconstructed charge per unit (dQ/dx) at the end of the track, because there is a rise in dQ/dx at the end of the track, also known as a Bragg peak, as shown in Figure 7.7. These events are sometimes followed by an additional short track from the Michel electron, as shown in Figure 7.6 (left).

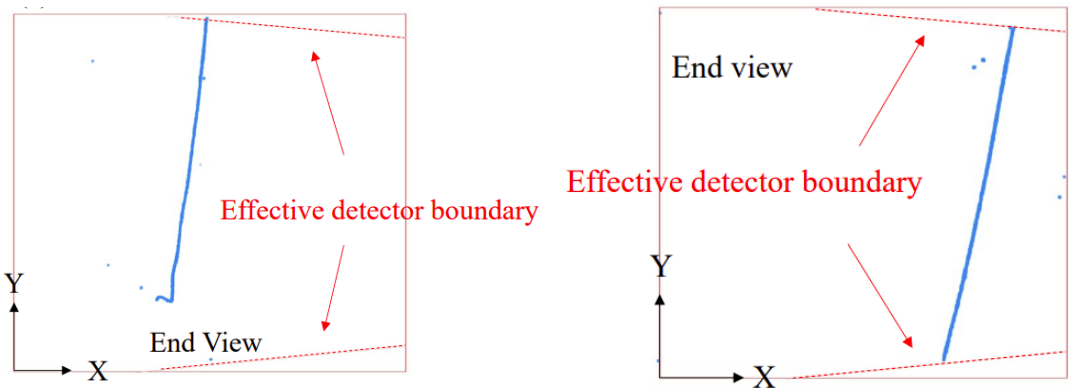

Figure 7.6: Examples of a track caused by a STM (left) and by a TGM (right). Figure from [112].

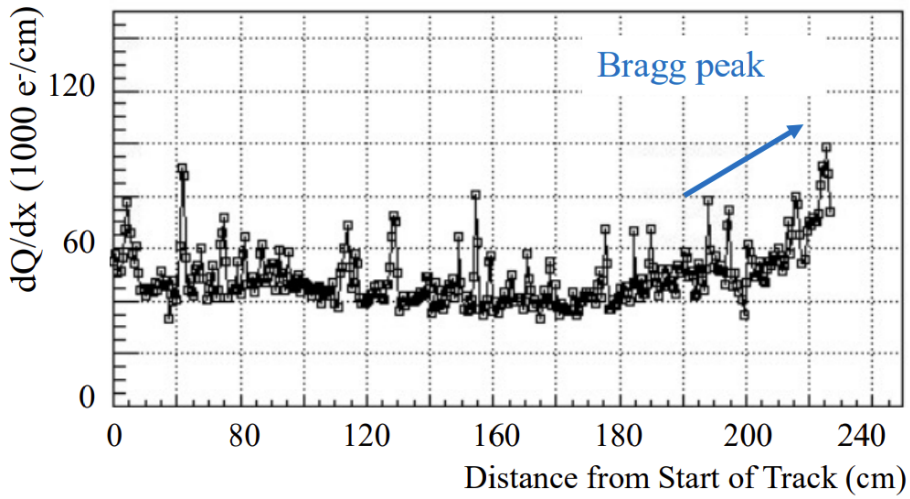

Figure 7.7: Example of a dE/dx distribution for a stopping muon. The rise in dQ/dx at the end of the track characterises the Bragg peak. Figure from [112].

The third group of background events is formed by Light-MisMatched (LMM) events. These events are often caused by the inefficiency of the PMT system to detect events that happen close to the cathode and the scintillation light produced by events outside the TPC active volume. A Kolmogorov-Smirnov (KS) test is performed to check the consistency between the observed and the predicted light pattern. Events are tagged as LMM and rejected when low consistencies are observed.

The generic neutrino selection removes 98% of the recorded cosmic ray interactions. Table 7.3 displays the number of interactions per topology. The table contains four columns: the first one specifies the topology classification according to description in Section 7.2; the second one displays the number of events per topology; the third one shows the survival percentage per topology when compared to the previous stage; and the fourth one shows the absolute survival percentage per topology when compared to the number of entries at the beginning of the selection chain.

Figure 7.8 shows the neutrino energy distribution after applying the generic neutrino selection requirement. A distribution such as the one in Figure 7.8 will be shown at each stage of the selection chain. This distribution compares the stacked prediction (MC + beam-off data) to beam-on data at each selection cut. The beam-on data is represented as black-dots and its systematic uncertainty is calculated following a Poisson distribution. The statistical uncertainty for the MC topologies deserves special attention. To avoid ending up with a large statistical uncertainty

caused by the small ν_eCC and $\bar{\nu}_e$CC statistics in the standard monte carlo simulation, the statistical uncertainty for these two topologies is calculated and reduced with the help of the intrinsic electron neutrino sample. First, the same set of selection cuts is applied on the intrinsic electron neutrino sample, resulting in a $N_i^{intrinsic}$ selected events for the topologies i, where i is either ν_eCC or $\bar{\nu}_e$CC. Then a Poisson statistical uncertainty is calculated for each bin as $\sqrt{N_i^{intrinsic}}$ and then normalised by $1/n$ where $n = N_i^{intrinsic}/N_i^{mc}$ and N_i^{mc} is the number of selected events in the standard monte carlo overlay sample.

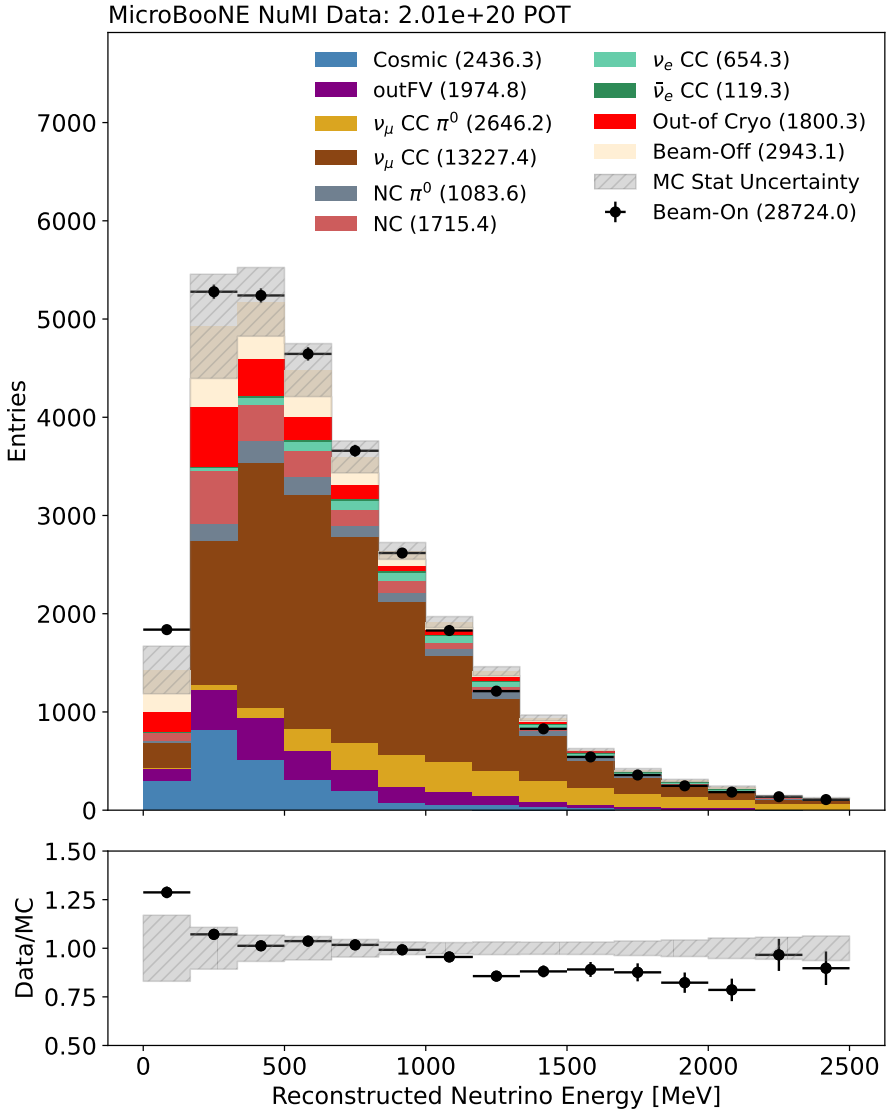

Figure 7.8: Neutrino energy distribution after applying the wire-cell cosmic ray rejection. Most of the cosmic ray contribution is removed, without prioritising the selection of any neutrino flavour.

Classification	Events	Survival Percentage since Previous Stage	Absolute Survival Percentage
Cosmic	2 613.44	2.47%	2.47%
OutFV	2 055.47	12.61%	12.61%
ν_μCCπ^0	2 646.21	98.59%	98.59%
ν_μCC	13 663.79	94.21%	94.21%
NCπ^0	1 164.20	94.44%	94.44%
NC	1 769.78	64.88%	64.88%
ν_eCC	701.06	98.91%	98.91%
$\bar{\nu}_e$CC	138.89	97.56%	97.56%
Out-of-Cryo	1 839.40	2.48%	2.48%
Beam-off	2 996.78	1.18%	1.18%
Beam-on	30 138	4.91%	4.91%

Table 7.3: Number of interactions per topology after applying the cosmic ray rejection. Because the cosmic ray rejection is the first selection applied in this analysis, the "survival percentage since previous stage" is equal to the "absolute survival percentage".

7.3.2 Vertex Containment

The MicroBooNE detector is placed inside a cylindrical cryostat. The entire cryostat is filled with liquid argon that neutrinos can interact with. Therefore, both the volume inside the TPC instrumented region, as well as the volume between the TPC and the interior part of the cryostat can become a target for neutrino interactions. However it is difficult to analyse the signals coming from outside the instrumented region of the detector, and they are commonly removed from the analysis. A "fiducial volume" is defined as a region within the TPC, 3 cm away from all the edges, to remove all the reconstructed vertices that are close to the boundaries of the detector and outside. The fiducial volume used in this analysis is $5.9 \times 10^7\,\mathrm{cm}^3$, with the boundaries defined in Table 7.4. Figure 7.9 shows the neutrino energy distribution after imposing the containment condition, and Table 7.5 displays the number of interactions per topology.

Coordinate	Lower Limit (cm)	Upper Limit (cm)
x	3.00	251.3
y	-118.0	114.0
z	3.6	1033.4

Table 7.4: The fiducial volume is defined as a volume 3 cm from the TPC boundaries of the MicroBooNE detector, and in this analysis this volume is limited by the coordinates described above.

Classification	Events	Survival Percentage since Previous Stage	Absolute Survival Percentage
Cosmic	2 081.51	79.65%	1.97%
OutFV	1 590.99	77.40%	9.77%
ν_μCCπ^0	2 542.68	96.09%	94.73%
ν_μCC	13 180.56	96.46%	90.87%
NCπ^0	1 105.65	94.97%	89.69%
NC	1 701.74	96.16%	62.39%
ν_eCC	679.39	96.91%	95.85%
$\bar{\nu}_e$CC	134.68	96.97%	94.61%
Out-of-Cryo	1 501.91	81.65%	2.03%
Beam-off	2 616.57	87.34%	1.03%
Beam-on	27 275	90.50%	4.44%

Table 7.5: Number of interactions per topology after applying the vertex containment condition.

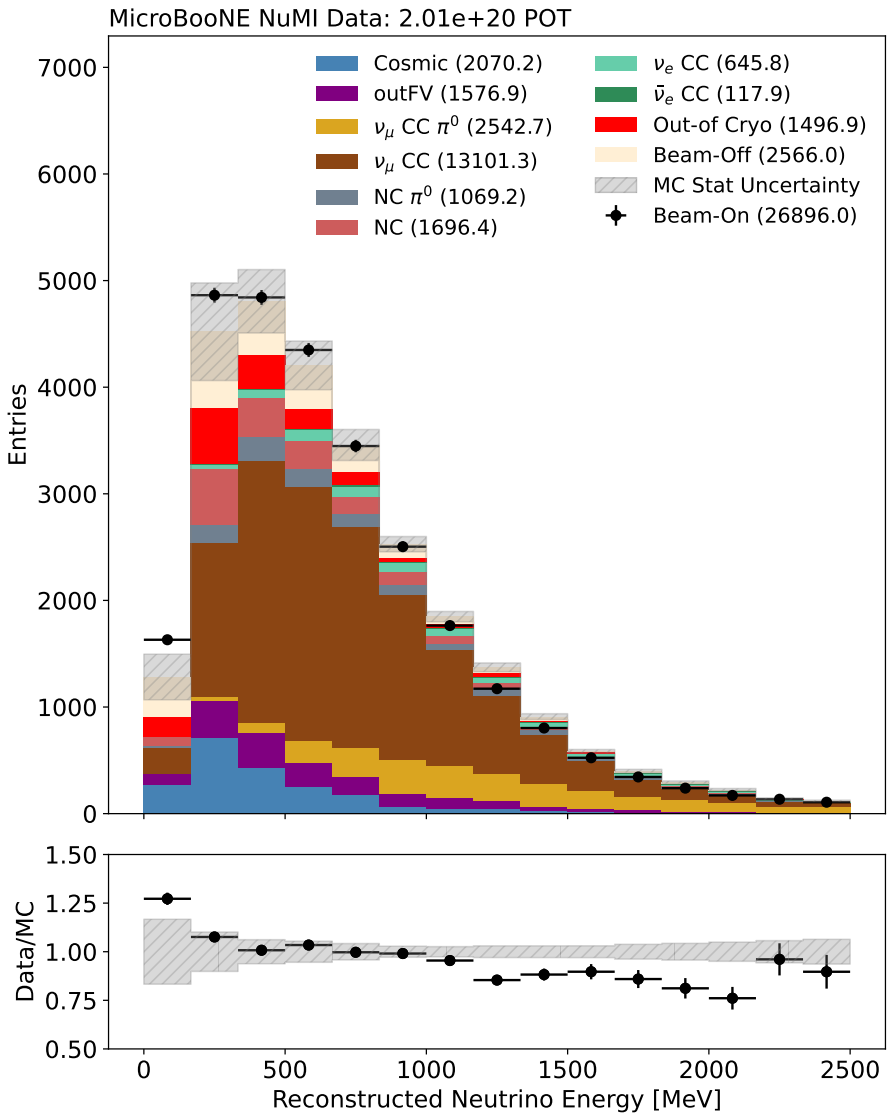

Figure 7.9: Neutrino energy distribution after imposing the vertex containment condition. This step does not affect the distribution significantly but it is crucial to guarantee that the analysis only uses events whose reconstruction we trust.

7.3.3 Shower Identification

The signature of electron-neutrino and antineutrino interactions in a LArTPC is the presence of at least one electron-like shower. Therefore, every event without a reconstructed shower is removed in this analysis.

WireCell differentiates tracks from electromagnetic showers as follows. For low-energy electrons, the bremsstrahlung effect is small and not sufficient to generate a full cascade. In the absence of a shower-like signature, low-energy electrons can end up having a track-like behaviour in the detector. However, they go through multiple Coulomb scatterings, their low mass results in a wiggled track instead of a straight one, for example caused by a muon. This effect is one of the features used to differentiate tracks from showers, and it is shown in Figure 7.10 (a). The presence of nearby clusters can also be used to identify an EM shower, as shown in Figure 7.10 (b), since muon-like tracks are characterised by the absence of those secondary signals

On the other hand, high-energy electrons will have a smaller deviation in their trajectory in comparison to low-energy ones, but now the bremsstrahlung effect is stronger. For this reason more secondary electrons and positrons are produced, resulting in a perpendicular spread along the EM shower direction, as shown in Figure 7.10 (c). The width of this spread is used not only to distinguish showers from tracks, since tracks have no spread, but also to identify the starting point of the EM shower.

Figure 7.11 shows the energy distribution after requesting the presence of a shower, and Table 7.6 shows the number of interactions per topology. Showers are often caused by electron and π^0 particles, which explains why this cut has a higher survival percentage for topologies containing one of those particles, such as ν_μCCπ^0, NCπ^0, ν_eCC and $\bar{\nu}_e$CC, as shown in Table 7.6.

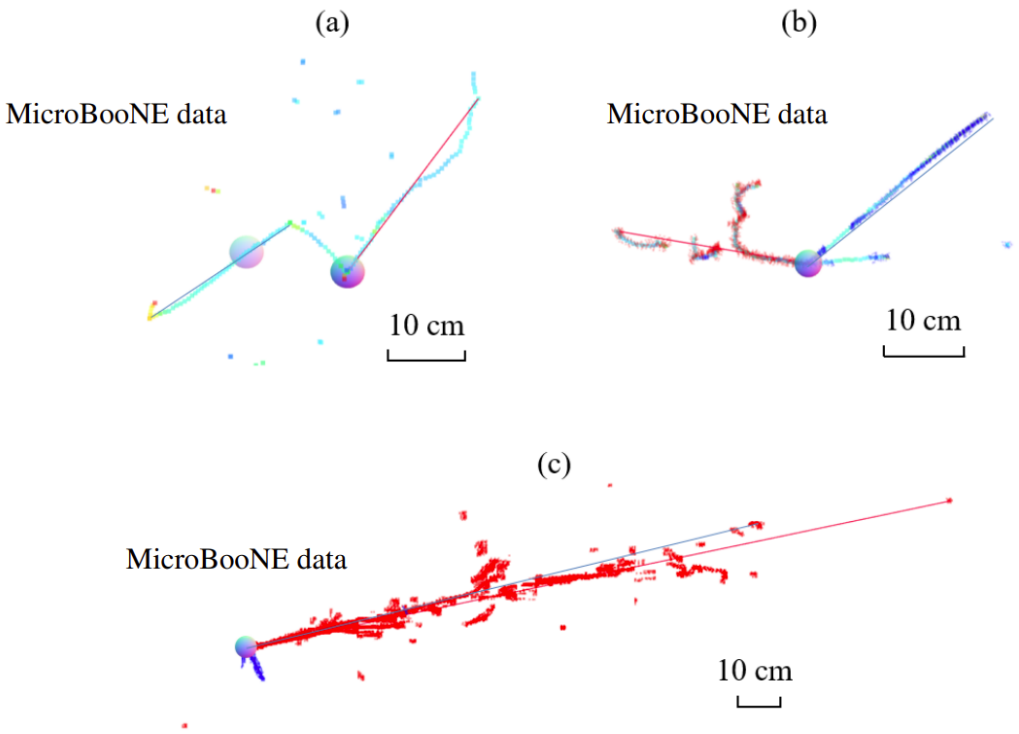

Figure 7.10: Examples of EM interactions. (a) low-energy wiggled track, (b) track with two isolated showers (shower-like objects are indicated by red colour and track-like objects are indicated by blue colour) , (c) an EM shower from a high-energy electron. The colours represent the reconstructed charge for each space point, where the blue, cyan, green, yellow, and red colours represent from less to more charge, respectively. Rainbow circles indicate particle starting positions. Figure from [113].

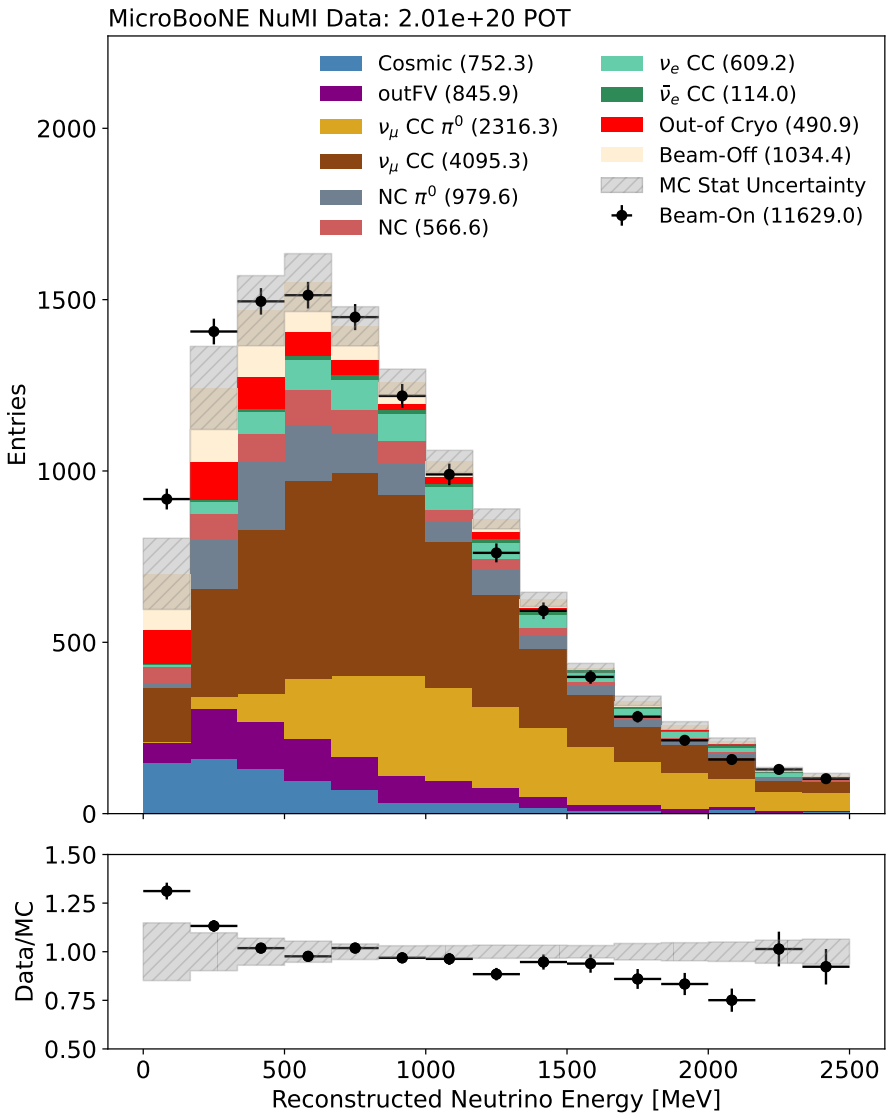

Figure 7.11: Neutrino energy distribution after requesting the presence of a shower. This step mostly affects the muon-like events, because muons are responsible for creating a track-like signal in the detector rather than a shower-like one.

Classification	Events	Survival Percentage since Previous Stage	Absolute Survival Percentage
Cosmic	763.57	36.68%	0.72%
OutFV	859.31	54.01%	5.27%
ν_μCCπ^0	2 316.32	91.10%	86.30%
ν_μCC	4 166.79	31.61%	28.73%
NCπ^0	1 016.00	91.89%	82.42%
NC	571.37	33.58%	20.95%
ν_eCC	642.73	94.60%	90.68%
$\bar{\nu}_e$CC	130.7	97.04%	91.81%
Out-of-Cryo	495.88	33.02%	0.67%
Beam-off	1 082.86	41.38%	0.43%
Beam-on	12 002	44.00%	1.96%

Table 7.6: Number of interactions per topology after applying the shower condition.

7.3.4 Electron Neutrino and Antineutrino Selection

The charged-current ν_eCC event selection [114] is a challenging task as the signal-to-background ratio is about 1:190 after the generic neutrino selection. The MicroBooNE collaboration has developed a tool to select ν_eCC and $\bar{\nu}_e$CC as part of the existing efforts to search for the ν_e low-energy excess. This tool was developed in two stages. The first stage was done by hand scanning $O(1000)$ events to extract features (i.e. variables) that can be used to reject background. The basic selection of inclusive ν_eCC events requires an EM shower with a reconstructed energy higher than $\sim 60\,\text{MeV}$ connecting to the primary neutrino vertex. The energy threshold is placed to exclude Michel electrons. The selected variables can be separated into the following groups:

- **Electron identification:** focused on analysing the produced shower, imposing (i) a good quality reconstructed shower without track overlaps or splitting at the beginning of the shower, (ii) that there is no gap at the beginning of the reconstructed shower (unlike in the case of a photon-induced shower), and (iii) that the deposited energy at the beginning of the shower corresponds to an electron-like event.
- **Background rejection:** focused on background rejection with kinematic information, such as the shower angle (when an EM shower goes backwards with respect to the neutrino beam direction).
- **Unreliable pattern recognition:** focused on cases with unreliable pattern recognition caused by a number of factors, which includes badly reconstructed events and tracks overlapping at the beginning of EM showers.

The full list of the 24 chosen variables can be found in [114]. These variables were then used in machine learning techniques with large statistics of Monte Carlo events to develop the ν_eCC selection. This BDT model achieves 91% ν_eCC $+\bar{\nu}_e$CC purity, as can be seen in Figure 7.12. This step is highly efficient in rejecting non ν_eCC and $\bar{\nu}_e$CC events, as shown in Table 7.7.

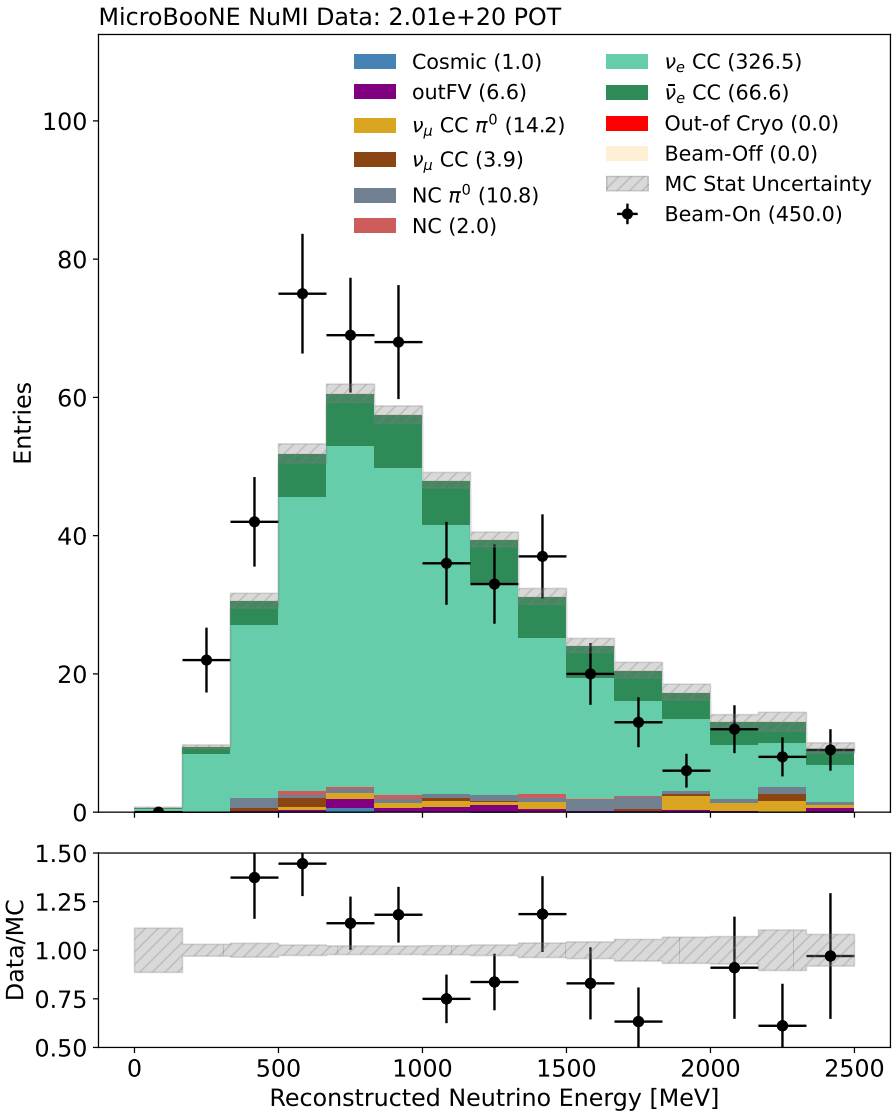

Figure 7.12: Neutrino energy distribution after applying the electron neutrino and antineutrino selection.

Classification	Events	Survival Percentage since Previous Stage	Absolute Survival Percentage
Cosmic	1.00	0.13%	0%
OutFV	7.10	0.83%	0.04%
ν_μCCπ^0	14.23	0.61%	0.53%
ν_μCC	4.44	0.11%	0.03%
NCπ^0	13.22	1.30%	1.07%
NC	1.99	0.35%	0.07%
ν_eCC	347.78	54.11%	49.07%
$\bar{\nu}_e$CC	77.75	59.49%	54.62%
Out-of-Cryo	0.00	0%	0%
Beam-off	0.00	0%	0%
Beam-on	476	3.97%	0.08%

Table 7.7: Number of interactions per topology after applying the electron neutrino and antineutrino selection.

7.4 Selection Efficiency and Purity

The event selection described in this section has an overall ν_eCC + $\bar{\nu}_e$CC purity of 91% and a selection efficiency of 50%. Purity is defined as the number of selected events of a given topology divided by the total number of selected events. Selection efficiency is defined as the number of selected events of a given topology divided by the number of events of the same topology at the beginning of the selection chain. The selection efficiency as a function of the true neutrino energy is similar for ν_eCC and $\bar{\nu}_e$CC, as shown in Figure 7.13. This is important for this analysis because it means that the selected events have a similar ratio to the one originally simulated, and therefore the selection is not introducing a bias into the analysis.

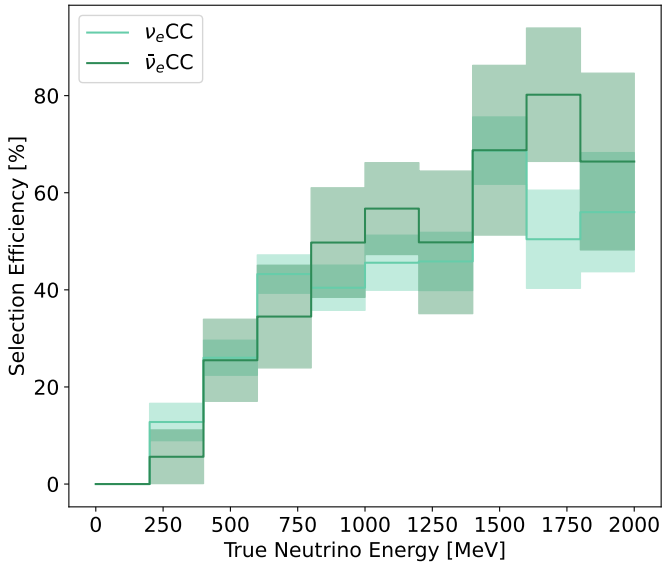

Figure 7.13: Selection efficiency for ν_eCC and $\bar{\nu}_e$CC as a function of the true neutrino energy. The efficiency uncertainty is calculated as $\sigma_\epsilon = \sqrt{(\epsilon/N) \times (1-\epsilon)}$ [115], where ϵ is the efficiency, and N is the number of true events in the fiducial volume.

The selection efficiency per selection step is shown in Figure 7.14. This plot shows how much each step of the selection chain impacts the individual topologies. There are three steps with the most impact in selecting ν_e and $\bar{\nu}_e$ interactions. The first one is the generic neutrino selection that removes most of the non neutrino interactions. The second one is the requirement of a presence of a shower, this step removes the muon neutrino and NC interactions. And finally, the ν_eCC +$\bar{\nu}_e$CC BDT removes most of the non-ν_eCC and non-$\bar{\nu}_e$CC interactions.

The selection purity per selection step is shown in Figure 7.15. This plot shows that the original MC sample is vastly dominated by beam-off events. After applying the generic neutrino selection, that rejects most of the non neutrino interactions, the sample becomes ν_μ-dominated because NuMI Run 1 operated in the neutrino mode and has a large component of ν_μ. The purity has an abrupt change after applying the ν_eCC +$\bar{\nu}_e$CC BDT, since this step has a high efficiency in rejecting backgrounds.

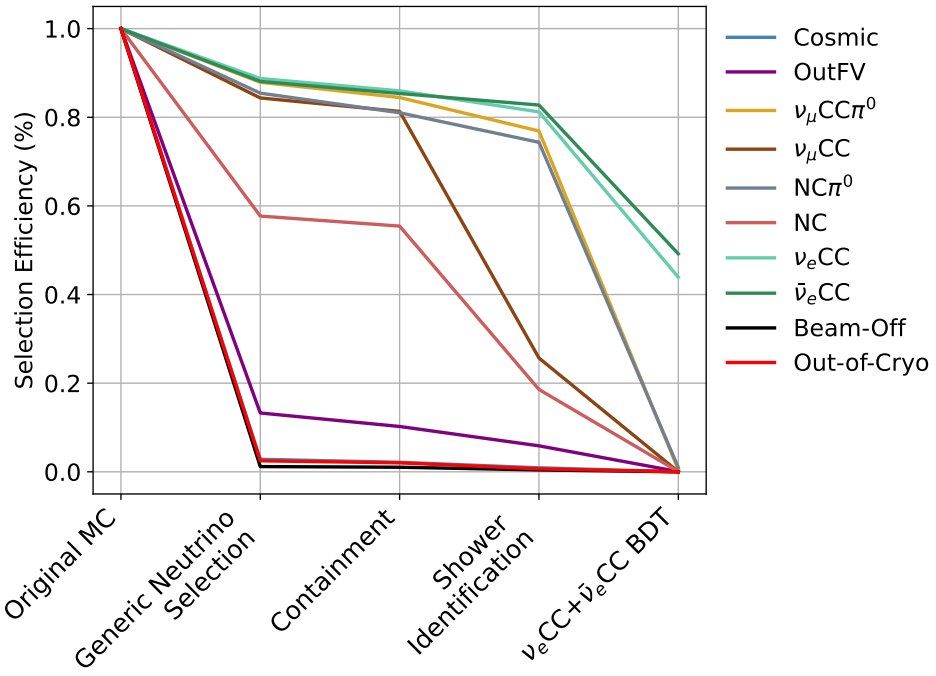

Figure 7.14: Selection efficiency as a function of the event selection step.

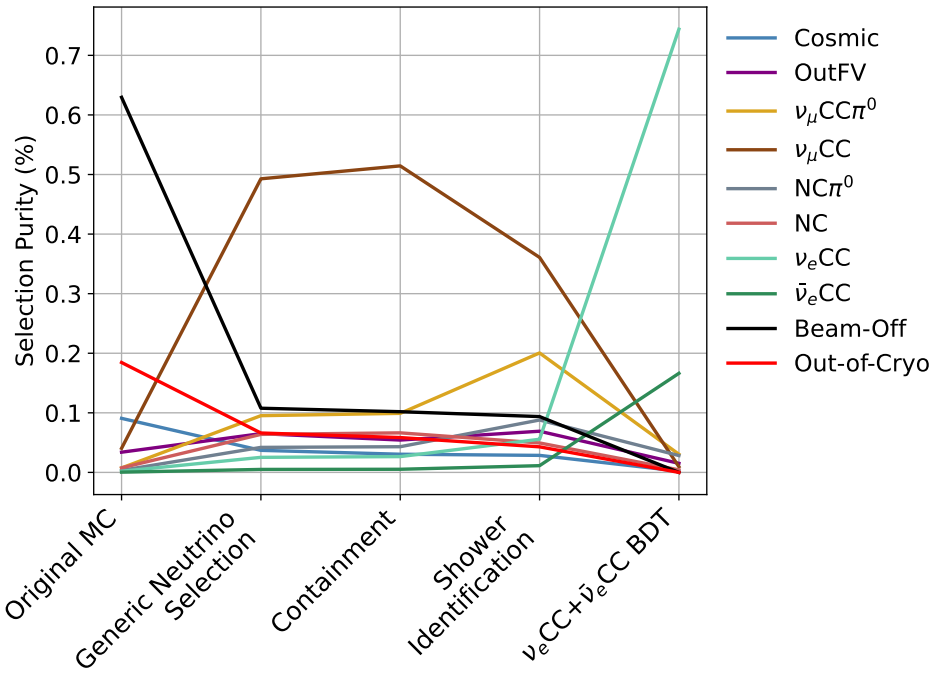

Figure 7.15: Purity as a function of the event selection step.

Chapter 8

Electron Antineutrino BDT

This chapter describes the Boosted Decision Tree used in this analysis to distinguish electron neutrinos from electron antineutrinos from the NuMI beam at the MicroBooNE detector. This work is my original contribution to this field. At this point, a fairly pure ν_eCC + $\bar{\nu}_e$CC sample has been selected, but these two topologies are still mixed. In order to be able to calculate their individual cross sections, it is necessary to distinguish them, and this will be described in this section.

8.1 BDT Variables

As described previously, ν_eCC interactions produce electrons and $\bar{\nu}_e$CC interactions produce positrons. Both these interactions have the same signature in the TPC, in that they create an electron-like shower at the neutrino interaction vertex. For this reason, differentiating between ν_eCC and $\bar{\nu}_e$CC interactions is challenging in this kind of detector, and has never been performed before. In this analysis I have developed the first BDT to make this distinction using kinematic properties of those interactions using neutrinos from the NuMI beam at the MicroBooNE detector.

For a BDT to perform well, it is necessary for the input variables to have different behaviour for "signal" and "background". In this analysis, "signal" is defined as well-reconstructed $\bar{\nu}_e$CC interactions in the fiducial volume, whilst "background" is defined as all the events that do not fall into the definition of "signal". The variables used to train the BDT in this analysis are:

- Reconstructed daughter-particle multiplicity (neutron, muon, proton, gamma, electron). There is no sign distinction since LArTPCs cannot tell apart particle from antiparticle. The particle multiplicity is based on information provided by GENIE, and for this reason this is a model-dependent analysis. Neutrons are neutral particles and for this reason are not directly detected by the MicroBooNE experiment. A reconstructed neutron is defined in the WireCell reconstruction process based on missing energy.

- Angle between the neutrino beam and the produced shower. The neutrino beam is assumed to be a constant vector between the NuMI target and the neutrino interaction point, schematised in Figure 8.1.

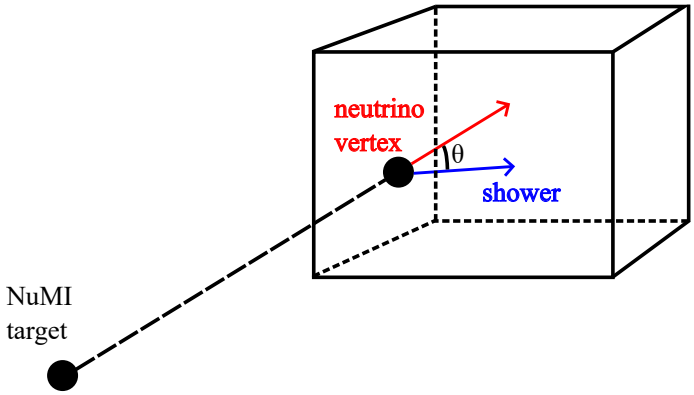

Figure 8.1: Scheme of the $\cos(\theta)$ used as one of the parameters to develop the BDT model.

- Reconstructed neutrino energy and reconstructed shower energy.

Variables such as kaon and pion multiplicity, as well as the neutrino reconstructed vertex position (x, y, z) did not result in significant importance for the BDT training. For this reason they were removed from this analysis. Most of the reconstructed kinematic properties used to train the BDT have very similar behaviour for ν_eCC and $\bar{\nu}_e$CC interactions, as shown in Figures 8.2-8.4. The plots are displayed as area normalised, where the area of the plot is equals 1, to evidence the shape of each distribution. Figure 8.5 (left) shows the importance of each variable for the training of the BDT model. The most effective variable for distinguishing ν_eCC from $\bar{\nu}_e$CC interactions is the angle between the neutrino beam, estimated as the vector between the beam target and the neutrino interaction vertex, and the produced shower, as shown in Figure 8.5 (left). The angle of the neutrino beam can be approximated thus, because the majority of $\bar{\nu}_e$ is produced from kaon decays at the beginning of the pipe.

The difference in the neutrino-shower angular distributions are a combination of the helicity suppression effect described in Section 3.2, where forward going anti-leptons are preferred with no such effect for leptons, and the fact that a population of ν_e from focused meson decays further along the beam pipe can also contribute at higher angles to either ν_e (for a neutrino mode beam) or $\bar{\nu}_e$ (for an antineutrino mode beam). The high-angle contribution of the focused mesons is a result of MicroBooNE being off-axis to the NuMI beam. In an on-axis experiments the direction of the incoming particle is the same regardless of where it was produced in the decay pipe and so this effect would not contribute.

8.2 BDT Result

The BDT model developed in this analysis falls into the category "good classifier" with an AUC= 0.85, as shown in Figure 8.5 (right). The final distribution of the calculated BDT score, as shown in Figure 8.6, does not go up to 1 because the "signal" and "background" have similar behaviours. Therefore, it is not efficient to apply a cut on the BDT variable to separate the sample into ν_e and $\bar{\nu}_e$. Instead, this analysis will use the fact that the distributions have different shapes to perform a template fit to the beam-on BDT distribution.

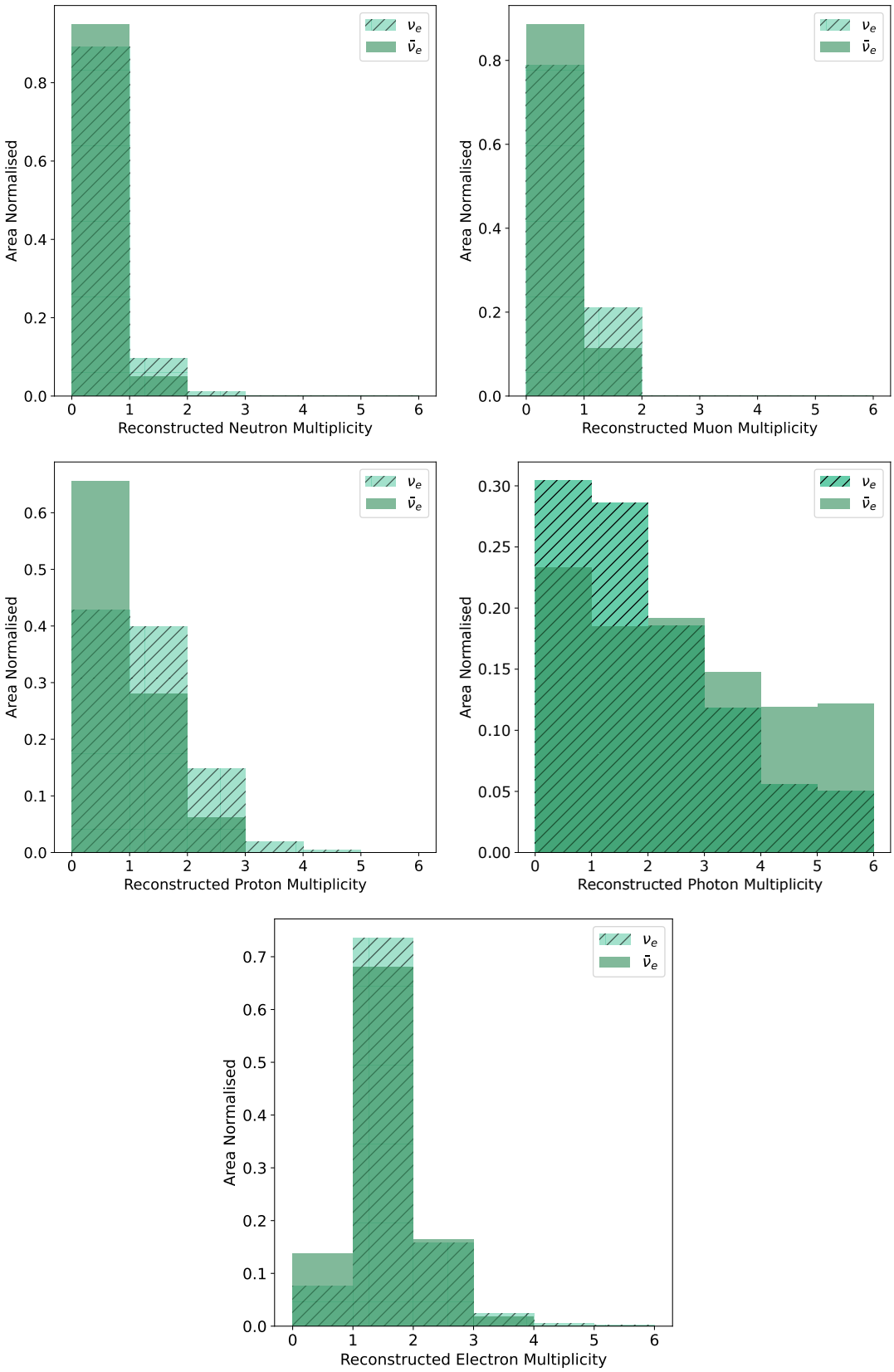

Figure 8.2: Distribution of the reconstructed particle multiplicity for ν_e and $\bar{\nu}_e$ interactions.

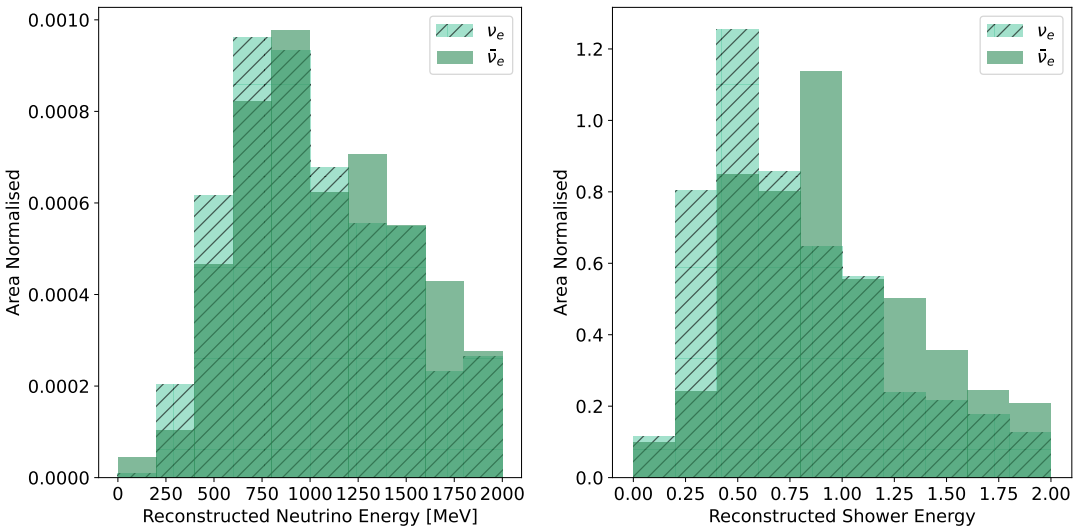

Figure 8.3: Distributions of the reconstructed neutrino energy and reconstructed energy for ν_e and $\bar{\nu}_e$ interactions.

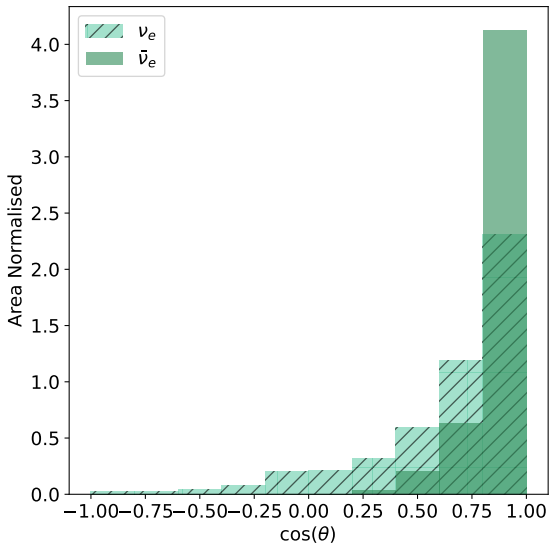

Figure 8.4: Distribution of the angle between the neutrino beam and the produced shower for ν_e and $\bar{\nu}_e$ interactions.

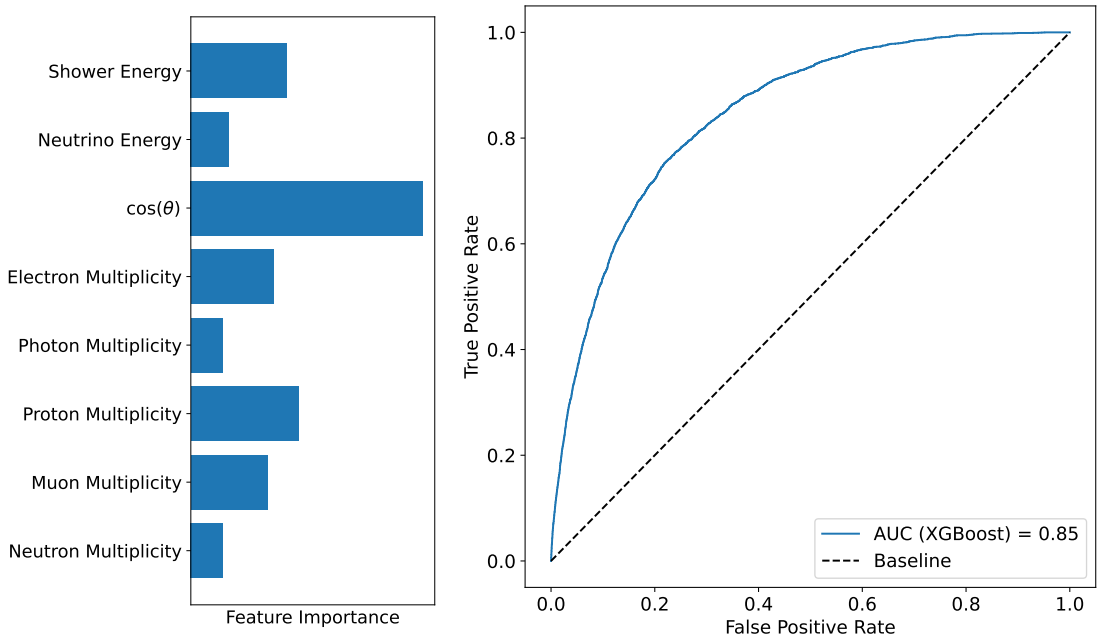

Figure 8.5: Diagram of the feature importance (left) and the Receiver Operating Characteristic (ROC) curve (right) of the BDT model trained in this analysis.

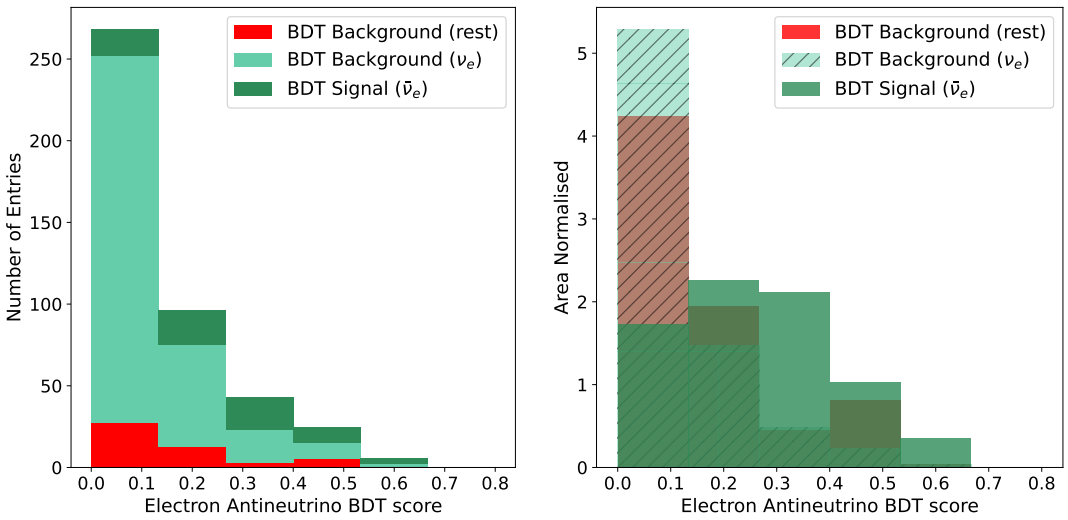

Figure 8.6: BDT score distribution for signal ($\bar{\nu}_e$) and background (split between ν_e and everything else). The area normalised plot (right) shows the different shape of the distributions, whilst the stacked weighted distribution (left) shows the real number of events.

8.3 Post Selection

The neutrino energy spectrum simulated in the MC sample is shown in Figure 8.7. These are ν_eCC and $\bar{\nu}_e$CC events with the interaction vertex inside the fiducial volume. The same plot shows the selection efficiency as a function of the neutrino energy. It is possible to see that the selection efficiency drops to zero at 240 MeV and 520 MeV for ν_e and $\bar{\nu}_e$, respectively. Therefore applying a threshold to remove events with reconstructed neutrino energy below 60 MeV to match the cut applied on the flux, is safely far from the minimum selected neutrino energy in this analysis.

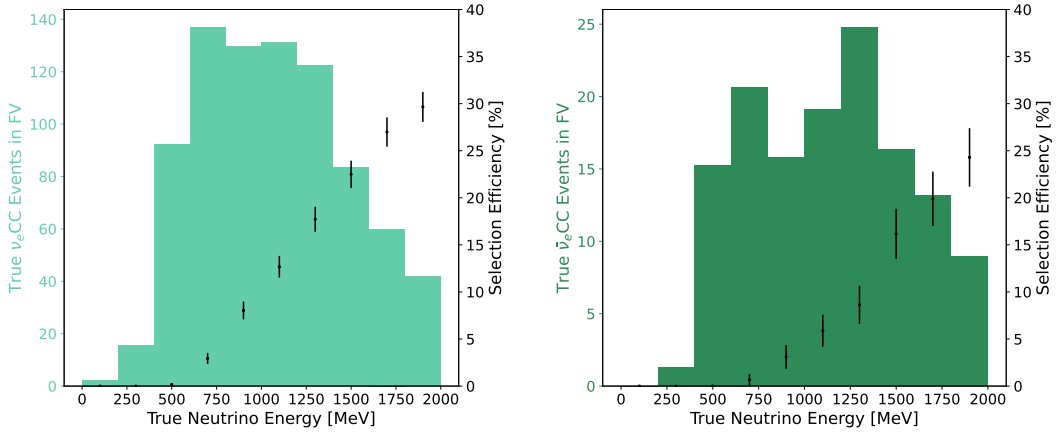

Figure 8.7: Neutrino energy distribution for the selected ν_e (left) and $\bar{\nu}_e$ (right) selected interactions. The selection efficiency plotted on top represents the efficiency in selecting events below a certain energy threshold.

The same exercise can be done by evaluating the simulated and selected shower energy, as shown in Figure 8.8. In this case the selected shower energy has a much lower threshold for $\bar{\nu}_e$ when compared to ν_e, 0.01 GeV and 0.14 GeV respectively. This analysis aims to follow the same procedure to calculate the ν_eCC and $\bar{\nu}_e$CC cross sections to facilitate their comparison. For this reason it was chosen not to apply any cut on the shower energy in the calculation of the number of simulated events.

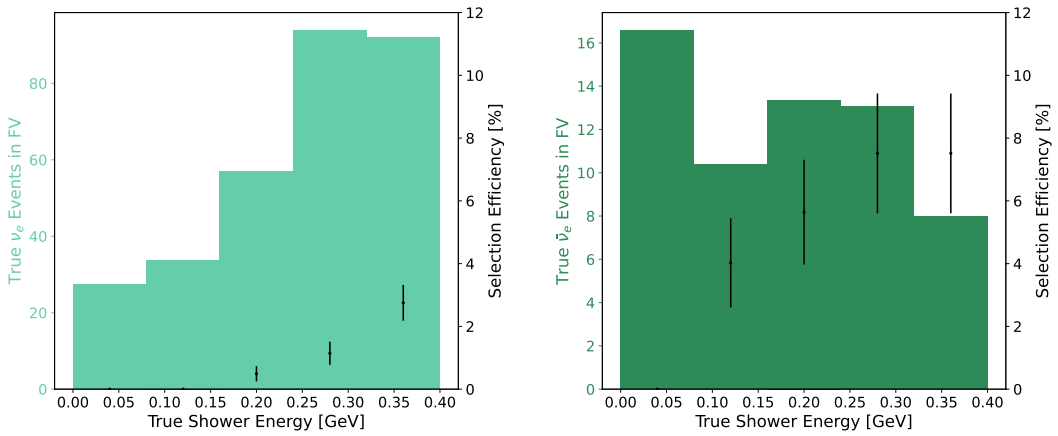

Figure 8.8: Shower energy distribution for the selected ν_e (left) and $\bar{\nu}_e$ (right) selected interactions. The selection efficiency plotted on top represents the efficiency in selecting events below a certain energy threshold. This plot is zoomed-in to lowest energies.

Chapter 9

Measurement of the Electron-Antineutrino and Electron-Neutrino Cross Section

MicroBooNE has been the pioneer experiment in measuring the combined inclusive electron-neutrino and antineutrino cross sections on argon [52, 53]. This analysis takes the next step and performs the first measurement of the *individual* electron neutrino and antineutrino cross sections on argon. This section will describe the procedure used for this measurement.

A cross section measures the probability of a particle to interact with a specific target. Therefore the number of interactions in the detector can be expressed as

$$N_i = \sigma_i \times \phi_i \times N_t, \tag{9.1}$$

where $i = \nu_e$ or $\bar{\nu}_e$, N_i is the number of interactions of this particle inside the detector, σ_i is the particle cross section, ϕ_i is the particle flux at the detector and N_t is the number of targets in the detector. In a scenario where MC simulation perfectly mimics nature, the number of simulated ν_e and $\bar{\nu}_e$ interactions in the detector, N_i^{MC}, should match the number of ν_e and $\bar{\nu}_e$ interactions recorded during the beam exposure, $N_i^{\text{beam-on}}$. But in reality the simulation is not perfect and $N_i^{\text{MC}} \neq N_i^{\text{beam-on}}$. Under the assumption that the discrepancy is primarily due to a wrong normalisation, it can be improved by scaling the MC by S_i. The method used in this analysis

to obtain this scaling term is explained in Section 9.2.1. The scaled equation is

$$N_i^{\text{beam-on}} = S_i \times N_i^{\text{MC}}. \tag{9.2}$$

To be able to count the number of ν_e and $\bar{\nu}_e$ interactions recorded during the beam exposure, the event selection described in Section 7.3 is used and achieves an overall ν_eCC + $\bar{\nu}_e$CC purity of 86.12% with a background contamination mostly consisting of π^0 containing events. Equation 9.2 can then be written as

$$N^{\text{beam-on}} = \left(S_{\nu_e} \times N_{\nu_e}^{\text{MC}}\right) + \left(S_{\bar{\nu}_e} \times N_{\bar{\nu}_e}^{\text{MC}}\right) + \left(S_{\text{bkg}} \times N_{\text{bkg}}^{\text{MC}}\right), \tag{9.3}$$

and the selected number of simulated interactions as

$$N_i^{\text{MC}} = \sigma_i^{\text{GENIE}} \times \phi_i \times \epsilon_i \times N_t, \tag{9.4}$$

where σ_i^{GENIE} is the cross section used in the simulation by GENIE for particle i, ϵ_i is the selection efficiency of a given topology, and each topology of the selected MC sample is scaled by a different number. This analysis is based on the assumption that the scaling correction in Equation 9.3 can be applied to the cross section term, σ_i^{GENIE}, to calculate a new value of the cross section

$$\sigma_i' = S_i \times \sigma_i^{\text{GENIE}}, \tag{9.5}$$

that results in a better agreement between the selected data and MC.

The next sections will describe how to extract the GENIE cross section used in the simulation, and how to calculate the scaling factors.

9.1 Cross Section Calculation

The total flux-averaged cross section is given by the equation

$$< \sigma >= \frac{N - B}{\epsilon \times \phi \times S_{\text{area}} \times \text{POT}_{\text{beam-on}} \times N_T}, \tag{9.6}$$

where N is the number of beam-on events after applying the selection cuts, B is the number of selected MC background events, ϵ is the MC selection efficiency, ϕ is the integrated neutrino flux at MicroBooNE, $\text{POT}_{\text{beam-on}}$ is the beam-on protons

on target (POT), N_T is the number of target nuclei in the fiducial volume, and S_{area} is a term used to correct the neutrino flux to the appropriate fiducial volume. Because beam-on data does not provide true information about the events, it is necessary to use MC information to estimate the number of selected events of a given topology. The idea is that, after applying the selection cuts, a fraction of the number of beam-on events, N, is made of the desired topology (signal), and another fraction is made of background. The number of background events, B, is estimated as the number of events in the selected MC sample not classified as the desired topology. Therefore $N - B$ represents the number of signal events in the selected beam-on data. Simulation also allows to estimate the MC efficiency to select the signal events, so $(N - B)/\epsilon$ should correspond to the number of beam-on signal events before the selection cuts.

The neutrino flux, ϕ, is originally calculated for the full active volume of the detector. However, the number of interactions, N and B, and the number of target nuclei, N_t, are calculated for the fiducial volume, rather than the active volume. In order for the terms in Equation 9.6 to be consistent, a correction term S_{area}, defined as the ratio XY fiducial area (front face of the detector) divided by the XY active area of the detector, is added.

The cross section is a physical quantity whose value should not depend on the number of delivered POT. However, the number of interactions in the detector, $N - B$, is proportional to the delivered POT. The larger the POT, the larger will the number of interactions be in the detector. To compensate for this fact, the flux is also scaled by the delivered POT and, because the neutrino flux is provided as a function of the delivered POT as shown in Table 9.1, the total neutrino flux for a given POT is therefore calculated as $\phi \times \text{POT}_{\text{beam-on}}$.

The procedure to calculate the cross section used in the GENIE simulations is similar to Equation 9.6. The difference is that now the procedure only uses the MC sample, so there is no need to estimate the number of simulated interactions in the detector as $(N - B)/\epsilon$. Instead, the number of simulated interactions is directly provided by the true GENIE information in the MC sample. N_i represents the number of simulated events normalised to the beam-on POT, where i designates the desired topology. Equation 9.6 is then rewritten as

$$< \sigma_i^{\text{GENIE}} >= \frac{N_i}{\phi_i \times S_{\text{area}} \times \text{POT}_{\text{beam-on}} \times N_T}. \tag{9.7}$$

where $(N - B)/\epsilon$ was replaced by N_i, and $< \sigma_i^{\text{GENIE}} >$ is the average cross section calculated in the range specified by energy cuts.

Number of simulated events (N_i)

Following the approach of [53], the number of simulated events was calculated for neutrino energy threshold of at least 60 MeV and whose neutrino vertex was inside the fiducial volume. The expected number of simulated ν_eCC and $\bar{\nu}_e$CC s $\nu_e = 821.76\,(741.43)$ and $\bar{\nu}_e = 190.79\,(159.18)$ interactions, with(without) μB tune, as explained in Section 6.1.2. The neutrino energy threshold and the absence of a threshold on the shower energy are based on the energy distributions for the selected ν_e and $\bar{\nu}_e$, as shown in Section 8.3.

Number of targets (N_T)

It is assumed that the entire volume of the detector is made of argon nuclei that work as interaction targets for the incoming neutrinos. The number of targets in the fiducial volume is given by the equation

$$N_T = \frac{\rho_{\text{Ar}} \times V \times N_A \times N_{\text{Nucleons}}}{m_{\text{mol}}}, \tag{9.8}$$

where $\rho_{\text{Ar}} = 1.3836\,\text{g/cm}^3$ is the liquid argon density, $V = 5.86 \times 10^7\,\text{cm}^3$ is the fiducial volume, $N_A = 6.022 \times 10^{22}\,\text{molecule/mol}$ is Avogadro's Number, $N_{\text{Nucleons}} = 40$ is the number of nucleons per argon nucleus, and $m_{\text{mol}} = 39.95\,\text{g/mol}$ is the number of grams per mole of argon. All together makes a total number of 4.89×10^{31} targets used in this analysis. No assumptions are made regarding how neutrino and antineutrino scatter from proton and neutrons individually.

Flux ($\phi_i \times S_{\text{area}}$) and beam-on POT ($\text{POT}_{\text{beam-on}}$)

The neutrino flux is largely dominated by muon decay neutrinos for energies below 60 MeV, as shown in Figure 6.1, which is extremely difficult to correctly predict and results in neutrino interactions with an energy significantly below the threshold of the reconstruction chain. For this reason the integrated flux in Equation 9.7 only considers neutrino energies above 60 MeV. The individual fluxes, the XY active and fiducial areas and the beam-on POT used in this analysis are listed in Table 9.1.

Parameter	Value
ϕ_{ν_e}	$1.18 \times 10^{-11}\,\mathrm{cm}^{-2}\,\mathrm{POT}^{-1}$
$\phi_{\bar{\nu}_e}$	$6.64 \times 10^{-12}\,\mathrm{cm}^{-2}\,\mathrm{POT}^{-1}$
XY active area	$5.97 \times 10^{4}\,\mathrm{cm}^{3}$
XY fiducial area	$5.68 \times 10^{4}\,\mathrm{cm}^{3}$
S_{area}	0.95
Run 1 FHC NuMI POT	2.01×10^{20} POT

Table 9.1: Parameters related to the flux and beam-on POT used in this analysis.

Summary

Putting the numbers in Equation 9.7, for an average ν_e and $\bar{\nu}_e$ energies of 1195 MeV and 1550 MeV respectively, the expected theoretical GENIE cross section is

$$\sigma_{\nu_e}^{\mathrm{GENIE}} = 7.44 \times 10^{-39}\,\mathrm{cm}^2/\mathrm{nucleon}\,(\mu\mathrm{B\ tune}), \tag{9.9}$$
$$\sigma_{\nu_e}^{\mathrm{GENIE}} = 6.71 \times 10^{-39}\,\mathrm{cm}^2/\mathrm{nucleon}\,(\mathrm{no}\ \mu\mathrm{B\ tune}), \tag{9.10}$$
$$\sigma_{\bar{\nu}_e}^{\mathrm{GENIE}} = 3.07 \times 10^{-39}\,\mathrm{cm}^2/\mathrm{nucleon}\,(\mu\mathrm{B\ tune}), \tag{9.11}$$
$$\sigma_{\bar{\nu}_e}^{\mathrm{GENIE}} = 2.56 \times 10^{-39}\,\mathrm{cm}^2/\mathrm{nucleon}\,(\mathrm{no}\ \mu\mathrm{B\ tune}). \tag{9.12}$$

9.2 Cross Section Calculation using the Template Fit

The scaling terms from Equation 9.3 are calculated in two steps. The first step consists of finding a variable with different distributions for ν_e and $\bar{\nu}_e$, which is achieved with a BDT, as explained in Chapter 8. The second step is to use the BDT distributions to perform a fit to the beam-on distribution, explained in the next section.

9.2.1 Template Fit

The template fit consists of an interactive fitting method that aims to find the appropriate parameters to minimise the difference between the data and model. This analysis uses the MINUIT library [116] to perform the fitting. The method calculates the parameters S_{ν_e}, $S_{\bar{\nu}_e}$, and S_{bkg} from Equation 9.3 that minimises the χ^2 function defined as

$$\chi^2 = \sum_{n}^{\text{bins}} \frac{h_n^{\text{Beam-On}} - (S_{\nu_e} \times h_n^{\nu_e}) - (S_{\bar{\nu}_e} \times h_n^{\bar{\nu}_e}) - \left(S_{\text{bkg}} \times h_n^{\text{bkg}}\right)}{\sqrt{h_n^{\text{Beam-On}}}}, \tag{9.13}$$

where h_n is the number of entries per bin per topology. The equation is normalised by the statistical uncertainty on the number of entries per bin for the beam-on distribution to reduce the weight on the χ^2 calculation of the bins with lower statistics. A single scaling factor is considered for each distribution. The template fit performed in this analysis has 3 degrees of freedom.

The event selection described in Section 7.3 results in 467.51 selected MC events, of which 347.78 are ν_e, 77.75 are $\bar{\nu}_e$, and 41.98 are background. The background portion is made of 27.45 (65%) π^0 events. The full template fit described above with the selected sample was found to return a scaling factor equal to zero for the background subsample. This result does not agree with our expectation and understanding of the background simulation. A possible explanation is that the low statistics of the selected background subsample in addition to its BDT score distribution not being distinctive enough led to this unphysical result.

In order to solve this problem, it was decided to constrain the fitting by performing a simultaneous template fit to the selected sample described above and to an enhanced MC π^0 sample[1]. The usage of an enhanced π^0 sample was chosen because it mimics selected background subsample most closely. The final fitting procedure follows the same steps as described above, but now a simultaneous fit to the enhanced π^0 sample takes place. Which means that the same sf_{bkg} term is used for fitting the π^0-enhanced sample and the selected background sample.

[1]The cuts used to select π^0 events were developed in studies to search for low-energy ν_e excess with WireCell in MicroBooNE [117].

9.2.2 Statistical uncertainty of the template fit

The statistical uncertainty in Equations 9.14 and 9.15 is directly extracted from the fitting procedure and is related to the available statistics in the beam-on dataset. Three tests were performed to validate it:

- **Test 1:** Scale the beam-on distribution by a weight from 1 to 6 and perform the template fit to the not-scaled MC distribution. The result of this test is shown in Figure 9.1. Both the template fit result and the fitting error have a linear growth, which is in accordance with the linear scale of the beam-on distribution only.

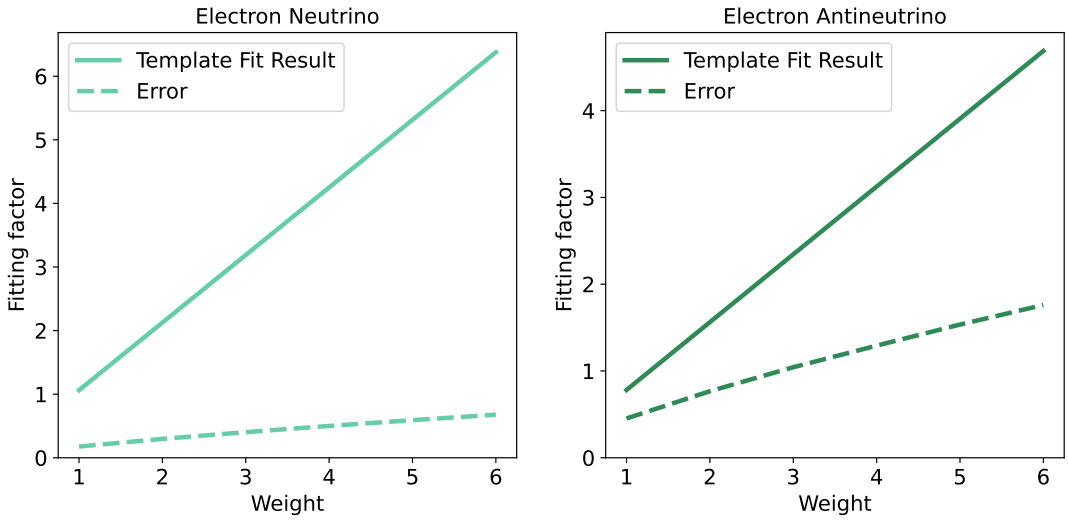

Figure 9.1: Study of the statistical uncertainty with scaling the beam-on distribution by a weight from 1 to 6 whilst keeping the CV MC distribution.

- **Test 2:** Scale both the beam-on and MC distributions by a weight from 1 to 6 and perform the template fit. The result of this test is shown in Figure 9.2. The template fit result remains constant because all distributions are being scaled up by the same factor, and the fitting error decreases when there is more statistics available.

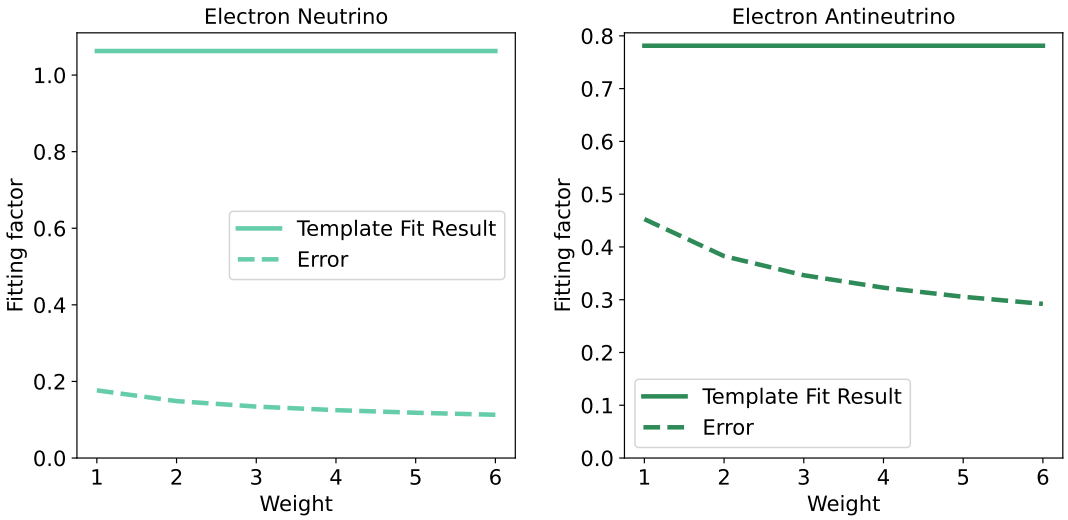

Figure 9.2: Study of the statistical uncertainty with scaling both beam-on and MC distributions by a weight from 1 to 6.

- **Test 3:** Scale the MC distribution by a weight from 1 to 6 and perform the template fit to the not-scaled beam-on distribution. The result of this test is shown in Figure 9.3. Both the template fit result and the fitting error have a behaviour of $1/w$, where w is the applied scaling weight.

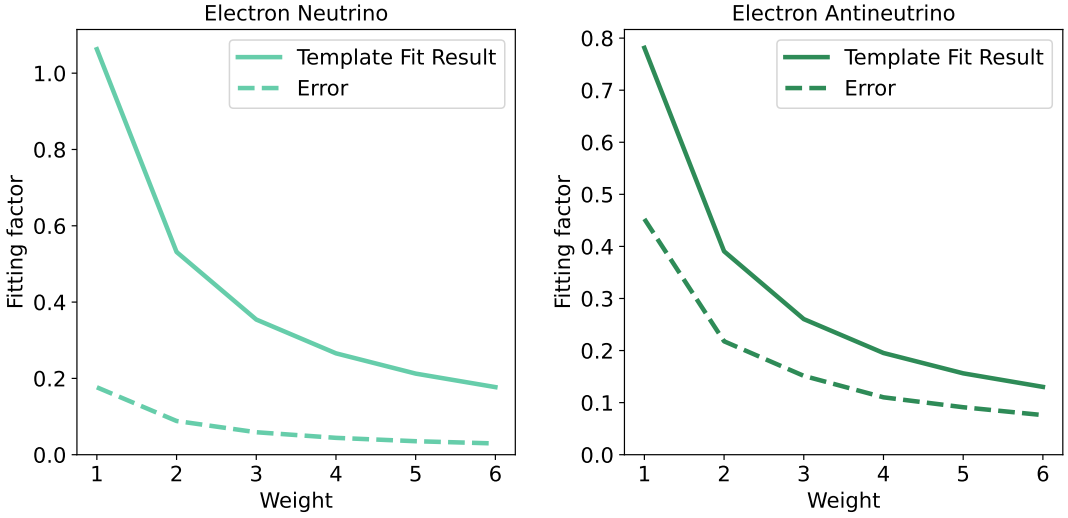

Figure 9.3: Study of the statistical uncertainty with scaling the MC distribution by a weight from 1 to 6 whilst keeping the nominal beam-on distribution.

These tests were performed to evaluate the effect of different sample sizes on the

fitting error. It was shown that a larger MC sample does not affect the fitting error, and that the error is a function of the available statistics of the beam-on distribution. Figure 9.4 shows the percentage error, defined as the ratio between the fitting error divided by the fitting result, for the three tests above. The percentage error decreases as a function of the applied weight only when the beam-on is scaled, and remains constant when the MC sample is scaled alone. Test 3 shows a small fluctuation for the $\bar{\nu}_e$ because of its small statistics.

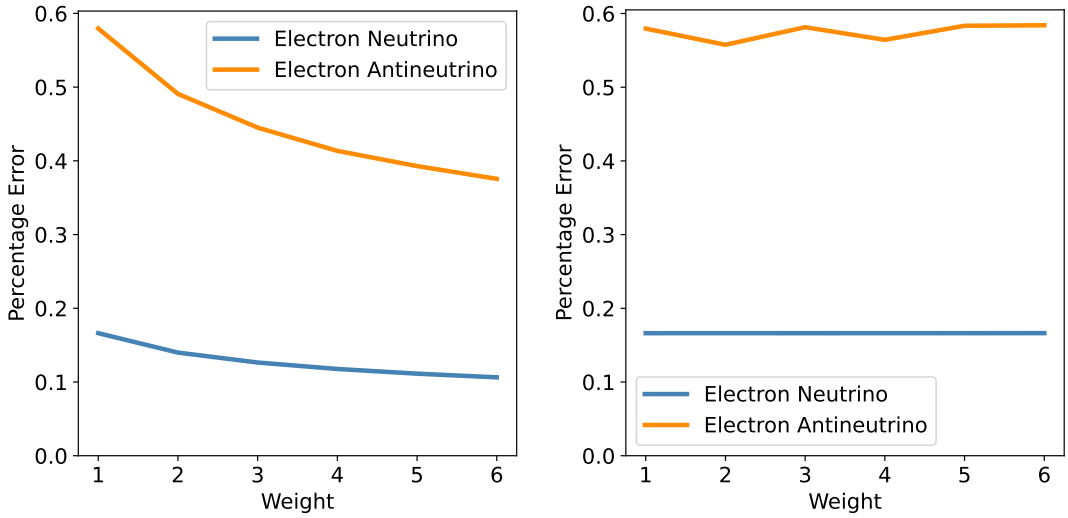

Figure 9.4: Variation of the percentage fitting error as a function of the scaling weight applied to the samples, for tests 1 and 2 (left) and 3 (right).

9.2.3 Template Fit Result

The result of the template fit is

$$\mathrm{sf}_{\nu_e} = 1.06 \pm 0.17 \text{ (stat)} \tag{9.14}$$

$$\mathrm{sf}_{\bar{\nu}_e} = 0.78 \pm 0.45 \text{ (stat)} \tag{9.15}$$

where the statistical uncertainty is provided by MINUIT and is a function of the statistics of the beam-on distribution. Scaling the MC distributions by the result of the fitting increases the agreement with beam-on from $\chi^2 = 4.17$ to $\chi^2 = 3.34$, as shown in Figure 9.5. The calculation of the systematic uncertainty will be described in the next chapter.

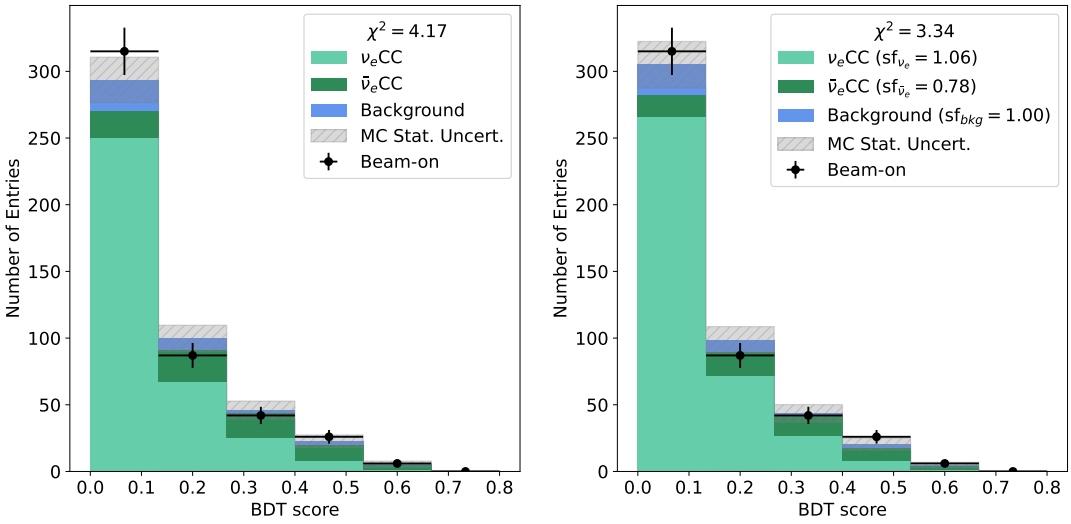

Figure 9.5: Stacked selected MC distribution in comparison to the selected beam-on distribution before (left) and after (right) applying the scaling factors calculated by the template fit.

Chapter 10

Uncertainty Calculation and Final Cross Section Result

The MC sample used to obtain the template fit in Equations 9.14 and 9.15 is a result of the combination of many parameters. These parameters include the physics models, and the beamline components used to generate the MC samples. Varying the nominal value of those parameters can alter the final MC sample and consequently the template fit result. This chapter will describe those variations and their impact on the final result.

10.1 Systematic Uncertainties

The baseline simulation is also known as Central Value (CV) and represents the simulation with nominal values of parameters. The systematic uncertainty calculation then varies the input parameters of the MC simulation and checks how it affects the final result. The present analysis has the following main sources of systematic uncertainties:

- **Flux:** Uncertainties in modelling the hadron production from the proton-target collision, and in modelling the NuMI beamline. Parameters used to constrain the NuMI flux prediction in the PPFX package are resampled to estimate the errors resulting from the chosen nominal values. The parameters related to the thin target assumption are listed in Table 10.1, while the

ones related to the beamline constraints are mostly related to attenuation and absorption effects that might happen from particles crossing elements of the beamline, for instance the horns.

Product	Description
$pC \to \pi X$	Constraints on pion production from pC collisions.
$pC \to KX$	Constraints on kaon production from pC collisions.
$pC \to \text{nucleon}X$	Constraints on proton/nucleon production from pC collisions.
$nC \to \pi X$	Constraints on pion production from nC collisions. These neutrons are produced from the proton-carbon collisions.
$\text{nucleon} - A$	Nucleons interacting in a material that is not Carbon. These are protons or neutrons interacting with other parts of the NuMI setup.
Meson Incident	Mesons that interact on any material in the beamline.

Table 10.1: List of categories of constraints composing the thin target assumption used by PPFX when predicting the neutrino flux, from Ref [63]. The first three lines represent the interactions proton-carbon of the protons coming from the accelerator unit at Fermilab.

- **Cross section:** Uncertainties in modelling the neutrino interactions from the GENIE neutrino generator. In the CV sample, event weights based on interaction properties such as the neutrino energy, final state particles and momentum transfer are saved. The cross section uncertainty is calculated based on reweighing the events after varying those parameters within their uncertainties. The parameter **GENIE All** listed in Table 10.2 comprises a long list of interaction modes detailed in [97].

- **Reinteraction:** Uncertainties in modelling the reinteractions of the neutrino daughter particles in the detector. Protons and pions are the main hadrons produced from neutrino interactions with argon, and they can reinteract as they propagate in the detector. Those reinteractions can affect the reconstruction process and therefore the neutrino identification. These uncertainties are estimated by varying the proton and pion cross sections for scattering on argon.

- **Detector:** Uncertainties in modelling the detector response, the list of parameters is found in Table 10.2. Three groups of parameters are considered in this analysis:

- The **wire modification** measures the difference in the detector response based on modifications to the simulated waveform along the drift direction (WireModX), on the YZ plane due to non-uniformity in the charge response (WireModYZ), and as a function of the orientation of the particle trajectory (WireModThetaXZ and WireModThetaYZ).
- The time-dependent behaviour of the **scintillation light** throughout the MicroBooNE working period is also accounted for by generating new MC samples with specific variations regarding the light. The "light yield down" is a sample generated with 25% reduction in the light yield, to mimic this same reduction observed on data. The "light yield rayleigh" is a sample generated by using a Rayleigh scattering length of 90 cm, instead of 60 cm as in the CV sample. This change is justified because there are many recent measurements showing a Rayleigh scattering length ranging from 60 cm to 100 cm [118, 119, 120, 121].
- Finally, the "space charge effect" and the "recombination" uncertainties account for consequence of the SCE in the amount of electron-ion recombination, and the amount of charge measured by the wires.

Two methods are used to evaluate how variations on the initial parameters affect the simulation. The first one is called **sample re-simulation**. In this method a single initial parameter is varied by $\pm 1\sigma$ with respect to its nominal value, and a full new MC sample is generated and the full analysis chain is applied on the new sample. This method is used to evaluate the detector systematic uncertainty. The second method is called **event re-weighting**. This method re-samples a set of initial parameters within their uncertainties N times, where N is a quantity chosen by and standardised in the MicroBooNE collaboration. The resulting simulation of each variation is called a "universe". In this method, a new event weight is calculated per universe, and applied to the nominal simulation and its existing events. This method is used to evaluate the flux, beamline, cross section and re-interaction systematic uncertainties. A list of the variations and the number of universes for each case is shown in Table 10.2.

During the analysis it was discovered that the "second class vector/axial currents" variations are not available for antineutrinos, which means that it was not possible to evaluate the antineutrino event weight in these cases. The solution adopted in this thesis, only for those two variations, was to assume the CV weight for the

Variation	Type	N_{uni}
Hadron production	Flux (RW)	600
Beamline geometry	Flux (RW)	20
GENIE All	Cross Section (RW)	1000
Strength of RPA correction	Cross Section (RW)	2
Parametrisation of the nucleon axial form factor	Cross Section (RW)	2
Parametrisation of the nucleon vector form factors	Cross Section (RW)	2
Changes angular distribution of nucleon cluster	Cross Section (RW)	2
Changes shape of differential cross section	Cross Section (RW)	2
Interpolates angular distribution for $\Delta \to N + \gamma$	Cross Section (RW)	2
Interpolates angular distribution for $\Delta \to N + \pi$	Cross Section (RW)	2
Scaling factor for CCCOH π production total cross section	Cross Section (RW)	2
Scaling factor for NCCOH π production total cross section	Cross Section (RW)	2
Reweight QE cross section to include second class vector currents*	Cross Section (RW)	10
Reweight QE cross section to include second class axial currents*	Cross Section (RW)	10
Reinteractions of π^+ from the neutrino interaction	Re-interaction (RW)	1000
Reinteractions of π^- from the neutrino interaction	Re-interaction (RW)	1000
Reinteractions of protons from the neutrino interaction	Re-interaction (RW)	1000
Light yield rayleigh	Detector (RS)	2
Light yield down	Detector (RS)	2
Space charge effect	Detector (RS)	2
Recombination	Detector (RS)	2
Wire modification X	Detector (RS)	2
Wire modification YZ	Detector (RS)	2
Wire modification θ_{XZ}	Detector (RS)	2
Wire modification θ_{YZ}	Detector (RS)	2
Wire modification dE/dx	Detector (RS)	2

Table 10.2: List of the systematic variations used in this analysis, specifying if the method used was re-simulation (RS) or re-weighting (RW). The (*) variations are not available for antineutrinos. From Ref. [63].

antineutrino events. The antineutrino Second Class Current (SCC) systematic uncertainty is not zero because the fitting is performed simultaneously to the ν_e, $\bar{\nu}_e$ and "background" distributions. For this reason, even though the antineutrino SCC weights were manually set to match the CV ones, because the ν_e and "background" distributions change, the $\bar{\nu}_e$ calculated scaling term will also change.

10.1.1 Summary

The systematic error calculation is performed by applying the procedure described in Chapter 9 to calculate the CV scaling terms for every systematically shifted universe. Both calculation methods, either sample re-simulation or event re-weighting, will cause the initial set of events present in the CV sample to be slightly modified. The same event selection is applied to each universe, and a new modified BDT score is calculated for each event. The BDT model is only trained once with the CV sample, and is used to calculate the score for each universe. The unique BDT score distribution of the various universes are shown in Figures 10.1-10.4 compared to the CV. Therefore a personalised scaling term is obtained for each universe.

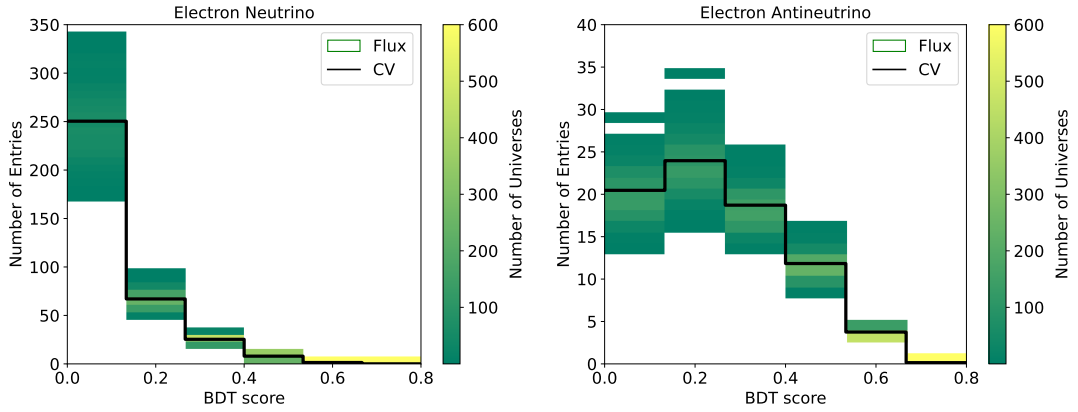

Figure 10.1: Distribution of the BDT score of the various "flux" universes compared to the CV for ν_e (left) and $\bar{\nu}_e$ (right). The colour scheme represents the number of universes per bin, and the black line shows the CV distribution.

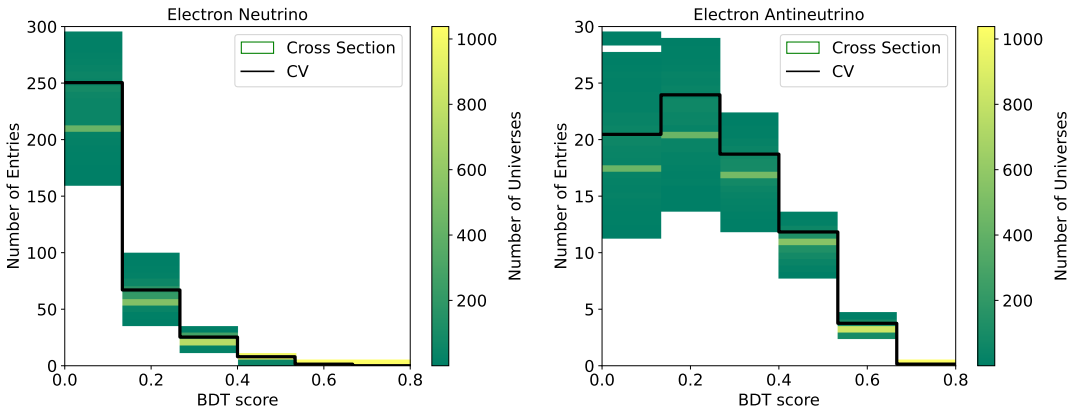

Figure 10.2: Distribution of the BDT score of the various "cross section" universes compared to the CV for ν_e (left) and $\bar{\nu}_e$ (right). The colour scheme represents the number of universes per bin, and the black line shows the CV distribution. The reason why there is a disagreement between the central value and the universe distributions is under study

.

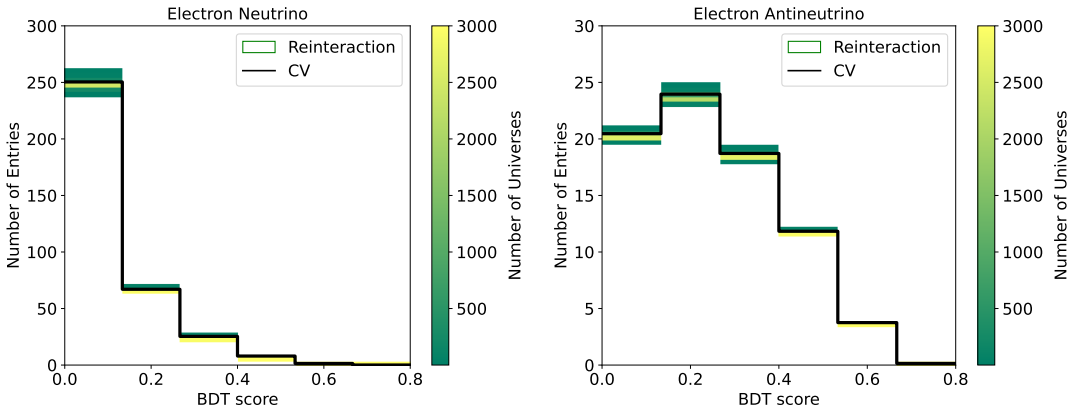

Figure 10.3: Distribution of the BDT score of the various "reinteractions" universes compared to the CV for ν_e (left) and $\bar{\nu}_e$ (right). The colour scheme represents the number of universes per bin, and the black line shows the CV distribution.

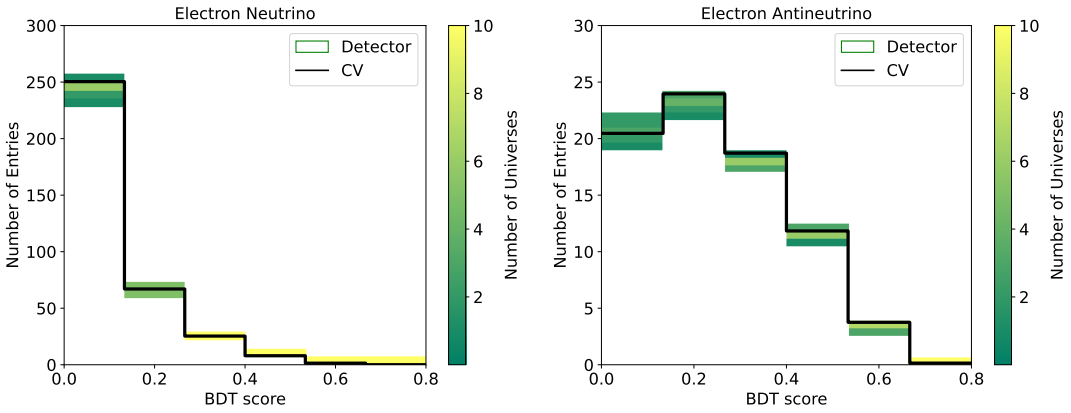

Figure 10.4: Distribution of the BDT score of the various "detector" universes compared to the CV for ν_e (left) and $\bar{\nu}_e$ (right). The colour scheme represents the number of universes per bin, and the black line shows the CV distribution.

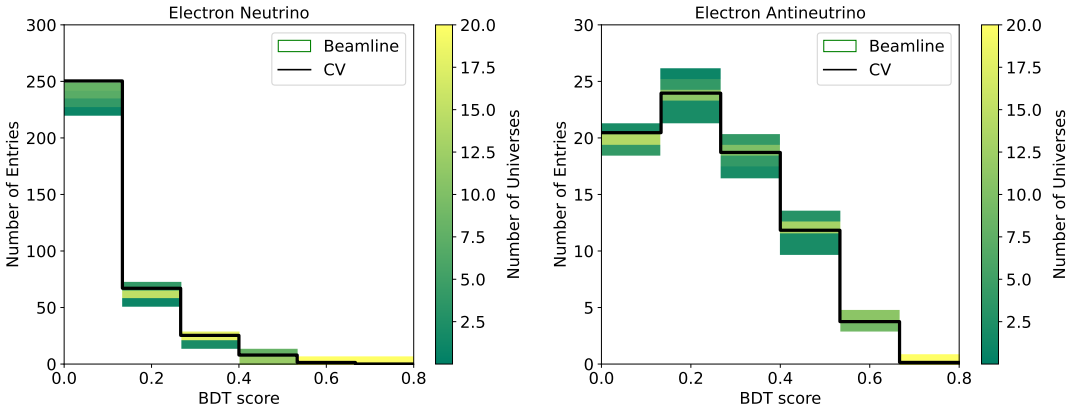

Figure 10.5: Distribution of the BDT score of the various "beamline" universes compared to the CV for ν_e (left) and $\bar{\nu}_e$ (right). The colour scheme represents the number of universes per bin, and the black line shows the CV distribution.

The distributions in Figures 10.1-10.4 show a larger spread with respect to the CV one for the variations related to the flux and cross section. The reason for this is still unknown. The format of this analysis makes it particularly challenging to investigate the cause of specific behaviours in the BDT score distribution, this is mainly because the BDT model considers multiple kinematic variables in a way that it is not straightforward to identify their individual contributions for each universe variation, this study is ongoing.

The systematic uncertainty for each kind of variation is computed through a covariance matrix. After sampling over a number of universes N the covariance matrix elements for each kind of variation, q, are calculated as

$$M_{ij}^{q} = \frac{1}{N}\sum_{k}^{N}\left(S_{i}^{q,k} - S_{i}^{q,\mathrm{CV}}\right)\left(S_{j}^{q,\,k} - S_{j}^{q,\mathrm{CV}}\right), \tag{10.1}$$

where q is the type of variation ($q =$ "hadron production", "beamline geometry" and so on), S^{k} is the scaling term obtained for universe variation k, i and j can be 0 or 1 representing the matrix index. The full covariance matrix per variation q is

$$M^{q} = \begin{bmatrix} M^{q}_{\nu_e,\nu_e} & M^{q}_{\nu_e,\bar{\nu}_e} \\ M^{q}_{\bar{\nu}_e,\nu_e} & M^{q}_{\bar{\nu}_e,\bar{\nu}_e} \end{bmatrix}, \tag{10.2}$$

and the systematic uncertainty is calculated as the square root of the individual terms of the main diagonal, $\sigma^{q}_{\nu_e} = \sqrt{M^{q}_{\nu_e,\nu_e}}$ and $\sigma^{q}_{\bar{\nu}_e} = \sqrt{M^{q}_{\bar{\nu}_e,\bar{\nu}_e}}$. No bin-bin correlation was considered in this analysis. This analysis only uses neutrino-mode data (FHC) and for this reason no antineutrino-mode data (RHC) is considered. Figure 10.6 shows the fractional uncertainty of the scaling terms per variation used in this analysis, and Figure 10.7 shows the fractional uncertainty of the scaling terms per variation type (for instance "flux", "beamline" and so on).

To be able to calculate the full systematic uncertainty, it is necessary to first calculate the full covariance matrix as the sum of the individual ones, $M^{\mathrm{total}} = \sum M^{q}$. The total systematic uncertainty on the scaling terms is then computed as $\sigma^{\mathrm{total}}_{\nu_e} = \sqrt{M^{\mathrm{total}}_{11}}$ and $\sigma^{\mathrm{total}}_{\bar{\nu}_e} = \sqrt{M^{\mathrm{total}}_{22}}$. Putting everything together, the final scaling term

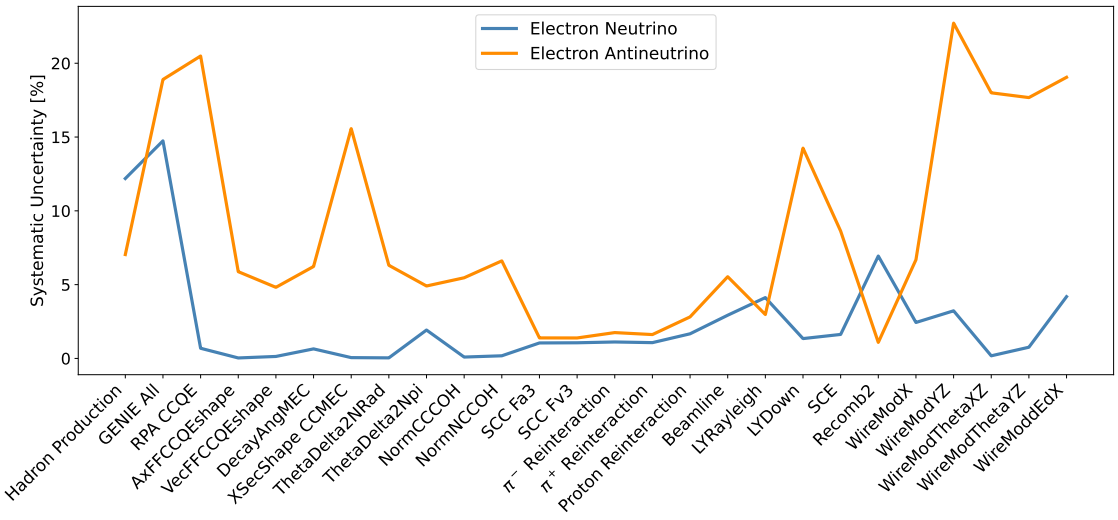

Figure 10.6: Percentile systematic uncertainty per variation used in this analysis. This plot is in "scaling term" units.

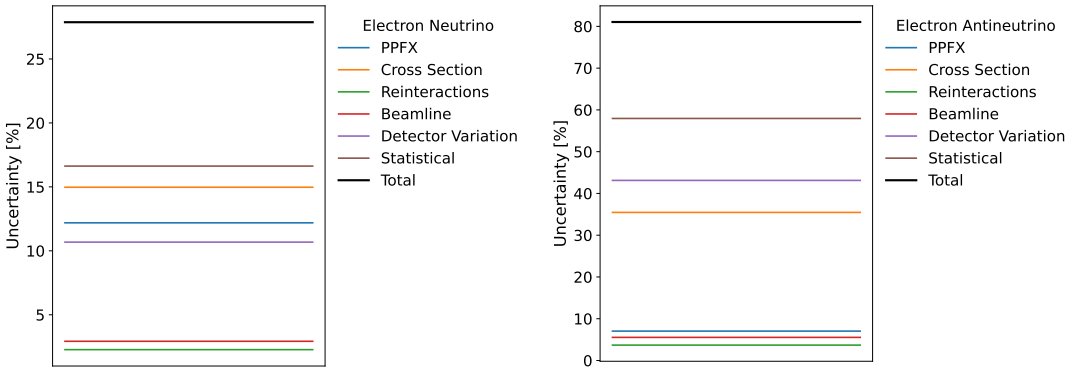

Figure 10.7: Systematic uncertainty contribution per variation type.

with statistical and systematic uncertainties is

$$S_{\nu_e} = 1.06 \pm 0.17\ (\text{stat}) \pm 0.24\ (\text{sys}) \tag{10.3}$$

$$S_{\bar{\nu}_e} = 0.78 \pm 0.45\ (\text{stat}) \pm 0.44\ (\text{sys}). \tag{10.4}$$

10.2 Cross Section Result

The goal of this analysis is to calculate the individual "corrected" ν_e and $\bar{\nu}_e$ cross sections that generates a better agreement with the beam-on recorded data. This cross section is calculated via Equation 9.5, and by combining the calculated GENIE

cross section (Equations 9.9-9.12), and the scaling terms with full statistical and systematic uncertainties (Equations 10.3-10.4), the final result is:

$$\sigma_{\nu_e} = [7.91 \pm 1.31\ (\text{stat}) \pm 1.77\ (\text{sys})] \times 10^{-39}\text{cm}^2/\text{nucleon} \tag{10.5}$$

$$\sigma_{\bar{\nu}_e} = [2.40 \pm 1.39\ (\text{stat}) \pm 1.36\ (\text{sys})] \times 10^{-39}\text{cm}^2/\text{nucleon} \tag{10.6}$$

for an average ν_e of 1195 MeV and $\bar{\nu}_e$ energy of 1550 MeV. The graphic representation of the cross sections is shown on Figure 10.8. The neutrino energy distribution after scaling the ν_e and $\bar{\nu}_e$ categories is shown in Figure 10.9. It is the first time the $\bar{\nu}_e$ cross section on argon has been calculated.

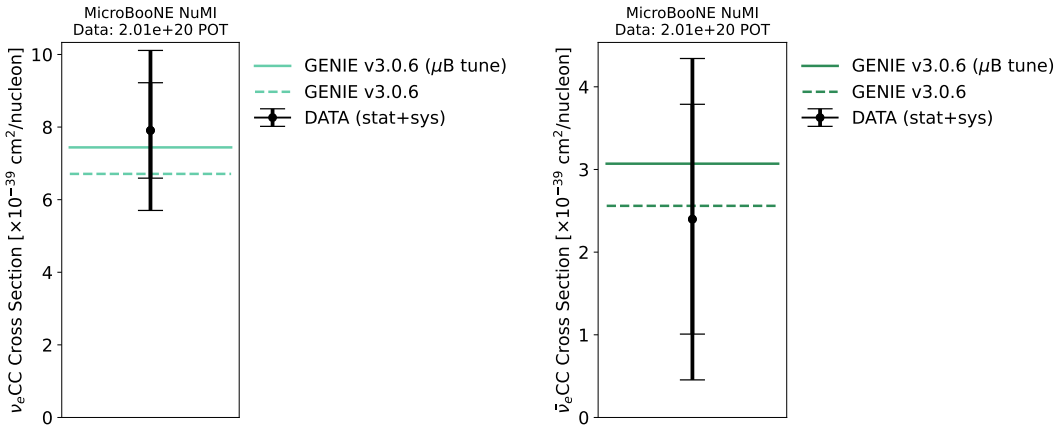

Figure 10.8: Comparison between the GENIE v3.0.6 cross section with and without tune, and the corrected cross section calculated in this analysis.

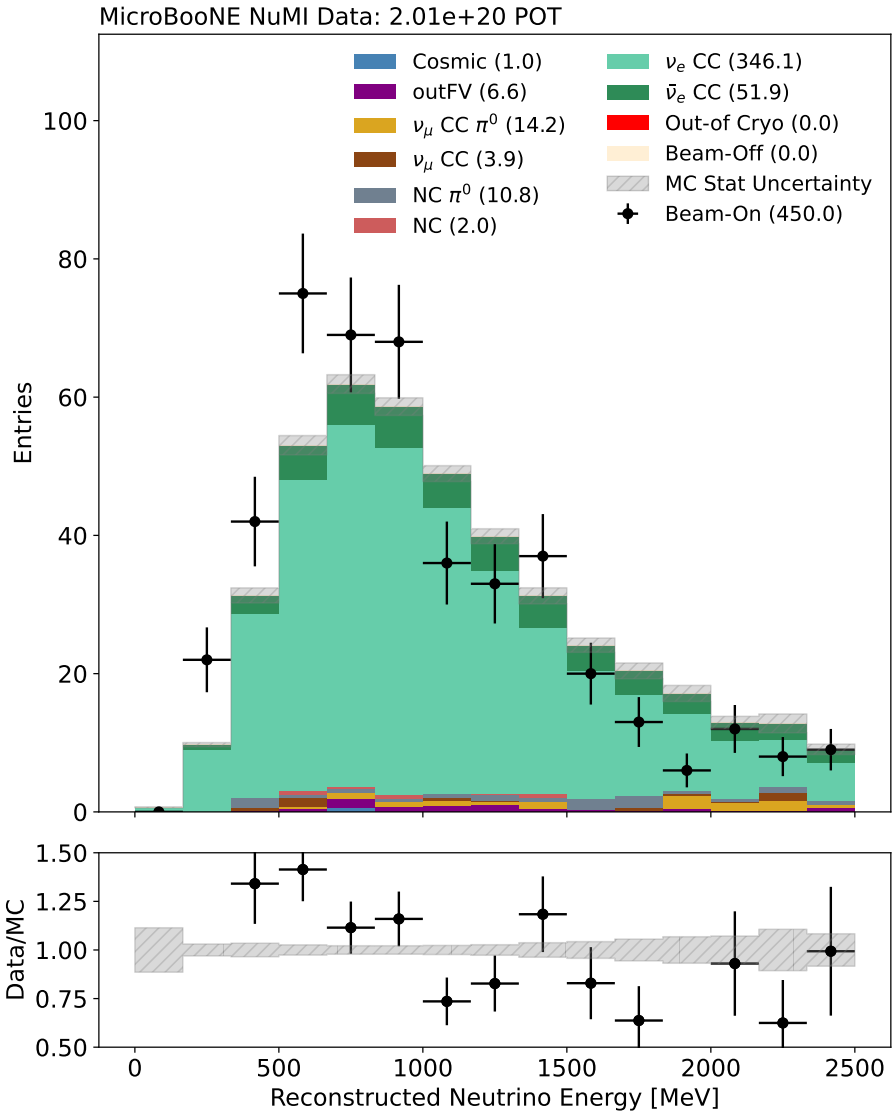

Figure 10.9: Neutrino energy distribution at the end of the selection chain after normalising the ν_e and $\bar{\nu}_e$ categories by their calculated scaling terms of 1.06 and 0.78 respectively.

Chapter 11

Conclusion

This thesis presents the first measurement of the individual electron-neutrino cross section on argon using the NuMI beam at MicroBooNE, and the first ever measurement of the electron-antineutrino cross section on argon. Understanding the precise neutrino cross section is a key step on the path to unravelling open questions in particle physics that can be answered by observing ν_e appearance from oscillation, such as why we live in a matter-dominated universe.

MicroBooNE is a LArTPC, which is a technology that provides one of the best opportunities to measure neutrino interactions nowadays. It, however, does not have the power to distinguish between particle and its antiparticle due to the absence of a magnetic field. For this reason, MicroBooNE has only published $\nu_e + \bar{\nu}_e$ cross-section measurements to date. The only individual ν_e measurement was performed on a pure ν_e beam. This thesis presents the result of the first simultaneous measurement of both the ν_eCC and $\bar{\nu}_e$CC cross sections on argon using the data from the NuMI beam at the MicroBooNE detector. It is the first ever measurement of the $\bar{\nu}_e$CC cross section on argon.

The dataset used in this analysis is the full NuMI Run 1 collected by MicroBooNE, that comprises 2.01×10^{20} POT. The collected data was then processed by the Wire-Cell framework and subjected to a set of selection cuts developed to select $\nu_e + \bar{\nu}_e$ interactions with an efficiency of 50%. A total of 476 $\nu_e + \bar{\nu}_e$ candidates are selected, which is the largest sample in a LArTPC to date.

The novelty of this analysis in comparison to the other three electron neutrino

cross-section measurements published by MicroBooNE is the development of a technique to distinguish ν_e from $\bar{\nu}_e$ interactions, which was believed to be impossible with a LArTPC. This technique is a XGBoost BDT model that exploits the fact that MicroBooNE is off-axis to the NuMI beam. Among the chosen variables, the angle between the produced shower and the vector between the NuMI target and the neutrino interaction vertex is the one with the highest importance feature.

The kinematic variables chosen to train the BDT model, however, do not show enough separation power to result in a BDT score distribution such to enable a cut to separate the selected ν_eCC from the selected $\bar{\nu}_e$CC . For this reason, in addition to calculating a BDT score, a template fit was performed to find the numerical scaling factor that normalises the selected MC in a way to minimise the χ^2 to the selected data, with the result $\text{sf}_{\nu_e} = 1.06 \pm 0.17(\text{stat}) \pm 0.24(\text{sys})$ and $\text{sf}_{\bar{\nu}_e} = 0.78 \pm 0.45(\text{stat}) \pm 0.44(\text{sys})$. Because the number of interactions is proportional to the cross section, this thesis assumes that the scaling factor found via the template fit can be used to scale the GENIE cross section used in the analysis to a value that represents the true value of the cross section.

The result of this thesis is a cross section of $\sigma_{\nu_e} = [7.91 \pm 1.31\ (\text{stat}) \pm 1.77\ (\text{sys})] \times 10^{-39}\,\text{cm}^2/\text{nucleon}$ and $\sigma_{\bar{\nu}_e} = [2.40 \pm 1.39\ (\text{stat}) \pm 1.36\ (\text{sys})] \times 10^{-39}\,\text{cm}^2/\text{nucleon}$ suggesting an overprediction of the $\bar{\nu}_e$ cross section by GENIE, for an average energy of 1195 MeV for ν_e and 1550 MeV for $\bar{\nu}_e$. This is also the first measurement of $\bar{\nu}_e$ cross section on argon.

11.1 Future Work

For being a new kind of analysis in the field, many new challenges were faced and the solutions adopted can still be improved. Here is a list of future steps for this analysis:

- Accelerator electron-neutrino analyses are famous for having low statistics, since ν_e are in reality a background in a designed ν_μ beam. Using the NuMI beam has been a conscious decision to enlarge the available ν_e statistics thanks to it being a more energetic beam. However, this analysis only uses the MicroBooNE Run 1 data, so including the rest of the available Runs can help reduce the statistical uncertainty of the analysis.

- The NuMI beam has operated in two different neutrino modes (FHC and RHC), as explained in Section 5.2. FHC mode generates a neutrino-enhanced beam whilst RHC generated an antineutrino-enhanced beam. For this reason, performing this analysis with the full MicroBooNE dataset will likely contribute to constrain the template fit.

- Electron neutrinos and antineutrinos have very similar signatures in LArTPC detectors, and for this reason differentiating them were thought to be impossible with this kind of technology. This analysis has shown that ν_e and $\bar{\nu}_e$ can have different behaviours for a few kinematic properties. Even though the differences are subtle, it was enough to obtain a BDT model that results in a BDT score distribution different for those topologies. During the course of my PhD I have tested many variables that did not contribute to the performance of the BDT model and, therefore, were removed from the analysis. However, exploring further the potential of this BDT model by testing new variables could further improve the separation power of this tool for this analysis.

- The systematic errors, especially for $\bar{\nu}_e$, seem artificially high and a dedicated study to understand whether this is not some accidental problem is needed and ongoing.

Appendix A

Other Projects

Other than the material presented in this thesis, I have also been involved in other projects during my PhD. The first one regards the simulation for the SBND experiment, a LArTPC located at Fermilab. During this project, I was responsible, alongside Gustavo Valdiviesso and Marco del Tutto, for rewriting the entire geometry used in the simulation of the SBND detector. The new geometry uses the Geometry Description Markup Language (GDML) and is the most accurate SBND has ever had. It accounts for precise dimensions and positions of all the elements in the detector. This improvement is crucial for SBND to perform precise neutrino oscillation measurements.

At the beginning of my PhD I learned how to develop a cross section measurement using MicroBooNE data by helping Krishan Mistry finalise his analysis [52]. During this period I got involved in the production of the necessary simulation samples for the systematic uncertainties and in writing the code he used for calculating them. During this process I acquired the knowledge on how to run simulations and how to calculate systematic uncertainties, which were crucial for developing my own analysis later on.

The framework developed for Krishan's analysis focused on selecting electron neutrinos and antineutrinos. Since I was familiar with it, I was asked to adapt his code to perform a π^0 selection instead and to increase the statistics by including more MicroBooNE data. The result was the missing piece for the studies on how to calculate detector-related uncertainties in a completely new way with MicroBooNE [122].

My analysis was developed using a new reconstruction framework called Wire-Cell. This framework was showing a good selection efficiency for ν_e and $\bar{\nu}_e$ interactions, which is a really attractive feature for electron neutrino analysis. The process of changing the reconstruction framework from Pandora (used by Krishan) to Wire-Cell involved re-learning how to develop a cross-section measurement using new variables, and also working with a new working group.

By the time I was starting to deal with the systematic uncertainties of my analysis, Fermilab changed the priority experiments had to access their data. During this period the priority assigned to MicroBooNE decreased by a lot and all data/simulation processing were delayed by almost two months. MicroBooNE has a group of people dedicated to run simulation upon request from the analysers. However the requests had accumulated after this period and I was unable to have my samples produced by this group, and had to process all the necessary samples for my analysis myself. Wire-Cell had just began to use NuMI data and for this reason, processing my simulations also involved debugging problems related to switching to NuMI, instead of using the BNB as traditionally in MicroBooNE.

The systematic uncertainty studies require many samples, so I developed a tracking tool to track the status of production and to organise the information regarding each sample. Later on, I adapted this tool to work for many production campaigns and it is now used by the MicroBooNE production team.

My PhD has been affected by the COVID-19 pandemic. I have spent close to 2 years working from home in Brazil. In addition, Fermilab was closed for many months, which comprises the period I was supposed to go there under the approved Universities Research Association (URA) Visiting Scholarship Program.

Bibliography

[1] S.M. Bilenky and J. Hošek. "Glashow-Weinberg-Salam theory of electroweak interactions and the neutral currents". In: *Physics Reports* 90.2 (1982), pp. 73–157. ISSN: 0370-1573. DOI: https://doi.org/10.1016/0370-1573(82)90016-3.

[2] Don Lincoln. "The Standard Model: The most successful theory ever". In: Fermilab Today, 2011. URL: https://www.fnal.gov/pub/today/archive/archive_2011/today11-11-18_NutshellStandardModelReadMore.html.

[3] "CKM Quark-Mixing Matrix". URL: https://pdg.lbl.gov/2019/reviews/rpp2019-rev-ckm-matrix.pdf.

[4] M. Kleesiek et al. "β-Decay spectrum, response function and statistical model for neutrino mass measurements with the KATRIN experiment". In: *The European Physical Journal C* (2019). DOI: 10.1140/epjc/s10052-019-6686-7.

[5] Wolfgang Pauli. "Pauli letter collection: letter to Lise Meitner". URL: https://cds.cern.ch/record/83282.

[6] J. Chadwick. "Possible Existence of a Neutron". In: *Nature* 129.312 (Feb. 1932). DOI: 10.1038/129312a0.

[7] F. Reines and C. L. Cowan. "Detection of the Free Neutrino". In: *Phys. Rev.* 92 (3 Nov. 1953), pp. 830–831. DOI: 10.1103/PhysRev.92.830.

[8] E. J. Konopinski and H. M. Mahmoud. "The Universal Fermi Interaction". In: *Phys. Rev.* 92 (4 Nov. 1953), pp. 1045–1049. DOI: 10.1103/PhysRev.92.1045.

[9] K. Kodama et al. "Observation of tau neutrino interactions". In: *Physics Letters B* 504.3 (2001), pp. 218–224. ISSN: 0370-2693. DOI: https://doi.org/10.1016/S0370-2693(01)00307-0.

[10] Luigi Di Lella and Carlo Rubbia. "The Discovery of the W and Z Particles". In: *Adv. Ser. Direct. High Energy Phys.* 23 (2015), pp. 137–163. DOI: 10.1142/9789814644150_0006.

[11] Alain Blondel. *The third family of neutrinos*. 2019. arXiv: 1812.11362.

[12] S Turck-Chièze. "The Standard Solar Model and beyond". In: *Journal of Physics: Conference Series* 665.1 (Jan. 2016), p. 012078. DOI: 10.1088/1742-6596/665/1/012078.

[13] Arnon Dar. *Solar Neutrinos and The Standard Solar Model*. 1997. arXiv: astro-ph/9707015 [astro-ph].

[14] John N. Bahcall. "Solar Neutrinos. I. Theoretical". In: *Phys. Rev. Lett.* 12 (11 Mar. 1964), pp. 300–302. DOI: 10.1103/PhysRevLett.12.300.

[15] Raymond Davis. "A review of the homestake solar neutrino experiment". In: *Progress in Particle and Nuclear Physics* 32 (1994), pp. 13–32. ISSN: 0146-6410. DOI: https://doi.org/10.1016/0146-6410(94)90004-3.

[16] B. Pontecorvo. "Mesonium and anti-mesonium". In: *Sov. Phys. JETP* 6 (1957), p. 429.

[17] B. Pontecorvo. "Inverse beta processes and nonconservation of lepton charge". In: *Zh. Eksp. Teor. Fiz.* 34 (1957), p. 247.

[18] A. Bellerive et al. "The Sudbury Neutrino Observatory". In: *Nuclear Physics B* 908 (2016). Neutrino Oscillations: Celebrating the Nobel Prize in Physics 2015, pp. 30–51. ISSN: 0550-3213. DOI: https://doi.org/10.1016/j.nuclphysb.2016.04.035.

[19] Ziro Maki, Masami Nakagawa, and Shoichi Sakata. "Remarks on the unified model of elementary particles". In: *Prog. Theor. Phys.* 28 (1962), pp. 870–880. DOI: 10.1143/PTP.28.870.

[20] R.L. Workman *et al.* "Particle Data Group - Neutrino Masses, Mixing, and Oscillations". In: Prog. Theor. Exp. Phys., 2022. URL: https://pdg.lbl.gov/2022/reviews/rpp2022-rev-neutrino-mixing.pdf.

[21] B. Abi et al. *Deep Underground Neutrino Experiment (DUNE), Far Detector Technical Design Report, Volume II: DUNE Physics*. 2020. arXiv: 2002.03005 [hep-ex].

[22] R. Acciarri et al. *A Proposal for a Three Detector Short-Baseline Neutrino Oscillation Program in the Fermilab Booster Neutrino Beam*. 2015. arXiv: 1503.01520 [physics.ins-det].

[23] T. Araki et al. "Measurement of Neutrino Oscillation with KamLAND: Evidence of Spectral Distortion". In: *Physical Review Letters* 94.8 (Mar. 2005). DOI: 10.1103/physrevlett.94.081801.

[24] I. Ambats et al. "The MINOS Detectors Technical Design Report". In: (Oct. 1998). DOI: 10.2172/1861363.

[25] K. Abe et al. "The T2K experiment". In: *Nuclear Instruments and Methods in Physics Research Section A: Accelerators, Spectrometers, Detectors and Associated Equipment* 659.1 (2011), pp. 106–135. ISSN: 0168-9002. DOI: https://doi.org/10.1016/j.nima.2011.06.067.

[26] D. S. Ayres et al. "The NOvA Technical Design Report". In: (Oct. 2007). DOI: 10.2172/935497.

[27] A. Gando et al. "Reactor on-off antineutrino measurement with KamLAND". In: *Phys. Rev. D* 88 (3 Aug. 2013), p. 033001. DOI: 10.1103/PhysRevD.88.033001.

[28] "Neutrino Masses, Mixing, and Oscillations". URL: https://pdg.lbl.gov/2023/reviews/rpp2022-rev-neutrino-mixing.pdf.

[29] Sacha Davidson, Enrico Nardi, and Yosef Nir. "Leptogenesis". In: *Physics Reports* 466.4 (2008), pp. 105–177. ISSN: 0370-1573. DOI: https://doi.org/10.1016/j.physrep.2008.06.002.

[30] "SuperNEMO experiment". URL: https://supernemo.org/.

[31] E.Kh. Akhmedov, G.C. Branco, and M.N. Rebelo. "Seesaw mechanism and structure of neutrino mass matrix". In: *Physics Letters B* 478.1-3 (Apr. 2000), pp. 215–223. DOI: 10.1016/s0370-2693(00)00282-3.

[32] A. Yu. Smirnov. *The MSW effect and Solar Neutrinos*. 2003. arXiv: hep-ph/0305106 [hep-ph].

[33] V. Barger et al. "Matter effects on three-neutrino oscillations". In: *Phys. Rev. D* 22 (11 Dec. 1980), pp. 2718–2726. DOI: 10.1103/PhysRevD.22.2718.

[34] A. Aguilar et al. "Evidence for neutrino oscillations from the observation of $\bar{\nu}_e$ appearance in a $\bar{\nu}_e$ beam". In: *Phys. Rev. D* 64 (11 Nov. 2001), p. 112007. DOI: 10.1103/PhysRevD.64.112007.

[35] A.A. Aguilar-Arevalo et al. "The MiniBooNE detector". In: *Nuclear Instruments and Methods in Physics Research Section A: Accelerators, Spectrometers, Detectors and Associated Equipment* 599.1 (Feb. 2009), pp. 28–46. DOI: 10.1016/j.nima.2008.10.028.

[36] A. A. Aguilar-Arevalo et al. "Updated MiniBooNE neutrino oscillation results with increased data and new background studies". In: *Phys. Rev. D* 103 (5 Mar. 2021), p. 052002. DOI: 10.1103/PhysRevD.103.052002.

[37] "The MiniBooNE experiment". URL: https://www.slac.stanford.edu/econf/C060717/papers/T012.PDF.

[38] S. Amerio et al. "Design, construction and tests of the ICARUS T600 detector". In: *Nucl. Instrum. Meth. A* 527 (2004), pp. 329–410. DOI: 10.1016/j.nima.2004.02.044.

[39] Mark Thomson. "Modern Particle Physics". In: Cambridge University Press, 2013. DOI: 10.1007/0-306-47094-2_4.

[40] J. A. Formaggio and G. P. Zeller. "From eV to EeV: Neutrino cross sections across energy scales". In: *Reviews of Modern Physics* 84.3 (Sept. 2012), pp. 1307–1341. DOI: 10.1103/revmodphys.84.1307.

[41] Omar Benhar et al. "Electron- and neutrino-nucleus scattering in the impulse approximation regime". In: *Phys. Rev. D* 72 (5 Sept. 2005), p. 053005. DOI: 10.1103/PhysRevD.72.053005.

[42] D. Rohe et al. "Correlated Strength in the Nuclear Spectral Function". In: *Phys. Rev. Lett.* 93 (18 Oct. 2004), p. 182501. DOI: 10.1103/PhysRevLett.93.182501.

[43] J. Nieves, I. Ruiz Simo, and M. J. Vicente Vacas. "Inclusive charged-current neutrino-nucleus reactions". In: *Phys. Rev. C* 83 (4 Apr. 2011), p. 045501. DOI: 10.1103/PhysRevC.83.045501.

[44] Lars Hans Bathe-Peters. "Studies of Single-Transverse Kinematic Variables for Neutrino Interactions on Argon". In: (Jan. 2020). URL: https://www.osti.gov/biblio/1661674.

[45] Kevin McFarland. *Neutrino Interactions*. 2008. arXiv: 0804.3899 [hep-ex].

[46] T. Eichten et al. "High energy electronic neutrino (ν_e) and antineutrino ($\bar{\nu}_e$) interactions". In: *Physics Letters B* 46.2 (1973), pp. 281–284. ISSN: 0370-2693. DOI: https://doi.org/10.1016/0370-2693(73)90703-X.

[47] J. Blietschau et al. "Total cross sections for ν_e and interactions and search for neutrino oscillations and decay". In: *Nuclear Physics B* (Feb. 1978). DOI: 10.1016/0550-3213(78)90299-7.

[48] K. Abe et al. "Measurement of the Inclusive Electron Neutrino Charged Current Cross Section on Carbon with the T2K Near Detector". In: *Phys. Rev. Lett.* 113 (24 Dec. 2014), p. 241803. DOI: 10.1103/PhysRevLett.113.241803.

[49] and K. Abe et al. "Measurement of the charged-current electron (anti-)neutrino inclusive cross-sections at the T2K off-axis near detector ND280". In: *Journal of High Energy Physics* 2020.10 (Aug. 2020). DOI: 10.1007/jhep10(2020)114.

[50] J. Wolcott et al. "Measurement of Electron Neutrino Quasielastic and Quasielasticlike Scattering on Hydrocarbon at $< E_\nu >= 3.6\,\text{GeV}$". In: *Phys. Rev. Lett.* 116 (8 Feb. 2016), p. 081802. DOI: 10.1103/PhysRevLett.116.081802.

[51] R. Acciarri et al. "First measurement of electron neutrino scattering cross section on argon". In: *Phys. Rev. D* 102 (1 July 2020), p. 011101. DOI: 10.1103/PhysRevD.102.011101.

[52] P. Abratenko et al. "Measurement of the flux-averaged inclusive charged-current electron neutrino and antineutrino cross section on argon using the NuMI beam and the MicroBooNE detector". In: *Phys. Rev. D* 104 (5 Sept. 2021), p. 052002. DOI: 10.1103/PhysRevD.104.052002.

[53] P. Abratenko et al. "First measurement of inclusive electron-neutrino and antineutrino charged current differential cross sections in charged lepton energy on argon in MicroBooNE". In: *Phys. Rev. D* 105 (5 Mar. 2022), p. L051102. DOI: 10.1103/PhysRevD.105.L051102. URL: https://link.aps.org/doi/10.1103/PhysRevD.105.L051102.

[54] MicroBooNE collaboration et al. *Differential cross section measurement of charged current ν_e interactions without final-state pions in MicroBooNE*. 2022. arXiv: 2208.02348 [hep-ex].

[55] M. A. Acero et al. "Measurement of the ν_e-Nucleus Charged-Current Double-Differential Cross Section at $< E_\nu >= 2.4$ GeV Using NOvA". In: *Phys. Rev. Lett.* 130 (5 Feb. 2023), p. 051802. DOI: 10.1103/PhysRevLett.130.051802.

[56] R. Acciarri et al. "Design and construction of the MicroBooNE detector". In: *Journal of Instrumentation* 12.02 (Feb. 2017), P02017. DOI: 10.1088/1748-0221/12/02/P02017. URL: https://dx.doi.org/10.1088/1748-0221/12/02/P02017.

[57] C. Rubbia. "The Liquid Argon Time Projection Chamber: A New Concept for Neutrino Detectors". In: *European Organization for Nuclear Research* (May 1977).

[58] Wouter Van de Pontseele. *PhD Thesis: Search for Electron Neutrino Anomalies with the MicroBooNE Detector*. 2020.

[59] T. Heindl et al. "The scintillation of liquid argon". In: *Europhysics Letters* 91.6 (Aug. 2010), p. 62002. DOI: 10.1209/0295-5075/91/62002.

[60] R Acciarri et al. "Effects of Nitrogen contamination in liquid Argon". In: *Journal of Instrumentation* 5.06 (June 2010), P06003. DOI: 10.1088/1748-0221/5/06/P06003.

[61] R Acciarri et al. "Oxygen contamination in liquid Argon: combined effects on ionization electron charge and scintillation light". In: *Journal of Instrumentation* 5.05 (May 2010), P05003. DOI: 10.1088/1748-0221/5/05/P05003.

[62] P. A. Zyla et al. "Review of Particle Physics". In: *PTEP* 2020.8 (2020), p. 083C01. DOI: 10.1093/ptep/ptaa104.

[63] Krishan Mistry. "First Measurement of the Flux-Averaged Differential Charged-Current Electron-Neutrino and Antineutrino Cross Section on Argon using the MicroBooNE Detector". PhD thesis. The University of Manchester, 2021.

[64] R Acciarri et al. "A study of electron recombination using highly ionizing particles in the ArgoNeuT Liquid Argon TPC". In: *Journal of Instrumentation* 8.08 (Aug. 2013), P08005. DOI: 10.1088/1748-0221/8/08/P08005.

[65] Tingjun Yang. "Calibration of Calorimetric Measurement in a Liquid Argon Time Projection Chamber". In: *Instruments* 5.1 (2021). ISSN: 2410-390X. DOI: 10.3390/instruments5010002.

[66] The MicroBooNE collaboration et al. "Measurement of the longitudinal diffusion of ionization electrons in the MicroBooNE detector". In: *Journal of Instrumentation* 16.09 (Sept. 2021), P09025. DOI: 10.1088/1748-0221/16/09/P09025.

[67] P. Abratenko et al. "Measurement of space charge effects in the MicroBooNE LArTPC using cosmic muons". In: *Journal of Instrumentation* 15.12 (Dec. 2020), P12037. DOI: 10.1088/1748-0221/15/12/P12037.

[68] C. Adams et al. "Ionization electron signal processing in single phase LArTPCs. Part II. Data/simulation comparison and performance in MicroBooNE". In: *Journal of Instrumentation* 13.07 (July 2018), P07007. DOI: 10.1088/1748-0221/13/07/P07007.

[69] C. Adams et al. "Design and construction of the MicroBooNE Cosmic Ray Tagger system". In: *Journal of Instrumentation* 14.04 (Apr. 2019), P04004. DOI: 10.1088/1748-0221/14/04/P04004.

[70] The MicroBooNE Collaboration. *Light Yield Calibration in MicroBooNE*. URL: https://microboone.fnal.gov/wp-content/uploads/MICROBOONE-NOTE-1120-TECH.pdf.

[71] P. Adamson et al. "The NuMI neutrino beam". In: *Nuclear Instruments and Methods in Physics Research Section A: Accelerators, Spectrometers, Detectors and Associated Equipment* 806 (2016), pp. 279–306. ISSN: 0168-9002. DOI: https://doi.org/10.1016/j.nima.2015.08.063.

[72] R.L. Workman *et al.* "Particle Data Group - Strange Mesons". In: Prog. Theor. Exp. Phys., 2015. URL: https://pdg.lbl.gov/2015/tables/rpp2015-tab-mesons-strange.pdf.

[73] *Beam Performance*. URL: https://microboone-exp.fnal.gov/at_work/beam/performance/pmg.html.

[74] L. Aliaga et al. "Design, calibration, and performance of the MINERvA detector". In: *Nuclear Instruments and Methods in Physics Research Section A: Accelerators, Spectrometers, Detectors and Associated Equipment* 743 (June 2014), pp. 130–159. DOI: 10.1016/j.nima.2013.12.053.

[75] S. Agostinelli et al. "Geant4—a simulation toolkit". In: *Nuclear Instruments and Methods in Physics Research Section A: Accelerators, Spectrometers, Detectors and Associated Equipment* 506.3 (2003), pp. 250–303. ISSN: 0168-9002. DOI: https://doi.org/10.1016/S0168-9002(03)01368-8.

[76] Leonidas Aliaga Soplin. "Neutrino Flux Prediction for the NuMI Beamline". PhD thesis. William-Mary Coll., 2016. DOI: 10.2172/1250884.

[77] Richard P. Feynman. "Very High-Energy Collisions of Hadrons". In: *Phys. Rev. Lett.* 23 (24 Dec. 1969), pp. 1415–1417. DOI: 10.1103/PhysRevLett.23.1415.

[78] J. Benecke et al. "Hypothesis of Limiting Fragmentation in High-Energy Collisions". In: *Phys. Rev.* 188 (5 Dec. 1969), pp. 2159–2169. DOI: 10.1103/PhysRev.188.2159.

[79] P. Skubic et al. "Neutral-strange-particle production by 300-GeV protons". In: *Phys. Rev. D* 18 (9 Nov. 1978), pp. 3115–3144. DOI: 10.1103/PhysRevD.18.3115.

[80] M. Bonesini et al. "On particle production for high energy neutrino beams". In: *The European Physical Journal C - Particles and Fields* 20 (1 Apr. 2001), pp. 13–27. DOI: 10.1007/s100520100656.

[81] C. Andreopoulos et al. "The GENIE neutrino Monte Carlo generator". In: *Nuclear Instruments and Methods in Physics Research Section A: Accelerators, Spectrometers, Detectors and Associated Equipment* 614.1 (Feb. 2010), pp. 87–104. DOI: 10.1016/j.nima.2009.12.009.

[82] J. Nieves et al. "Neutrino energy reconstruction and the shape of the charged current quasielastic-like total cross section". In: *Phys. Rev. D* 85 (11 June 2012), p. 113008. DOI: 10.1103/PhysRevD.85.113008.

[83] Jonathan Engel. "Approximate treatment of lepton distortion in charged-current neutrino scattering from nuclei". In: *Phys. Rev. C* 57 (4 Apr. 1998), pp. 2004–2009. DOI: 10.1103/PhysRevC.57.2004.

[84] J. Nieves, J. E. Amaro, and M. Valverde. "Inclusive quasielastic charged-current neutrino-nucleus reactions". In: *Phys. Rev. C* 70 (5 Nov. 2004), p. 055503. DOI: 10.1103/PhysRevC.70.055503.

[85] R. Bradford et al. "A New Parameterization of the Nucleon Elastic Form Factors". In: *Nuclear Physics B - Proceedings Supplements* 159 (2006). Proceedings of the 4th International Workshop on Neutrino-Nucleus Interactions in the Few-GeV Region, pp. 127–132. ISSN: 0920-5632. DOI: https://doi.org/10.1016/j.nuclphysbps.2006.08.028.

[86] Marco Del Tutto. "First Measurements of Inclusive Muon Neutrino Charged Current Differential Cross Sections on Argon at 0.8 GeV Average Neutrino Energy with the MicroBooNE Detector". PhD thesis. University of Oxford, 2019.

[87] Konstantin S., Kuzmin Vladimir V. Lyubushkin, and Vadim A. Naumov. "Lepton Polarization in Neutrino-Nucleon Interactions". In: 19 (2004), pp. 2815–2829. DOI: 10.1142/S0217732304016172.

[88] Jaroslaw A. Nowak and MiniBooNE Collaboration. "Four Momentum Transfer Discrepancy in the Charged Current π^+; Production in the MiniBooNE: Data vs. Theory". In: *AIP Conference Proceedings* 1189.1 (Nov. 2009), pp. 243–248. ISSN: 0094-243X. DOI: 10.1063/1.3274164. eprint: https://pubs.aip.org/aip/acp/article-pdf/1189/1/243/11982209/243_1_online.pdf.

[89] Ch. Berger and L. M. Sehgal. "Lepton mass effects in single pion production by neutrinos". In: *Phys. Rev. D* 76 (11 Dec. 2007), p. 113004. DOI: 10.1103/PhysRevD.76.113004.

[90] Ch. Berger and L. M. Sehgal. "Partially conserved axial vector current and coherent pion production by low energy neutrinos". In: *Phys. Rev. D* 79 (5 Mar. 2009), p. 053003. DOI: 10.1103/PhysRevD.79.053003.

[91] A Bodek and U K Yang. "Higher twist, ξw scaling, and effective LO PDFs for lepton scattering in the few GeV region". In: *Journal of Physics G: Nuclear and Particle Physics* 29.8 (July 2003), p. 1899. DOI: 10.1088/0954-3899/29/8/369.

[92] A Bodek and U K Yang. "Studies of higher twist and higher order effects in NLO and NNLO QCD analysis of lepton-nucleon scattering data on F_2 and $R = \sigma_L/\sigma_T$". In: *The European Physical Journal C - Particles and Fields* 13 (2000). DOI: 10.1007/s100520000320.

[93] M. Glück, E. Reya, and A. Vogt. "Dynamical parton distributions of the proton and small-x physics". In: *Zeitschrift für Physik C Particles and Fields* (1995). DOI: 10.1007/BF01624586.

[94] A. Bodek and J. L. Ritchie. "Fermi-motion effects in deep-inelastic lepton scattering from nuclear targets". In: *Phys. Rev. D* 23 (5 Mar. 1981), pp. 1070–1091. DOI: 10.1103/PhysRevD.23.1070.

[95] J. Schwehr, D. Cherdack, and R. Gran. *GENIE implementation of IFIC Valencia model for QE-like 2p2h neutrino-nucleus cross section*. 2017. arXiv: 1601.02038 [hep-ph].

[96] D. Ashery et al. "True absorption and scattering of pions on nuclei". In: *Phys. Rev. C* 23 (5 May 1981), pp. 2173–2185. DOI: 10.1103/PhysRevC.23.2173.

[97] P. Abratenko et al. "New CC0π GENIE model tune for MicroBooNE". In: *Phys. Rev. D* 105 (7 Apr. 2022), p. 072001. DOI: 10.1103/PhysRevD.105.072001.

[98] K. Abe et al. "Measurement of double-differential muon neutrino charged-current interactions on C_8H_8 without pions in the final state using the T2K off-axis beam". In: *Phys. Rev. D* 93 (11 June 2016), p. 112012. DOI: 10.1103/PhysRevD.93.112012.

[99] Afroditi P. et al. *Technical Note: MCC9 Overlay GENIE simulated BNB and Cosmic data*. URL: https://microboone-docdb.fnal.gov/cgi-bin/sso/ShowDocument?docid=20737.

[100] D.H. Wright and M.H. Kelsey. "The Geant4 Bertini Cascade". In: *Nuclear Instruments and Methods in Physics Research Section A: Accelerators, Spectrometers, Detectors and Associated Equipment* 804 (2015), pp. 175–188. ISSN: 0168-9002. DOI: https://doi.org/10.1016/j.nima.2015.09.058.

[101] (On behalf ofGeant4 Hadronic Working Group). "Improvements in the Geant4 Hadronic Physics". In: *Journal of Physics: Conference Series* 331.3 (Dec. 2011), p. 032002. DOI: 10.1088/1742-6596/331/3/032002.

[102] G. Folger and J. P. Wellisch. *String Parton Models in Geant4*. 2003. arXiv: nucl-th/0306007 [nucl-th].

[103] E.L. Snider and G. Petrillo. "LArSoft: toolkit for simulation, reconstruction and analysis of liquid argon TPC neutrino detectors". In: *Journal of Physics: Conference Series* 898.4 (Oct. 2017), p. 042057. DOI: 10.1088/1742-6596/898/4/042057.

[104] C. Adams et al. "Ionization electron signal processing in single phase LArTPCs. Part I. Algorithm Description and quantitative evaluation with MicroBooNE simulation". In: *Journal of Instrumentation* 13.07 (July 2018), P07006. DOI: 10.1088/1748-0221/13/07/P07006.

[105] X. Qian et al. "Three-dimensional imaging for large LArTPCs". In: *Journal of Instrumentation* 13.05 (May 2018), P05032. DOI: 10.1088/1748-0221/13/05/P05032.

[106] R. Acciarri et al. "Noise Characterization and Filtering in the MicroBooNE Liquid Argon TPC". In: *Journal of Instrumentation* 12.08 (Aug. 2017), P08003. DOI: 10.1088/1748-0221/12/08/P08003.

[107] B. Baller. "Liquid argon TPC signal formation, signal processing and reconstruction techniques". In: *Journal of Instrumentation* 12.07 (July 2017), P07010. DOI: 10.1088/1748-0221/12/07/P07010.

[108] *Online demonstration of signal processing*. URL: https://lar.bnl.gov/magnify/#/.

[109] The MicroBooNE collaboration et al. "Neutrino event selection in the MicroBooNE liquid argon time projection chamber using Wire-Cell 3D imaging, clustering, and charge-light matching". In: *Journal of Instrumentation* 16.06 (June 2021), P06043. DOI: 10.1088/1748-0221/16/06/P06043.

[110] *XGBoost Documentation*. URL: https://xgboost.readthedocs.io/en/stable/.

[111] P. Abratenko et al. "Cosmic Ray Background Rejection with Wire-Cell LArTPC Event Reconstruction in the MicroBooNE Detector". In: *Phys. Rev. Applied* 15 (6 June 2021), p. 064071. DOI: 10.1103/PhysRevApplied.15.064071. URL: https://link.aps.org/doi/10.1103/PhysRevApplied.15.064071.

[112] The MicroBooNE Collaboration. "Cosmic Ray Background Rejection with Wire-Cell LArTPC Event Reconstruction in MicroBooNE". In: (2021). URL: https://microboone-docdb.fnal.gov/cgi-bin/sso/ShowDocument?docid=27695.

[113] MicroBooNE Collaboration et al. "Wire-cell 3D pattern recognition techniques for neutrino event reconstruction in large LArTPCs: algorithm description and quantitative evaluation with MicroBooNE simulation". In: *Journal of Instrumentation* 17.01 (Jan. 2022), P01037. DOI: 10.1088/1748-0221/17/01/P01037.

[114] The MicroBooNE Collaboration. "Measurement of Charged-Current ν_μ and ν_e Interactions Towards a Search for Low Energy ν_e Events Using Wire-Cell in MicroBooNE". In: *MICROBOONE-NOTE-1100-PUB* (Aug. 2021). URL: https://microboone.fnal.gov/wp-content/uploads/MICROBOONE-NOTE-1100-PUB-1.pdf.

[115] Marc Paterno. "Calculating efficiencies and their uncertainties". In: (Dec. 2004). DOI: 10.2172/15017262.

[116] *Function Minimizations and Error Analysis*. URL: http://cdssls.cern.ch/record/2296388/files/minuit.pdf.

[117] The MicroBoonE Collaboration. "Measurement of charged-current ν_μ and ν_e interactions towards a search for low energy ν_e events using Wire-Cell in MicroBooNE". In: (2021). DOI: https://microboone-docdb.fnal.gov/cgi-bin/sso/ShowDocument?docid=33302.

[118] N. Ishida et al. "Attenuation length measurements of scintillation light in liquid rare gases and their mixtures using an improved reflection suppresser". In: *Nuclear Instruments and Methods in Physics Research Section A: Accelerators, Spectrometers, Detectors and Associated Equipment* 384.2 (1997), pp. 380–386. ISSN: 0168-9002. DOI: https://doi.org/10.1016/S0168-9002(96)00740-1.

[119] Emily Grace et al. "Index of refraction, Rayleigh scattering length, and Sellmeier coefficients in solid and liquid argon and xenon". In: *Nuclear Instruments and Methods in Physics Research Section A: Accelerators, Spectrometers, Detectors and Associated Equipment* 867 (2017), pp. 204–208. ISSN: 0168-9002. DOI: https://doi.org/10.1016/j.nima.2017.06.031.

[120] A. Neumeier et al. "Attenuation measurements of vacuum ultraviolet light in liquid argon revisited". In: *Nuclear Instruments and Methods in Physics Research Section A: Accelerators, Spectrometers, Detectors and Associated Equipment* 800 (2015), pp. 70–81. ISSN: 0168-9002. DOI: https://doi.org/10.1016/j.nima.2015.07.051.

[121] J. Calvo et al. "Measurement of the attenuation length of argon scintillation light in the ArDM LAr TPC". In: *Astroparticle Physics* 97 (2018), pp. 186–196. ISSN: 0927-6505. DOI: https://doi.org/10.1016/j.astropartphys.2017.11.009.

[122] P. Abratenko et al. "Novel approach for evaluating detector-related uncertainties in a LArTPC using MicroBooNE data". In: *The European Physical Journal C* 82.5 (May 2022). DOI: 10.1140/epjc/s10052-022-10270-8.